Titre: Title:	Subsynchronous Resonance in DFIG-Based Wind Farms
Auteur: Author:	Mohsen Ghafouri
Date:	2018
Type:	Mémoire ou thèse / Dissertation or Thesis
Référence: Citation:	Ghafouri, M. (2018). Subsynchronous Resonance in DFIG-Based Wind Farms [Ph.D. thesis, École Polytechnique de Montréal]. PolyPublie. https://publications.polymtl.ca/3025/

UNIVERSITÉ DE MONTRÉAL

SUBSYNCHRONOUS RESONANCE IN DFIG-BASED WIND FARMS

MOHSEN GHAFOURI
DÉPARTEMENT DE GÉNIE ÉLECTRIQUE
ÉCOLE POLYTECHNIQUE DE MONTRÉAL

THÈSE PRÉSENTÉE EN VUE DE L'OBTENTION
DU DIPLÔME DE PHILOSOPHIÆ DOCTOR
(GÉNIE ÉLECTRIQUE)
AVRIL 2018

UNIVERSITÉ DE MONTRÉAL

ÉCOLE POLYTECHNIQUE DE MONTRÉAL

Cette thèse intitulée :

SUBSYNCHRONOUS RESONANCE IN DFIG-BASED WIND FARMS

présentée par : GHAFOURI Mohsen
en vue de l'obtention du diplôme de : Philosophiæ Doctor
a été dûment acceptée par le jury d'examen constitué de :

M. SAYDY Lahcen, Ph. D., président
M. KARIMI Houshang, Ph. D., membre et directeur de recherche
M. MAHSEREDJIAN Jean, Ph. D., membre et directeur de recherche
M. SHESHYEKANI Keyhan, Ph. D., membre
Mme AKHRIF Ouassima, Ph. D., membre externe

DEDICATION

To my mother

ACKNOWLEDGMENTS

I would like to acknowledge the following people who were involved in my thesis. First, my supervisors and jury members :

– My supervisor Prof. Houshang Karimi for his kind support, supervision, trust.
– My co-supervisor Prof. Jean Mahseredjian for his valuable advices and constant support.
– My co-supervisor Dr. Karaagac for his expertise, encouragement and patience.
– Prof. Lahcen Saydy for his constant support, orientation and encouragement.
– Prof. Sherif Faried for his encouragement and precious advice.

I also would like to express my gratitudes to the external jury member Prof. Oussima Akhrif from ETS university. Finally, special thanks to Senvion wind turbine generator and Ecole polytechnique de Montreal for their financial support.

RÉSUMÉ

La résonance sous-synchrone (SSR) se produit lorsqu'un réseau de transmission est compensé et un générateur commence à échanger de l'énergie aux fréquences inférieures à celles du système d'alimentation. Ce phénomène a été observé dans la centrale électrique d'Arizona en 1970, lorsqu'un générateur synchrone a été relié radialement à une ligne compensée. Depuis, des recherches approfondies ont été réalisées pour analyser et atténuer ces oscillations. En octobre 2009, un incident d'interaction de contrôle sous-synchrone (SSCI) s'est produit dans le système d'énergie ERCOT (parc éolien de Zorillo Gulf au Texas), ce qui a révélé la susceptibilité des parcs éoliens à générateur d'induction doublement alimentés (DFIG) à des phénomènes sous-synchrone.

Dans cette thèse, le problème de SSCI dans un parc éolien basé sur DFIG relié à la ligne de transmission compensée en série est étudié. Les équations linéarisées qui décrivent le comportement du système sont développées sur la base du modèle réaliste de l'éolienne. Cet ensemble d'équations est utilisé pour obtenir un aperçu du comportement du système et de ses modes dominants. Plusieurs points de repère sont également développés sur la base du système d'alimentation réaliste pour aborder le problème de la simplicité et du système irréaliste dans la littérature existante. La simulation électromagnétique (EMT) a été utilisée pour obtenir le comportement transitoire précis du système et vérifier son exécution avec les exigences du code de réseau. Les points de repère développés ainsi que l'approche de balayage de fréquence, la méthode basée sur l'impédance, l'analyse de valeurs propres ou les simulations EMT permettent de détecter le risque potentiel des oscillations SSCI. Les analyses de valeurs propres et de sensibilité sont ensuite effectuées pour observer l'impact de différents paramètres système sur la stabilité. Plusieurs contrôleurs supplémentaires sont proposés pour résoudre le problème de stabilité et les mauvaises performances résultant du phénomène SSCI. Les contrôleurs proposés sont conçus selon la topologie et les conditions de fonctionnement du système d'alimentation. Pour vérifier la performance des contrôleurs proposés, plusieurs études de simulation sont réalisées dans le logiciel EMTP-RV. Dans les études de simulation, un modèle de parc éolien détaillé comprenant les fonctions de détection de défauts (FRT), le contrôleur de parc éolien (WFC), les non-linéarités du circuit électrique et de contrôle, le réseau de sous-transmission détaillé et la vitesse du vent non homogène sont considérés. Le problème du contrôleur SSCI complémentaire local ou central et l'impact de l'agrégation des générateurs d'éoliennes sur la procédure de conception sont également discutés. En outre, il est démontré que la défaillance du capteur et les retards peuvent affecter négativement la stabilité du système lorsque le contrôleur supplémentaire est inclus au niveau

secondaire. Ces défis de mise en œuvre sont étudiés dans cette recherche et plusieurs solutions sont proposées pour augmenter la marge de retard et pour obtenir un système de contrôle tolérant aux pannes.

ABSTRACT

Subsynchronous resonance (SSR) occurs when a compensated transmission network and a generator start to exchange energy at frequencies lower than that of the power system. This phenomenon was observed in an Arizona power station in 1970, when a synchronous generator was radially connected to a compensated line. Since then, extensive research has been conducted to analyze and mitigate such oscillations. In October 2009, a subsynchronous control interaction (SSCI) incident occurred at an ERCOT (Electric Reliability Council of Texas) power system (at Zorillo-Gulf wind farm) which revealed the susceptibility of doubly-fed induction generator (DFIG)-based wind farms to the subsynchronous phenomenon.

This thesis investigates the SSCI problem in a DFIG-based wind farm connected to a series compensated transmission line. The linearized equations which describe the behavior of the system are developed based on a realistic wind turbine model. This set of equations is utilized to gain insight into the behavior of the system and its dominant modes. Benchmarks are developed based on realistic power systems to tackle the problems caused by the application of oversimple and unrealistic case study systems that exist in the literature. Electromagnetic transient (EMT) simulation is carried out to obtain the precise dynamic response of the system and to verify its compliance with the grid code requirements. The developed benchmarks together with the frequency scan approach, the impedance-based method, eigenvalue analysis, and EMT simulations are used to identify the potential risk of the SSCI oscillations and to obtain guidelines for the safe operation of the system. Eigenvalue and sensitivity analyses are then performed to evaluate the impact of different parameters on the stability of the system. Supplementary controllers are proposed to tackle the stability problem and the poor performance due to the SSCI phenomenon. The proposed controllers are designed according to the topology and the operating conditions of the power system. To examine the performance of the proposed controllers, several simulation studies are carried out using the EMTP-RV software. In the simulation studies, a detailed wind farm model is considered. This detailed model includes the fault-ride-through (FRT) functions, a wind farm controller (WFC), the nonlinearities of the electrical and control circuits, a detailed sub-transmission network, and non-homogeneous wind speed. The problems of local and central supplementary SSCI controllers and the impact of aggregating the wind turbine generators in the design procedure are also discussed. It is shown that delays and sensor failure can adversely affect stability when a supplementary controller is included at the secondary level. To overcome these implementation challenges, some existing approaches such as Smith predictor scheme and residue generation method are used in order to increase the delay margin and to achieve a fault-tolerant control system.

TABLE OF CONTENTS

LIST OF TABLES

LIST OF FIGURES

LIST OF ABBREVIATIONS

DFIG	Doubly-fed induction generator
DFT	Discrete Fourier transformation
EMT	Electromagnetic transients
FACTS	Flexible alternating current transmission system
FDI	Fault detection and isolation
FFT	Fast Fourier transformation
FRT	Fault-ride-through
FTCS	Fault tolerant control system
GSC	Grid side converter
HVDC	High-voltage direct current
HVRT	High-voltage-ride-through
IGE	Induction generator effect
LFT	Linear fractional transformation
LTI	Linear time invariant
LVRT	Low-voltage-ride-through
MPPT	Maximum power point tracking
POI	Point of interconnection
RSC	Rotor side converter
SFR	Stator flux reference
SSCI	Subsynchronous control interaction
SSI	Subsynchronous interaction
SSO	Subsynchronous oscillation
SSR	Subsynchronous resonance
SSTI	Subsynchronous torsional interaction
SVR	Stator voltage reference
TI	Torsional interaction
WF	Wind farm
WFC	Wind farm controller
WT	Wind turbine

LIST OF APPENDIX

CHAPTER 1 INTRODUCTION

1.1 Problem Definition

Wind energy production units are the most common type of renewable energy sources in actual practical use in power systems at the present time. The International Energy Agency (IEA) reports indicate that renewable energy sources will provide 25% of the global electricity consumption by 2035 [1]. Furthermore, the wind energy contributes almost 34% of the total renewable energy in 2016 due to its advantages such as low environmental impacts and cost efficiency [2]. The cost of wind energy has dropped from 0.40 USD/kWh to 0.025-0.05 USD/kWh since the 1980s. Therefore, new trends towards the integration of renewable energies into the utility grid will consider wind power as a remarkable source for the production of electricity.

Global Wind Energy Council statistics show that the capacity of installed wind farms has grown by 22% in 2015 with respect to 2014 [3]. The total capacity of the wind turbines installed in the United States in 2016 was 8,203 MW, equal to the amount installed in 2015 according to the available statistics [3]. In 2016, the total wind energy capacity installed globally yielded a growth of more than 82 GW in electricity production with respect to 2015. The installed wind energy capacity in Canada was 11,898 MW in 2016, of which 3,510 MW was produced in Quebec [4].

Several technologies have been developed to harvest wind energy. Table 1.1 shows the different types of wind farm technologies used in power systems.

Among the existing wind turbine technologies, types 3 and 4 are the most commonly used as they are capable of harvesting the maximum available wind energy, i.e., operating in the maximum power point tracking (MPPT) mode. To achieve MPPT, wind turbines should be able to operate in the variable speed mode. The Doubly-fed induction generator (DFIG) technology (type 3) has attracted considerable attention since it requires lower-rate switching devices as compared to type 4. The schematic diagram of a typical DFIG is shown in Fig. 1.1. A DFIG-based wind turbine comprises an induction generator (IG), a back-to-back converter, a choke filter, two harmonic shunt filters and a mechanical system. The power produced by the DFIG is transferred to the grid through the stator of the induction generator and converters. A wind farm (WF) consists of turbines, medium voltage (MV) feeders, transformers and a wind farm controller (WFC).

Series compensated transmission lines were first introduced in the 1960s as an economical

Table 1.1 Wind turbine technologies.

Configuration	Type	Generator	Power Electronic Device
Fixed speed	A	Squirrel cage induction generator (SCIG)	Thyristor-based soft starter
Variable speed	B	Wound rotor induction generator (WRIG)	Diode-based rectifier bridge
	C	Doubly-fed induction generator (DFIG)	Back-to-back partial converter IGBT-based
	D	Permanent magnet synchronous generator (PMSG)	Back-to-back full converter IGBT-based

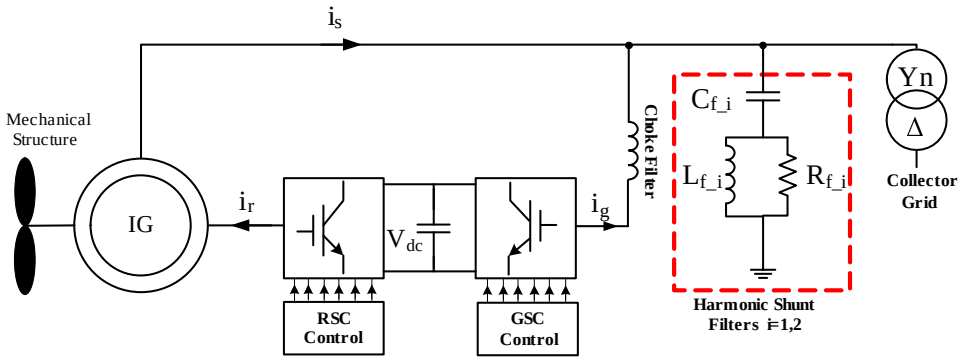

Figure 1.1 The DFIG structure.

solution to the problem of delivering to the grid the maximum power produced by generation units such as the wind farms or thermal power plants. A series compensated line is obtained by incorporating a series capacitor into the transmission line. This structure is advantageous as it enhances transient stability, increases the power line capacity, allows load sharing control, and accommodates the voltage drop. However, the series compensated transmission lines impose resonance conditions on the power system and may result in instability.

The investigations on the Mohave power station incidents of 1970 and 1971 revealed that a high level of compensation in a transmission line, i.e., a smaller series capacitor, may result in subsynchronous resonance (SSR). The SSR phenomenon is a condition in which the power components of the transmission line become oscillatory with frequencies equal to the natural frequencies of the overall power system [5, 6]. The frequencies of oscillations, i.e., the natural

frequencies, are below the synchronous frequency. This phenomenon may result in various power system issues (e.g., generation unit outages and power system instability). Therefore, its analysis and mitigation are important and challenging tasks in power system studies.

Along with the increased renewable energy production in the last decades, power systems have been facing numerous problems such as stability and sustainable integration of such systems. The ERCOT accident in 2009 shows that wind farms are vulnerable to a specific type of subsynchronous phenomenon, referred to as subsynchronous control interaction (SSCI). In SSCI, the frequency of oscillations is below the nominal frequency of the power system, and is equal to the resonance frequency of the series compensated transmission line. This resonance frequency can be calculated as $f_{ss} = f_n\sqrt{\frac{X_T}{X_C}}$, where f_n is the synchronous frequency in Hz, X_T is the series reactance of the power system, and X_C is the impedance of the series capacitor. Depending on the damping provided by the power system, these oscillations may remain undamped and cause severe damage to turbines and the power system. The main reason for insufficient damping of the power system is the fast reaction of the DFIG converters. Therefore, this type of oscillations should be addressed in the stability analysis of power systems that involve compensated transmission lines and DFIG-based wind farms.

1.2 Objectives

The main objective of this thesis is to propose supplementary controllers for the mitigation of the SSCI phenomenon. Several analysis techniques are employed to identify and evaluate the risk of SSCI, and to study the stability of wind farms connected to series compensated transmission lines. The results of the analyses are used to obtain guidelines for the safe operation of DFIG-based wind farms. More specifically, the objectives of the thesis are as follows.

- Providing a realistic model for a wind farm. The model is to include all of the functions needed for obtaining the precise transient behavior of the overall system.
- Proposing realistic benchmarks to be used as the systems under study.
- Determining the stability of power systems that are susceptible to the SSCI.
- Proposing supplementary controllers to improve the transient performance, and to increase the stability margin of the proposed benchmarks susceptible to the SSCI conditions.
- Comparing different control implementation structures (i.e., local versus central implementation) to achieve a better transient behavior and a simpler control scheme.
- Studying some of the implementation issues such as communication delay and sensor failure, and proposing some schemes to overcome those problems.

1.3 Methodology

The risk of the SSCI phenomenon can be identified using different analysis techniques [7]. These techniques determine whether or not an SSCI instability can occur in a power system. Moreover, these techniques provide the frequency of oscillations and also approximate the damping of the system. Frequency scan is one of the most popular frequency domain techniques, and we will use it in our analyses. In large electrical networks, this technique can be used to reduce the network size for the SSCI analysis. The SSCI may also occur following a contingency in the network, particularly, after contingencies that lead to a radially series compensated line connected to a generation unit. Therefore, we consider several scenarios for the analysis of SSCI. The results obtained from the frequency scan method are validated through EMT simulations. If the results of the frequency scan and EMT simulations show that, under various scenarios and operating conditions, the power system is not vulnerable to the SSCI phenomenon further detailed analysis will not be required.

A system prone to SSCI could be made to operate under safe conditions, that is in a region of parameters in which the system is stable. The safe operating conditions can be obtained through different methods of analysis. To apply those methods or techniques, one must have access to detailed models for the power system and the wind farm. Depending on the models available, the desired precision, and the objectives of analysis, an appropriate technique can be chosen. To validate the stability conditions obtained through analysis, a detailed model of the system including the FRT, WFC and all nonlinearities is developed and simulated using the EMTP-RV software. The results of analysis will also be used to determine the sensitivity of the system with respect to different parameters and operating conditions. There are three techniques employed in this thesis: (1) eigenvalue analysis, (2) residue-based analysis, and (3) EMT simulations. These techniques complement one another, so that a comprehensive analysis of the system must involve all of them. Guidelines for the safe operation of the system can be obtained using the analysis results. It should be noted that a simplified linearized model of the system is used for the analysis purposes; however, the results obtained are supported by the EMT simulations.

In this thesis, several supplementary controllers are designed and added to the existing DFIG control systems in order to mitigate the SSCI oscillations. Various design techniques such as the linear-quadratic-regulator (LQR), H^∞ and the μ-synthesis method are employed to design the supplementary controller. The LQR method provides a robust and structurally simple controller. However, several important control objectives such as noise attenuation and disturbance rejection may not be readily achievable by this method. The mixed-sensitivity H^∞ technique can be used to shape the desired frequency response of the system and achieve

several control objectives. However, this method requires a relatively high level of control theory expertise as well as a detailed mathematical model which may not be always available. Moreover, the mixed-sensitivity H^∞ technique results in high order controllers which are not usually desirable in the industry due to noise sensitivity and difficulties in implementation. The μ-synthesis technique is well-suited to power systems with a high level of uncertainties, e.g., systems with large variations in loading patterns, frequent line outages or systems with several SSCI modes. However, this method suffers from the same disadvantages as the mixed-sensitivity H^∞ technique. Therefore, each synthesis technique is advantageous over the others depending on the power system topology, modeling details and desired control objectives.

A wind farm can be represented by an equivalent single DFIG turbine, referred to as an aggregated model. We have used the linear aggregated model of the system to design the supplementary controllers and to perform the stability analysis of the closed-loop system in all cases. To verify the performance of the proposed supplementary SSCI damping controllers, a detailed model of the wind farm considering all nonlinear dynamics and functions is implemented in the proposed benchmarks. The EMT simulation results show the effectiveness of the proposed supplementary controller in mitigating the SSCI oscillations.

In this thesis, a framework is also proposed to alleviate the impact of sensor failure on the wind farm stability. The residue generation technique [8] is utilized to distinguish between power system faults and sensor failures. The proposed framework improves the robustness of the wind farm against sensor failures. The stability analysis of the wind farm system subject to communication delays between the central control unit and the wind turbines is also addressed in this research. This problem arises when the SSCI supplementary controller is implemented at the secondary control level. The impact of different wind farm operating conditions and power system parameters on the stability margin is investigated using the Guardian Map Theory and Rekasius's Substitution [9, 10]. The Smith predictor scheme is then applied to increase the delay margin of the system.

1.4 Contributions

The main contributions of this thesis are as follows:

- Proposing three new benchmarks representing realistic power systems that include wind farms.
- Proposing guidelines for the safe operation of wind farms connected to series compensated transmission lines using the frequency scan, eigenvalue analysis, and EMT simulations.
- Designing and applying supplementary controllers to mitigate SSCI oscillations.
- Proposing a new scheme (local adaptive implementation) for the implementation of the

supplementary controllers in a realistic and detailed wind farm.
– Improving the performance of the control system in the presence of technical challenges such as sensor failure and delay.

1.5 Thesis Structure

In Chapter 2, a comprehensive literature review is carried out on the analysis and mitigation of the subsynchronous phenomenon. The limitations of the methods proposed in the existing literature are presented in this chapter. The DFIG modeling, the wind farm structure, the benchmarks used for the design, the stability analysis, and the simulations appear in Chapter 3. Chapter 4 describes the subsynchronous phenomenon and presents the analysis methods used for the SSCI studies. The frequency scan method, eigenvalue analysis, robust stability analysis, the residue-based method, and the EMT simulation of the benchmarks are performed and the results are discussed in this chapter. Chapter 5 proposes the supplementary controllers for mitigating the SSCI oscillations, investigates their implementation options (local or central), and studies the impact of aggregating wind farm model on the closed-loop system behavior. Sensor failures and communication delays are also addressed in this chapter. Finally, Chapter 6 concludes the thesis.

CHAPTER 2 LITERATURE REVIEW

The analysis and mitigation of subsynchronous phenomenon have received considerable attention since the Mohave accident [11, 12, 13]. Recent studies demonstrate that DFIG-based wind farms connected to series compensated lines are susceptible to SSCI [14, 15]. This was confirmed in October 2009 when the first SSCI incident occurred in the Zorillo Gulf wind farm in Texas [16, 17, 18, 19]. The literature on the subsynchronous phenomenon is mainly categorized into analysis and mitigation methods. In the following two sections, the most recent literature on analysis and mitigation methods are presented.

2.1 Subsynchronous Phenomenon : Analysis Methods

The first step in analyzing the subsynchronous phenomenon is to investigate the possibility of its occurrence. The frequency scan method provides a better understanding of the system behavior over the subsynchronous frequency range [20]. Using this method, one can determine whether a power system can potentially undergo the subsynchronous phenomenon. Moreover, this method can provide an approximation of the damping factor of the subsynchronous modes. To show the effectiveness of the frequency scan method, the ERCOT benchmark (first SSCI incident) was studied in [21]. The results of the frequency scan of a North American power system with compensated lines have been presented in [22]. The results obtained help power system planners to consider the subsynchronous risk in their designs. A comprehensive SSR screening which analyzes the western electricity coordinating council (WSCC) network is presented in [23]. In this study, sensitivity analysis in used to show the impact of in-service turbines on the loci of the SSCI modes. The general methodology for screening the SSCI in DFIG-based wind farms has been proposed in [20, 7, 19]. The reactance crossover approach for computing the resonance frequency of a power system has been discussed in [24]. Frequency scan can be performed using different approaches and different signals, with each approach having its own advantages and disadvantages. These methods and their performances in identifying the subsynchronous risk have been discussed in [25]. The frequency scan methods proposed in the literature are only able to identify the frequencies in which subsynchronous oscillations are likely to occur. Therefore, to obtain more accurate results, a modified method which takes into account the combined turbine and power system impedances is presented in [26, 27]. The frequency scan method is also able to identify the torsional interaction phenomenon as detailed in [28]. It should be noted that EMT simulations of the system or the measured data should be used to validate the results obtained from the screening

methods.

The other well-known type of analysis, the eigenvalue analysis, has been applied to the IEEE SSR first benchmark model to identify the subsynchronous phenomenon and distinguish between different modes of the power system [29, 30, 31, 32]. The proposed approach can be replicated for any power system and wind farm topology to obtain the subsynchronous modes using the linear model of the system. This approach provides a good understanding of the system behavior as it yields the frequency and damping of all the system modes. However, this method requires detailed state-space modeling of the system, and consequently, it will become more complicated as the size of the power system increases. Sensitivity analysis can be performed based on eigenvalue analysis to observe the impact of different parameters on the subsynchronous modes [29].

To simply carry out the stability analysis, the impedance-based method has been proposed in [33, 34]. In this method, the interaction between the voltage-sourced converters (VSCs) of the DFIG and the power system is characterized by the ratio of their impedances [33]. The impedance of the converter directly corresponds to its control system parameters. Hence, this method is able to determine the impact of control system parameters on the DFIG response and on the system stability. The subsynchronous stability analysis of the IEEE SSR first benchmark model has been investigated using this method in [35, 36, 37, 38]. In these works, the Nyquist criterion is adopted to draw conclusion about the stability of the system. This technique results in a fast but not necessarily an accurate analysis of the phenomenon; therefore, its application in the literature is limited.

Residue-based analysis has been employed in several power system applications to determine the best feedback signal and the most effective feedback location in the control scheme to improve the stability margin [39, 40]. Using this method, the structure of the supplementary SSCI damping controller is determined based on the modal information of the system [32, 41, 42]. However, the application of this method is limited as the suggested measurement signals may be difficult or impossible to obtain.

The EMT type simulations have been applied to accurate power system models to obtain their precise transient behaviors. This method uses a detailed three-phase model of the system considering transmission lines, cables, and machines even under unbalanced and nonlinear conditions. Since nonlinear modeling of complex components is taken into account, this approach is well-suited for subsynchronous studies [43, 44, 45].

Any of the analysis methods described above can provide some insight into the system's behavior. The frequency scan methods are able to identify the risk of subsynchronous oscillations as well as the approximate frequency and damping of oscillations. However, these methods

cannot demonstrate the system behavior in frequency or time domain. The eigenvalue and impedance-based analysis methods provide modal information and stability condition of the linearized system. However, they fail to provide any reliable results for large-scale systems. The EMT simulation method demonstrates the detailed time domain behavior of the system. Nevertheless, it is not able to provide frequency domain information and cannot be used for the system design. In this thesis, we have used all of the described methods in order to thoroughly analyze the subsynchronous phenomenon.

2.2 Mitigation of the Subsynchronous Phenomenon

There has been a growing interest in developing effective SSCI mitigation methods ever since the first subsynchronous incident [11]. The mitigation methods proposed in the literature are as follows.

2.2.1 FACTS Devices

FACTS devices have proven to be an effective solution for damping subsynchronous oscillations. A gate-controlled series capacitor (GCSC) has been used to mitigate the SSR phenomenon in DFIG-based wind farms in [46]. The subsynchronous oscillations of the turbine-generator shaft are alleviated by the GCSC [47]. To mitigate the SSR oscillations, the fuzzy control approach is proposed and incorporated in the control strategy of the GCSC [48]. The GCSC and the thyristor-controlled series capacitor (TCSC) have been employed to damp the SSR in a fixed speed wind farm [49]. The same method for damping the oscillations in a DFIG-based wind farm has been proposed by [50]. To mitigate the SSR oscillations, static VAR compensator (SVC) together with the TCSC have been used in [51]. The SVC itself has also been utilized to tackle subsynchronous instability as presented in [52, 53]. To optimally damp the subsynchronous oscillations, the procedure of designing an SVC controller has been detailed in [54]. A static synchronous compensator (STATCOM) is used as a shunt FACTS device to control the flow of reactive power and to improve the transient stability of power systems [55]. The alleviation of SSR can be achieved using the STATCOM as demonstrated in [55, 56]. The STATCOM is also utilized to damp the SSR in induction generator-based wind farms [57]. The damping of the SSR oscillations using the TCSC has been addressed in [58, 59, 60]. A static synchronous series compensator (SSSC) is another FACTS device capable of mitigating the SSR [61, 62, 63]. It has been shown that an SSSC together with a dielectric capacitor are able to eliminate the SSR oscillations in DFIG-based wind farms [64]. The SSSC and a fixed capacitor have been used to damp the power swings and the SSR in a phase-imbalanced series capacitive network [65]. Despite the advantages of the FACTS

devices, they incur huge costs of design and implementations.

2.2.2 Narain G. Hingorani (NGH) Strategy

In this method, the zero-crossings (time instances at which the value of the voltage is zero) of the compensating capacitor voltage are measured and used to determine the frequency. In case of the subsynchronous phenomenon, the measured frequency deviates toward the subsynchronous frequency. To overcome the SSR using the NGH method, the thyristor (Fig. 2.1) fires and the capacitor discharges into the resistor; consequently, the zero-crossing of the capacitor voltage changes, and the change results in the removal of the subsynchronous frequency contents. The thyristor will then turn off whenever the capacitor voltage indicates the elimination of the subsynchronous frequency contents from the voltage signal. Fig. 2.1 shows the schematic of the NGH strategy [66, 67, 68].

2.2.3 Blocking Filter

Blocking filters are used in the generator or the capacitor sides of the transmission line to eliminate subsynchronous oscillations [69, 70, 71]. Although the blocking filter shows good performance, particularly for the torsional modes, it needs to be regularly retuned as the subsynchronous frequency will vary due to the changes in the power system topology and also due to the aging of the elements of the filter. Therefore, the application of this method in power systems is limited.

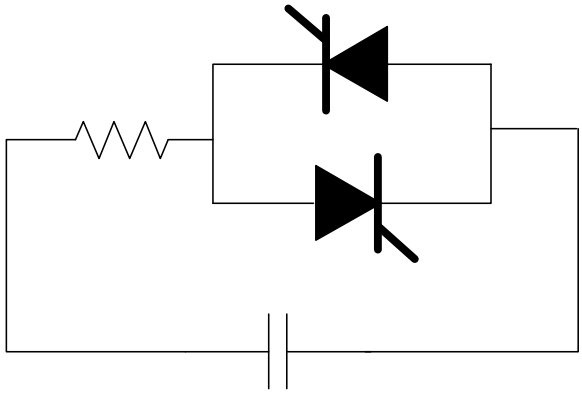

Figure 2.1 The circuit demonstrating NGH strategy.

2.2.4 Supplementary Controller

As discussed before, subsynchronous oscillations can be alleviated by using FACTS devices, blocking filters and the NGH strategy. However, a large-scale installation of such components with the sole purpose of mitigating the subsynchronous oscillations may not be cost effective. Therefore, using the control system of the DFIG converters to mitigate the subsynchronous phenomenon is gaining more attention due to its effectiveness and low cost. In general, there are two methods to damp the subsynchronous oscillations through the controller of the DFIG wind turbines. The first method is to optimize the existing controller parameters so that the damping in the subsynchronous frequency range becomes positive [72, 73]. However, such optimization may result in unsatisfactory transient behavior during faults as the DFIG will not be able to provide the required reactive power. The second approach, which is the subject of this thesis, is to design a supplementary SSCI damping controller and append it to the control system of the DFIG [42, 74, 75, 76, 77, 78, 79]. These supplementary control schemes include the linear-quadratic regulator (LQR) [77], the lead-lag compensator [74], the low-pass filter with phase compensation [78], partial feedback linearization (PFL) [76], and proportional-integral (PI) controllers [79].

A nonlinear damping controller designed using the PFL technique is proposed to damp the subsynchronous oscillations in a simplified Nordic power system in [76]. Several small-signal stability analyses including the eigenvalue analysis are performed in this study to identify the subsynchronous phenomenon. A novel 2DOF control strategy combined with a damping control loop is proposed to alleviate the SSR which may arise due to the induction generator effect (IGE) in [78]. The eigenvalue analysis and the impedance-based stability criterion are deployed to analyze the system, and time-domain simulations are carried out to demonstrate the effectiveness of the proposed control technique in this study. The addition of the supplementary SSCI damping controller to the GSC and the RSC loops are compared to each other for the ERCOT power system in [42]. The eigenvalue analysis and EMT simulations are used in order to demonstrate the performance of the SSCI damping controller for different power system operating conditions and its effectiveness against small/large disturbances. The IGE is mitigated in a DFIG-based wind farm which is subjected to subsynchronous resonance in [80]. The GSC control system is used to damp the oscillations, and the eigenvalue analysis and EMT simulations are utilized to demonstrate the effectiveness of the damping controller. The modal analysis of a DFIG-based wind farm is performed to identify the four major system modes (i.e., subsynchronous, supersynchronous, electromechanical, and shaft modes) in [31]. This paper also presents a feasibility test for the input signal of the SSCI damping controller. Nyquist stability analysis is carried out to show that the DFIG-based wind farms

are more vulnerable to subsynchronous oscillations at lower wind speeds in [81, 79]. Moreover, it is demonstrated that RSC current control loops can effectively be used to improve the damping of the subsynchronous modes. The eigenvalue analysis and time-domain simulations are carried out to demonstrate that the series capacitor voltage is an effective signal as the input of the SSCI damping controller in [29, 32]. PI controllers whose parameters are obtained using the results of the eigenvalue analysis are employed as the supplementary damping controllers in [29, 32]. SSCI mitigation is achieved in a power system which is comprised of DFIG and FFC turbines as well as an HVDC system in [44]. The output of the lead-lag supplementary controller is applied to the GSCs of DFIG and FFC wind turbines, and to the onshore Modular Multi-level Converter (MMC) of the offshore wind farms. This paper also investigates the impact of phase-imbalance series compensation as a countermeasure in SSCI damping. The time domain simulations are performed using the EMTP-RV software to show that the current of the transmission line and the active output power of the wind farm are effective input signals for damping controllers. The subsynchronous oscillations are damped in a DFIG-based wind farm using a simple proportional gain implemented in a GSC controller [50]. PSCAD/EMTDC simulations are used to perform the time-domain analysis in this study.

The current supplementary controllers are only able to damp the subsynchronous oscillations for a limited number of operating conditions. Furthermore, they do not employ realistic wind farm models, the variations in the power system parameters, and the transient behavior of the system against faults. Therefore, they are not able to damp the SSCI oscillations in a realistic power system. To overcome the drawbacks of the current supplementary methods, we will propose several damping controllers to tackle the subsynchronous phenomenon. Moreover, to validate the performance of the supplementary controllers proposed here, a few benchmark systems are developed. These benchmarks employ realistic power systems and wind farm structures.

2.3 Drawbacks of the Existing Mitigation Methods

The main drawbacks of the existing methods are summarized below.

– Most of the existing control methods are not able to mitigate subsynchronous oscillations under faulty or disturbed conditions for realistic wind farm scenarios, i.e., they fail if applied to a detailed wind farm model considering all nonlinearities. These methods use the IEEE first and second benchmarks [29] which have been developed for the SSR analysis in thermal power plants.
– The existing methods do not incorporate the secondary reactive power control in their

control loops and thus the impact of such controllers on the overall performance is unknown.
– They cannot provide a good transient response during faulty conditions as they do not include the wind farm controller (WFC) and the fault-ride-through (FRT) capabilities.
– They do not take into account the power system and wind farm uncertainties such as the wind speed, the outages, and the changes in the operating points.

CHAPTER 3 DFIG MODELING AND BENCHMARKS

Among different types of renewable energy-based generation, wind energy is one of the most commonly-used technologies for electric power production. A typical wind farm mainly consists of wind turbines, a subtransmission collector grid, transformers, and the main wind farm controller (WFC). Fig. 3.1 shows a simplified single-line diagram of a typical wind farm. In this structure, each wind turbine is connected to the collector grid by an LV/MV transformer. The collector grid is connected to the point of interconnection (POI) by a step-up MV/HV delta-grounded wye transformer. The WFC measures the current and voltage at the POI and regulates the reactive power, voltage or power-factor.

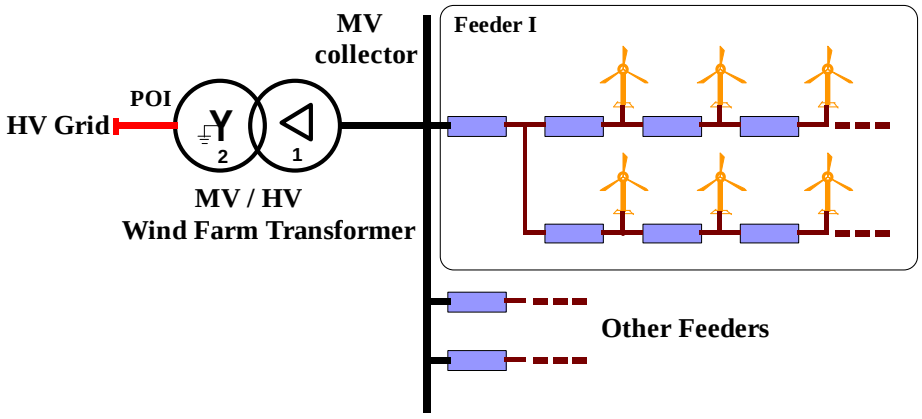

Figure 3.1 Wind farm structure.

The main objective of this chapter is to obtain linear equations describing the wind farm behavior. The derived equations will be used for SSCI analysis and the design of damping controllers in the following chapters. To verify the results obtained using a linearized model, a detailed wind farm model will also be developed in EMTP-RV simulation software in this chapter. Moreover, four benchmarks will be developed in this chapter using the wind farm and power system models. These benchmarks are inspired by actual power systems that may be subject to the subsynchronous phenomenon. The analysis and mitigation methods proposed in the following chapters will be verified using EMT simulations of these benchmarks.

Wind turbines can be mainly categorized into fixed and variable speed types. Among the variable speed types, the doubly-fed induction generator (DFIG) is the focus in this research.

In a DFIG, the rotor is connected to a back-to-back converter allowing bidirectional power flow and operation at both subsynchronous and supersyncheronous speeds. The stator is

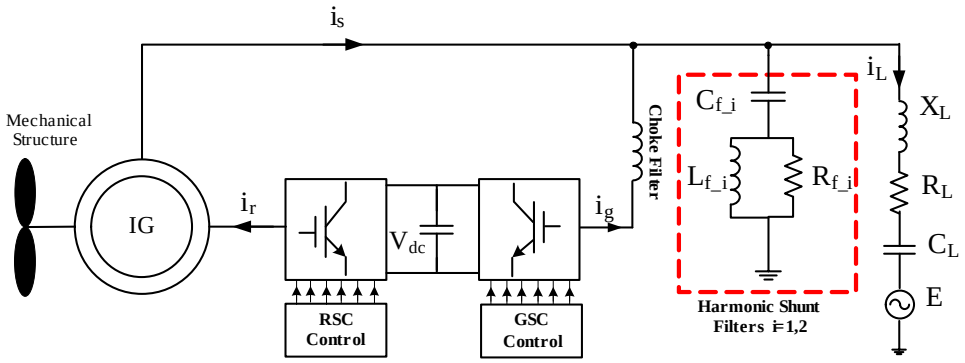

Figure 3.2 Simplified model of a DFIG-based wind farm connected to a series compensated transmission line.

directly connected to the grid. The back-to-back converter consists of two voltage-sourced converters (VSCs), namely, the rotor side converter (RSC) and the grid side converter (GSC). The DC bus of the back-to-back converter decouples the RSC and the GSC. The power quality of the GSC is improved by one choke filter and two shunt harmonic filters. Protection of the RSC against over-currents and protection of the DC capacitor against over-voltages are achieved by incorporating a crowbar connected to the rotor windings. During crowbar ignition, the RSC is blocked and the wind turbine starts to consume reactive power, similar to a squirrel-cage induction generator. To avoid unnecessary crowbar operation during the faults, a DC resistive chopper is also used to maintain the DC voltage within an acceptable limit, Fig. 3.2. When the wind speed is lower than its nominal value, a small portion of active power (maximum 30% of the wind power) flows from the rotor to the RSC. However, if the wind speed exceeds its nominal value (the hypersynchronous mode) the rotor absorbs some active power. A DFIG consists of the following components:

1. induction machine,
2. mechanical shaft and drive train,
3. converters,
4. control circuit,
5. choke filter,
6. shunt filters, and
7. protection systems.

For the sake of simplicity, all quantities are converted to per-unit values. The base values of the per-unit system are as follows:

$$S_b = S_{gen} N_{gen} \tag{3.1}$$

$$I_{b_{HV}} = \frac{S_b}{V_{b_{HV}}}$$
$$I_{b_{MV}} = \frac{S_b}{V_{b_{MV}}} \tag{3.2}$$
$$I_{b_{LV}} = \frac{S_b}{V_{b_{LV}}}$$
$$\omega_b = 2\pi f_n \tag{3.3}$$

where N_{gen} is the number of wind turbines in the wind farm, f_n is the nominal system frequency, and S_{gen}, the apparent power, represents the capacity of each wind turbine. $V_{b_{HV}}$, $V_{b_{MV}}$ and $V_{b_{LV}}$ represent the base voltages of the high voltage (HV) power system, medium voltage (MV) collector and low voltage (LV) DFIG terminal, respectively. To express time in the per-unit system, each differential equation is multiplied by the base angular frequency ω_b.

In the following sections, equations describing the dynamics of each component of the system are presented. The system here is a DFIG-based wind farm connected to a series compensated transmission line.

3.1 Asynchronous Machine

Asynchronous machines are the main part of DFIG-based wind farms. The wound rotor induction generator is used in the DFIG structure as it allows connection to the RSC, and consequently allows the active and reactive power control of the stator.

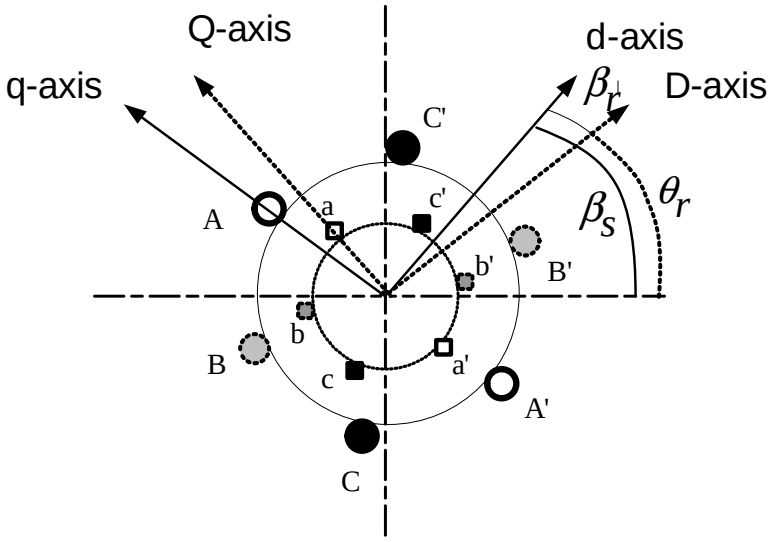

Figure 3.3 Induction machine windings and the corresponding dq-frames.

Fig. 3.3 shows the stator and rotor windings, and their corresponding rotating dq-frames. In this figure, the dq-axis and the DQ-axis rotate with the angular speeds of ω_s and ω_r, respectively. The voltages of the stator can be expressed as:

$$\begin{pmatrix} v_{as} \\ v_{bs} \\ v_{cs} \end{pmatrix} = R_s \begin{pmatrix} i_{as} \\ i_{bs} \\ i_{cs} \end{pmatrix} + \frac{d}{dt} \begin{pmatrix} \phi_{as} \\ \phi_{bs} \\ \phi_{cs} \end{pmatrix}. \tag{3.4}$$

Similarly, the rotor voltages can be obtained by Kirchhoff's and Faraday's laws as:

$$\begin{pmatrix} v_{ar} \\ v_{br} \\ v_{cr} \end{pmatrix} = R_r \begin{pmatrix} i_{ar} \\ i_{br} \\ i_{cr} \end{pmatrix} + \frac{d}{dt} \begin{pmatrix} \phi_{ar} \\ \phi_{br} \\ \phi_{cr} \end{pmatrix} \tag{3.5}$$

where the subscripts a, b, c, s, and r denote the phases a, b, c and the stator and rotor, respectively. The flux linkage is denoted by ϕ, and $R_x,\ x = \{r, s\}$ represent the resistances of the rotor and stator, respectively.

The flux linkage of the rotor and stator can be represented as a function of the currents and inductances:

$$\begin{pmatrix} \phi_{as} \\ \phi_{bs} \\ \phi_{cs} \end{pmatrix} = \mathbf{L_s} \begin{pmatrix} i_{as} \\ i_{bs} \\ i_{cs} \end{pmatrix} + \mathbf{L_m} \begin{pmatrix} i_{ar} \\ i_{br} \\ i_{cr} \end{pmatrix} \tag{3.6}$$

and

$$\begin{pmatrix} \phi_{ar} \\ \phi_{br} \\ \phi_{cr} \end{pmatrix} = \mathbf{L_r} \begin{pmatrix} i_{ar} \\ i_{br} \\ i_{cr} \end{pmatrix} + \mathbf{L_m^T} \begin{pmatrix} i_{as} \\ i_{bs} \\ i_{cs} \end{pmatrix} \tag{3.7}$$

where $\mathbf{L_s}$, $\mathbf{L_r}$ and $\mathbf{L_m}$ are the stator, rotor and mutual inductance matrices, respectively. They can be expressed by:

$$\mathbf{L_s} = \begin{pmatrix} L_{ls} + L_m & -\frac{1}{2}L_m & -\frac{1}{2}L_m \\ -\frac{1}{2}L_m & L_{ls} + L_m & -\frac{1}{2}L_m \\ -\frac{1}{2}L_m & -\frac{1}{2}L_m & L_{ls} + L_m \end{pmatrix} \tag{3.8}$$

$$\mathbf{L_r} = \begin{pmatrix} L_{lr} + L_m & -\frac{1}{2}L_m & -\frac{1}{2}L_m \\ -\frac{1}{2}L_m & L_{lr} + L_m & -\frac{1}{2}L_m \\ -\frac{1}{2}L_m & -\frac{1}{2}L_m & L_{lr} + L_m \end{pmatrix} \tag{3.9}$$

$$\mathbf{L_m} = L_m \begin{pmatrix} cos(\theta_r) & cos(\theta_r + \frac{2}{3\pi}) & cos(\theta_r - \frac{2}{3\pi}) \\ cos(\theta_r - \frac{2}{3\pi}) & cos(\theta_r) & cos(\theta_r + \frac{2}{3\pi}) \\ cos(\theta_r + \frac{2}{3\pi}) & cos(\theta_r) & cos(\theta_r - \frac{2}{3\pi}) \end{pmatrix} \tag{3.10}$$

where L_l and L_m are the leakage and magnetizing inductances. It should be noted that due to the symmetrical structure of the rotor, the mutual inductances between the stator and the rotor are equal. The angular displacement of the rotor can be obtained as:

$$\theta_r(t) = \int_0^t \omega_r dt + \theta_r^0 \tag{3.11}$$

In this equation, θ_r^0 is the initial rotor position. It should be noted that the machine equations are nonlinear and time-varying since they depend on the rotor's angular displacement. This makes the analysis complicated. To eliminate the time-dependency, the dq0-transformation is adopted. The following matrix $\mathbf{P}$ which represents the dq0-transformation, transforms the abc-frame quantities into the dq0-frame ones, i.e.,

$$\mathbf{f}_{abc} = \mathbf{P} \times \mathbf{f}_{dq0} \tag{3.12}$$

where

$$\mathbf{P} = \frac{2}{3} \begin{pmatrix} cos(\beta_{dq}) & cos(\beta_{dq} - \frac{2\pi}{3}) & cos(\beta_{dq} + \frac{2\pi}{3}) \\ -sin(\beta_{dq}) & -sin(\beta_{dq} - \frac{2\pi}{3}) & -sin(\beta_{dq} + \frac{2\pi}{3}) \\ \frac{1}{2} & \frac{1}{2} & \frac{1}{2} \end{pmatrix} \tag{3.13}$$

To eliminate the time-dependency, the angle β_{dq} needs to be selected appropriately. The phase-angle β_{dq} is defined as follows and is used by the dq0-transformation.

$$\beta_{dq}(t) = \int_0^t \omega_{dq} dt + \beta_{dq}^0 \tag{3.14}$$

The dq-frame can rotate with the synchronous speed of either the stator voltage or the stator

flux, and can be used by the RSC and GSC for their transformations. In the time-domain simulations, the RSC and GSC operate in the flux and voltage rotating frames, respectively. In the voltage reference frame (leading the flux-based frame by 90 degrees), the d-axis represents the active power and the q-axis represents the reactive power, whereas in the flux rotating frame, the d and q axes represent the reactive and active powers, respectively. If the stator voltage is applied to a phase-locked loop (PLL) and the phase-angle measured by the PLL is used for the Park transformation $\mathbf{P}$, then:

$$\omega_{dq} = \omega_s \tag{3.15}$$

In this case, the rotor quantities after the Park transformation $\mathbf{P}$ depend on the following angular displacement:

$$\beta_r = \beta_{dq} - \theta_r = \int_0^t (\omega_s - \omega_r)dt + (\beta_{dq}^0 - \theta_r^0) \tag{3.16}$$

Therefore, β_{dq} in the matrix $\mathbf{P}$ is equal to β_s which is the phase-angle of the stator quantities. In this chapter, the following assumptions have been made:

1. The induction machine operates under balanced conditions. Therefore, the variables on the zero-axis become zero.
2. The iron core saturation of the transformer is neglected due to its negligible impact on subsynchronous phenomena.
3. The voltage and current quantities are line-to-line RMS.

Applying the Park transformation to the voltage equations results in:

$$\mathbf{T_{dq0}}^{-1}(\beta_s)\vec{v_{dq0s}} = R_s\mathbf{T_{dq0}}^{-1}(\beta_s)\vec{i_{dq0s}} + \frac{d}{dt}\mathbf{T_{dq0}}^{-1}(\beta_s)\vec{\phi_{dq0s}} \tag{3.17}$$

$$\mathbf{T_{dq0}}^{-1}(\beta_r)\vec{v_{dq0r}} = R_r\mathbf{T_{dq0}}^{-1}(\beta_r)\vec{i_{dq0r}} + \frac{d}{dt}\mathbf{T_{dq0}}^{-1}(\beta_r)\vec{\phi_{dq0r}} \tag{3.18}$$

similarly, the flux equations are:

$$\mathbf{T_{dq0}}^{-1}(\beta_s)\vec{\phi_{dq0s}} = \mathbf{L_s}\mathbf{T_{dq0}}^{-1}(\beta_s)\vec{i_{dq0s}} + \mathbf{L_m}\mathbf{T_{dq0}}^{-1}(\beta_r)\vec{i_{dq0r}} \tag{3.19}$$

$$\mathbf{T_{dq0}}^{-1}(\beta_r)\vec{\phi_{dq0r}} = \mathbf{L_r}\mathbf{T_{dq0}}^{-1}(\beta_r)\vec{i_{dq0r}} + \mathbf{L_m^T}\mathbf{T_{dq0}}^{-1}(\beta_s)\vec{i_{dq0r}} \tag{3.20}$$

By multiplying both sides of (3.18) and (3.20) by $\mathbf{T_{dq0}}(\beta_r)$, and both sides of (3.17) and

(3.19) by $\mathbf{T_{dq0}}(\beta_s)$, one can obtain the following equations:

$$\vec{v_{dq0s}} = R_s \vec{i_{dq0s}} + \mathbf{T_{dq0}}(\beta_s)\frac{d}{dt}(\mathbf{T_{dq0}}^{-1}(\beta_s))\vec{\phi_{dq0s}} \tag{3.21}$$

$$\vec{v_{dq0r}} = R_r \vec{i_{dq0r}} + \mathbf{T_{dq0}}(\beta_r)\frac{d}{dt}(\mathbf{T_{dq0}}^{-1}(\beta_r))\vec{\phi_{dq0r}} \tag{3.22}$$

$$\vec{\phi_{dq0s}} = \mathbf{T_{dq0}}(\beta_s)\mathbf{L_s}\mathbf{T_{dq0}}^{-1}(\beta_s)\vec{i_{dq0s}} + \mathbf{T_{dq0}}(\beta_s)\mathbf{L_m}\mathbf{T_{dq0}}^{-1}(\beta_r)\vec{i_{dq0r}} \tag{3.23}$$

$$\vec{\phi_{dq0s}} = \mathbf{T_{dq0}}(\beta_r)\mathbf{L_r}\mathbf{T_{dq0}}^{-1}(\beta_r)\vec{i_{dq0r}} + \mathbf{T_{dq0}}(\beta_r)\mathbf{L_m^T}\mathbf{T_{dq0}}^{-1}(\beta_s)\vec{i_{dq0s}} \tag{3.24}$$

The second terms of the voltage equations can be simplified and rearranged as:

$$\mathbf{T_{dq0}}(\beta_s)\frac{d}{dt}(\mathbf{T_{dq0}}^{-1}(\beta_s)\vec{\phi_{dq0s}}) = \frac{d}{dt}\begin{pmatrix}\phi_{ds}\\ \phi_{qs}\end{pmatrix} + \omega_s\begin{pmatrix}\phi_{qs}\\ -\phi_{ds}\end{pmatrix} \tag{3.25}$$

$$\mathbf{T_{dq0}}(\beta_r)\frac{d}{dt}(\mathbf{T_{dq0}}^{-1}(\beta_r)\vec{\phi_{dq0r}}) = \frac{d}{dt}\begin{pmatrix}\phi_{dr}\\ \phi_{qr}\end{pmatrix} + (\omega_s-\omega_r)\begin{pmatrix}\phi_{qr}\\ -\phi_{dr}\end{pmatrix} \tag{3.26}$$

The coupling terms in equations (3.25) and (3.26) result from the Park transformation. In summary, the equations representing the induction machine model are expressed as:

$$v_{qs} = R_s i_{qs} + \frac{d}{dt}\phi_{qs} - \omega_s\phi_{ds} \tag{3.27}$$

$$v_{ds} = R_s i_{ds} + \frac{d}{dt}\phi_{ds} + \omega_s\phi_{qs} \tag{3.28}$$

$$v_{qr} = R_r i_{qr} + \frac{d}{dt}\phi_{qr} - (\omega_s-\omega_r)\phi_{dr} \tag{3.29}$$

$$v_{dr} = R_r i_{dr} + \frac{d}{dt}\phi_{dr} + (\omega_s-\omega_r)\phi_{qs} \tag{3.30}$$

The equations of rotor and stator fluxes are:

$$\phi_{ds} = L_{ls} i_{ds} + L_m(i_{ds}+i_{dr}) \tag{3.31}$$

$$\phi_{qs} = L_{ls} i_{qs} + L_m(i_{qs}+i_{qr}) \tag{3.32}$$

$$\phi_{dr} = L_{lr} i_{dr} + L_m(i_{ds}+i_{dr}) \tag{3.33}$$

$$\phi_{qr} = L_{lr} i_{qr} + L_m(i_{qs}+i_{qr}) \tag{3.34}$$

Substituting the flux quantities into the voltage equations, the induction machine can be

described as:

$$v_{ds} = R_s i_{ds} + L_s \frac{di_{ds}}{dt} + L_m \frac{di_{ds}}{dt} + L_m \frac{di_{dr}}{dt} + \omega_s L_s i_{qs} + \omega_s L_m i_{qs} + \omega_r L_m i_{qr} \tag{3.35}$$

$$v_{qs} = R_s i_{qs} + L_s \frac{di_{qs}}{dt} + L_m \frac{di_{qs}}{dt} + L_m \frac{di_{qr}}{dt} - \omega_s L_s i_{ds} - \omega_s L_m i_{ds} - \omega_r L_m i_{dr} \tag{3.36}$$

$$v_{dr} = R_r i_{dr} + L_r \frac{di_{dr}}{dt} + L_m \frac{di_{ds}}{dt} + L_m \frac{di_{dr}}{dt} + (\omega_s - \omega_r) L_r i_{qr} + (\omega_s - \omega_r) L_m i_{qs} + (\omega_s - \omega_r) L_m i_{qr} \tag{3.37}$$

$$v_{qr} = R_r i_{qr} + L_r \frac{di_{qr}}{dt} + L_m \frac{di_{qs}}{dt} + L_m \frac{di_{qr}}{dt} - (\omega_s - \omega_r) L_r i_{dr} - (\omega_s - \omega_r) L_m i_{ds} - (\omega_s - \omega_r) L_m i_{dr} \tag{3.38}$$

The equivalent circuit representing the dq-frame equations of the induction generator is shown in Fig. 3.4.

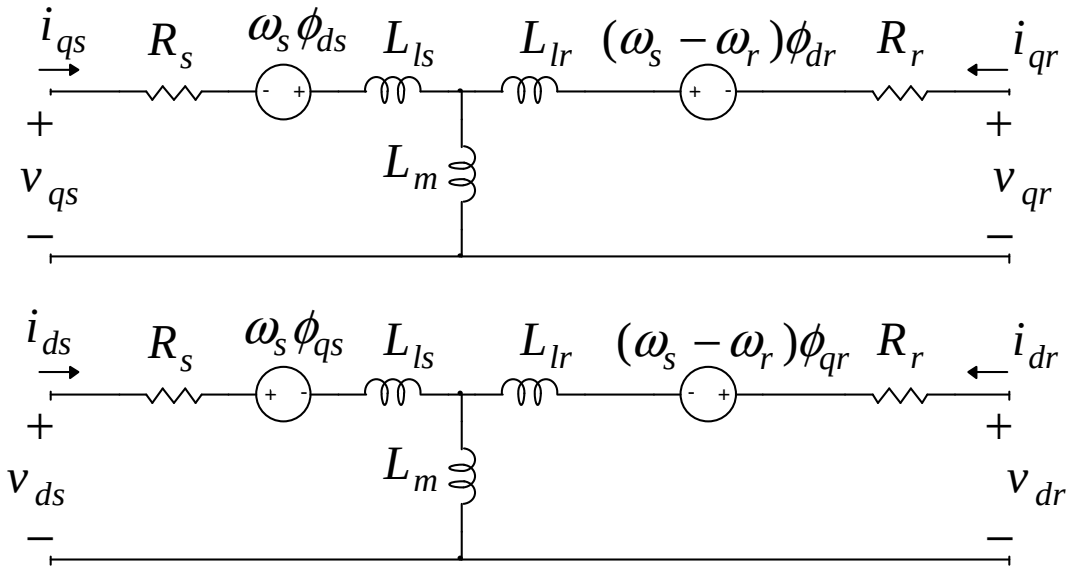

Figure 3.4 The equivalent circuit of induction machine in dq-frame.

3.2 Mechanical Structure

The mechanical system of a wind turbine should harvest the maximum possible kinetic energy in the swept area of the blades. The kinetic energy of wind can be obtained as:

$$P_{air} = \frac{1}{2} \rho A v^3 \tag{3.39}$$

$$A = \pi R^2 \tag{3.40}$$

where ρ is the air density (approximately 1.225 $\frac{Kg}{m^3}$), υ is the wind speed ($\frac{m}{s}$), R is the blade radius (m), and A is the surface swept by the blades. According to Betz law, the wind power transferred to the mechanical system of a turbine is limited by the coefficient C_p (limited to 66%). This coefficient can be determined by a curve fitting process considering both the tip-speed-ratio (λ) and the pitch angle (β) as given by:

$$C_P(\lambda,\beta) = \sum_{i=0}^{4}\sum_{j=0}^{4} \alpha_{ij}\beta^i\lambda^j \tag{3.41}$$

$$\lambda = \frac{\omega_t R}{\upsilon} \tag{3.42}$$

or equivalently

$$\begin{aligned} \lambda &= \frac{K_{speed}\omega_t}{\upsilon} \\ K_{speed} &= \frac{2\pi f_n R}{n_{pp} G} \end{aligned} \tag{3.43}$$

where n_{pp} is the number of pole pairs, G is the gearbox ratio, and f_n is the nominal frequency.

At each value of the wind speed, there is a specific value for the rotational speed of the wind turbine in which C_P becomes maximum, and consequently the maximum power transfer rate from the wind to the mechanical system occurs. If the wind speed exceeds its nominal value, the pitch angle increases to keep the power at its nominal value. At lower wind speeds, the turbine operates in a variable speed mode where the rotational speed is adjusted to achieve the maximum possible C_P.

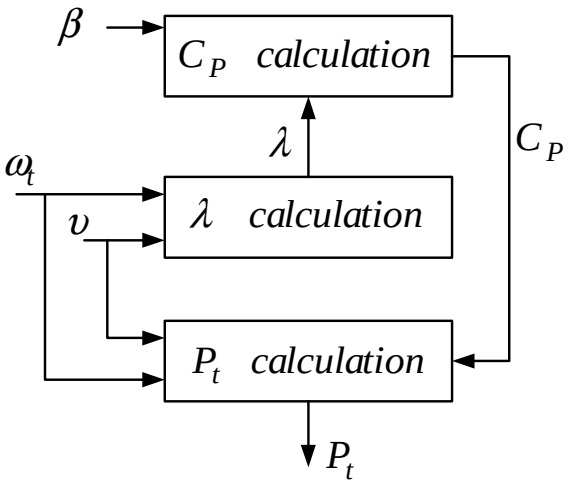

Figure 3.5 Wind turbine mechanical power calculation scheme.

The drive train system receives the mechanical power and electrical torque, and outputs the

shaft torque T_{tg}, the machine input torque T_m, the rotor angular speed ω_r, and the turbine speed ω_t, Fig. 3.5. The mechanical shaft is often represented by a two-mass model. These masses represent the machine rotor and the turbine. The spring-damper model is often used to obtain the linearized equations describing the mechanical shaft. The values of damping and spring constants should be adjusted for a two-pole machine representation at the electrical side. The state-space representation of the mechanical part is then:

$$\frac{d}{dt}\begin{pmatrix}\omega_m\\ \omega_r\\ T_{sh}\end{pmatrix} = \begin{pmatrix}\frac{-D_t - D_{sh}}{2H_t} & \frac{D_{sh}}{2H_t} & \frac{-1}{2H_t}\\ \frac{D_{sh}}{H_g} & \frac{-D_g - D_{sh}}{2H_g} & \frac{1}{2H_g}\\ K_{sh}\omega_b & -K_{sh}\omega_b & 0\end{pmatrix} + \begin{pmatrix}\frac{1}{2H_t} & 0\\ 0 & \frac{-1}{2H_g}\\ 0 & 0\end{pmatrix}\begin{pmatrix}T_m\\ T_e\end{pmatrix} \tag{3.44}$$

$$T_e = X_m(i_{ds}i_{qr} - i_{qs}i_{dr}) \tag{3.45}$$

where ω_m is the turbine speed, T_{sh} is the torque at the shaft segment between the turbine and the induction generator (IG), and H_t and H_g are the inertia constants of the turbine and IG, respectively. D_t and D_g are the turbine and IG mechanical damping coefficients, D_{sh} is the damping coefficient of the flexible coupling between the turbine and the IG, and K_{sh} is the shaft stiffness. The electrical torque is also obtained from (3.45).

3.3 Transmission Line

The constant-parameter (frequency-independent) transmission line model is used in EMT simulations due to its high computational speed and precise behavior during the transients. A series impedance (resistance, inductance and capacitance) is used as a linear model of the transmission line in the analysis and design of the damping controller. The state-space representation of the transmission line can be detailed as:

$$\frac{di_{Ld}}{dt} = \frac{\omega_b}{X}(v_{ds} - X i_{Lq} - R i_{Ld} - v_{Cd} - E_d) \tag{3.46}$$

$$\frac{di_{Lq}}{dt} = \frac{\omega_b}{X}(v_{qs} + X i_{Ld} - R i_{Lq} - v_{Cq} - E_q) \tag{3.47}$$

$$\frac{dv_{Cd}}{dt} = \omega_b X_C(i_{Ld} - \frac{v_{Cq}}{X_C}) \tag{3.48}$$

$$\frac{dv_{Cq}}{dt} = \omega_b X_C(i_{Lq} + \frac{v_{Cd}}{X_C}) \tag{3.49}$$

where E_d and E_q are the infinite-bus voltages in the dq-frame considering the DFIG terminal voltage as reference. v_{Cq}, v_{Cd}, i_{Lq}, and i_{Ld} are the capacitor voltages and inductance currents

of the transmission line in the dq-frame, respectively.

In the wind farm linearized model, the DFIG transformer, the collector grid, the Thevenin equivalent circuit of the power system and the wind farm transformer are connected in series. Therefore, their impedances can be appended to the transmission line. It should be mentioned that the power system behind the infinite bus is represented by its equivalent Thevenin circuit $R_{Th}+jX_{Th}$. Thus, R and X, the active and reactive parts of the transmission line impedance used in (3.46)-(3.49) can be obtained as:

$$\begin{aligned} X &= X_{Line} + X_{dfig_{trans}} + X_{WF_{trans}} + X_{Th} + X_{collector} \\ R &= R_{Line} + R_{dfig_{trans}} + R_{WF_{trans}} + R_{Th} + R_{collector} \end{aligned} \tag{3.50}$$

where $X_{collector}$, $R_{collector}$, $X_{WF_{trans}}$, $R_{WF_{trans}}$, $X_{dfig_{trans}}$, and $R_{dfig_{trans}}$ denote the collector grid, the wind farm transformer, and the DFIG transformer reactances and resistances, respectively. The collector grid is often modeled by an PI equivalent circuit in EMT simulations, Fig. 3.6. It should be noted that all of the shunt branches are disregarded due to their marginal impact on the subsynchronous stability.

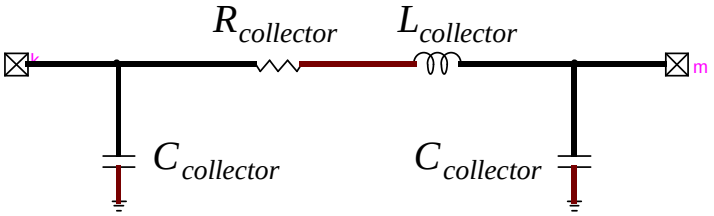

Figure 3.6 Collector model.

3.4 Choke Filter

A choke filter is used in the DFIG structure to make the waveform as sinusoidal as possible and to filter out the high-frequency harmonics injected by the converters, Fig. 3.7. The choke filter is described by:

$$V_g - V_s = Z_{Choke} I_g \tag{3.51}$$

Applying the Park transformation yields:

$$v_{chd} = L_{choke} \frac{di_{dg}}{dt} + \omega_s L_{Choke} i_{qg} \tag{3.52}$$

$$v_{chq} = L_{choke}\frac{di_{qg}}{dt} - \omega_s L_{Choke} i_{dg} \tag{3.53}$$

The algebraic equations in the dq-frame are expressed as:

$$v_{dg} - R_{choke} i_{dg} - v_{chd} = v_{ds} \tag{3.54}$$

$$v_{qg} - R_{choke} i_{qg} - v_{chq} = v_{qs} \tag{3.55}$$

Therefore, the linear equations representing the choke filter in per-unit system are:

$$\frac{di_{dg}}{dt} = \frac{\omega_b}{L_{choke}}(-v_{ds} - R_{choke} i_{dg} + v_{dg} - L_{choke}\omega_s i_{qg}) \tag{3.56}$$

$$\frac{di_{qg}}{dt} = \frac{\omega_b}{L_{choke}}(-v_{qs} - R_{choke} i_{qg} + v_{qg} + L_{choke}\omega_s i_{dg}) \tag{3.57}$$

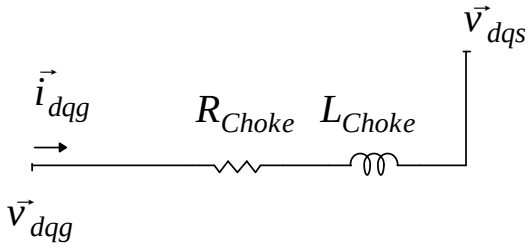

Figure 3.7 Choke filter.

3.5 Harmonic Filter

Two band-pass harmonic filters are often incorporated in the DFIG terminals to remove the switching frequency harmonics produced by the converters, Fig. 3.8. The values of the resistances, inductances, and capacitances of the filters are obtained as:

$$C_{f_1} = \frac{Q_{gen} N_{gen}}{V_s^2 (2\pi f_n)} \tag{3.58}$$

$$C_{f_2} = C_{f_1} \tag{3.59}$$

$$L_{f_1} = \frac{N_{gen}}{C_{f_1}(n_1 2\pi f_n)^2} \tag{3.60}$$

$$L_{f_2} = \frac{N_{gen}}{C_{f_2}(n_2 2\pi f_n)^2} \tag{3.61}$$

$$R_{f_1} = \frac{QL_{f_1} n_1 (2\pi f_n)}{N_{gen}} \tag{3.62}$$

$$R_{f_2} = \frac{QL_{f_2} n_2 (2\pi f_n)}{N_{gen}} \tag{3.63}$$

where V_s is the stator line-to-line RMS voltage, Q_{gen} is the reactive power injected by the filters, and $Q = 1000$ is the quality factor of the filters. The parameters n_1 and n_2 are the carrier signal ratio and its second harmonic value, i.e., $n_2 = 2n_1$. The carrier signal ratio is defined as the ratio of the switching frequency of the GSC to the nominal frequency f_n.

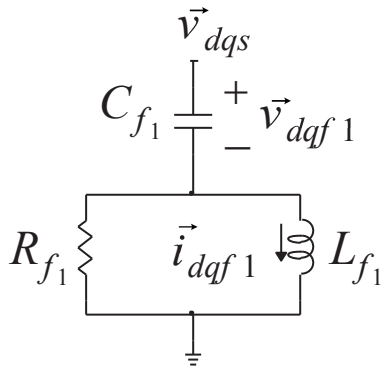

Figure 3.8 Harmonic filter structure.

The linearized model of the first harmonic filter is obtained as:

$$v_{ds} - v_{df1} = L_{f_1} \frac{di_{df_1}}{dt} + \omega_s L_{f_1} i_{qf1} \tag{3.64}$$

$$v_{qs} - v_{qf1} = L_{f_1} \frac{di_{qf1}}{dt} - \omega_s L_{f_1} i_{df1} \tag{3.65}$$

$$\frac{v_{ds} - v_{df1}}{R_{f_1}} + i_{df1} = C_{f_1} \frac{dv_{df1}}{dt} + \omega_s C_{f_1} v_{qf1} \tag{3.66}$$

$$\frac{v_{qs} - v_{qf1}}{R_{f_1}} + i_{qf1} = C_{f_1} \frac{dv_{qf1}}{dt} - \omega_s C_{f_1} v_{df1} \tag{3.67}$$

where v_{df1}, v_{qf1}, i_{df1} and i_{qf1} are the dq-components of the capacitor voltage and the inductance current of the first harmonic filter, respectively. After some manipulations, the equations in the per-unit system become:

$$\frac{di_{df1}}{dt} = \frac{\omega_b}{L_{f_1}} (v_{ds} - v_{df1} - \omega_s L_{f_1} i_{qf1}) \tag{3.68}$$

$$\frac{di_{qf1}}{dt} = \frac{\omega_b}{L_{f_1}} (v_{qs} - v_{qf1} + \omega_s L_{f_1} i_{df1}) \tag{3.69}$$

$$\frac{dv_{df1}}{dt} = \frac{\omega_b}{C_{f_1}}(\frac{v_{ds} - v_{df1}}{R_{f_1}} + i_{df1} - C_{f_1}\omega_s v_{qf1}) \tag{3.70}$$

$$\frac{dv_{qf1}}{dt} = \frac{\omega_b}{C_{f_1}}(\frac{v_{qs} - v_{qf1}}{R_{f_1}} + i_{qf1} + C_{f_1}\omega_s v_{df1}) \tag{3.71}$$

Similarly, we can obtain the second harmonic filter model. It should be noted that the DFIG terminal voltage appears in the IG, the choke filter and the harmonic filters equations. However, the DFIG terminal voltage is a function of other states and can be obtained from the harmonic filters equations as:

$$v_{ds} = \frac{1}{R_{f_1} + R_{f_2}}(R_{f_2}v_{df1} + R_{f_1}v_{df2} + R_{f_1}R_{f_2}(-i_{Ld} + i_{dg}) - i_{ds} - i_{df1} - i_{df2}) \tag{3.72}$$

$$v_{qs} = \frac{1}{R_{f_1} + R_{f_2}}(R_{f_2}v_{qf1} + R_{f_1}v_{qf2} + R_{f_1}R_{f_2}(-i_{Lq} + i_{qg}) - i_{qs} - i_{qf1} - i_{qf2}) \tag{3.73}$$

Therefore, the stator voltages in the dq-frame (i.e., (3.72) and (3.73))) can be substituted in other equations to obtain the closed-loop state-space representation.

3.6 DC Link

The DC link schematic diagram is shown in Fig. 3.9. If the active power injected by the RSC exceeds that of the GSC, the DC bus voltage will increase. Conversely, the DC bus voltage will decrease if the active power of the RSC is less than that of the GSC. The following equation describes the dynamic behavior of the DC bus voltage.

$$\frac{dE_{DC}}{dt} = P_{RSC} + P_{GSC} - P_{Loss} \tag{3.74}$$

where

$$P_{RSC} = i_{qr}v_{qr} + i_{dr}v_{dr} \tag{3.75}$$

$$P_{GSC} = i_{qg}v_{qg} + i_{dg}v_{dg} \tag{3.76}$$

$$P_{Loss} = \frac{V_{DC}^2}{R_{DC}} \tag{3.77}$$

Therefore, the differential equation describing the DC link voltage is:

$$\frac{dV_{DC}}{dt} = \frac{\omega_b}{C_{DC}V_{DC}}(i_{qr}v_{qr} + i_{dr}v_{dr} + i_{qg}v_{qg} + i_{dg}v_{dg} - \frac{V_{DC}^2}{R_{DC}}) \tag{3.78}$$

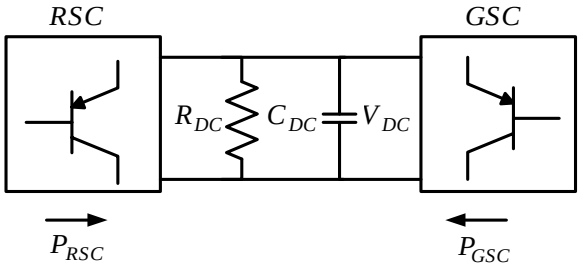

Figure 3.9 DC link capacitor.

3.7 Voltage and Current Filters

The first- and second-order low-pass filters (LPFs) are incorporated into the DFIG current and voltage control loops, as shown in Fig. 3.10. It should be noted that the output signals of these filters are used in the control system. The equations (3.79)-(3.87) describe the corresponding dynamics in the per-unit system.

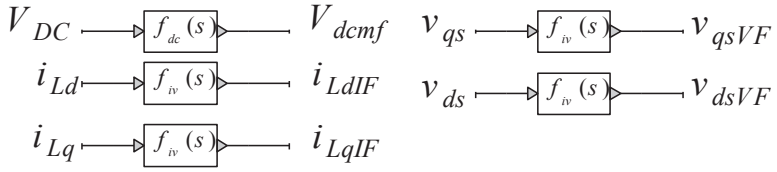

Figure 3.10 Current and voltage filters.

$$\frac{dv_{dsVF}}{dt} = (\frac{\omega_b}{T_f})(v_{ds} - v_{dsVF}) \tag{3.79}$$

$$\frac{dv_{qsVF}}{dt} = (\frac{\omega_b}{T_f})(v_{qs} - v_{qsVF}) \tag{3.80}$$

$$\frac{di_{LdIF}}{dt} = (\frac{\omega_b}{T_f})(i_{Ld} - i_{LdIF}) \tag{3.81}$$

$$\frac{di_{LqIF}}{dt} = (\frac{\omega_b}{T_f})(i_{Lq} - i_{LqIF}) \tag{3.82}$$

In (3.79)-(3.82), $T_f = 75\ ms$ is the time constant of the filter, and subscripts IF and VF are used to refer to the output currents and voltages of the filters, respectively. The second-order filter is incorporated into the DC voltage loop whose parameters W_{1dc}, F_{dc} and W_{2dc} are designed to be:

$$F_{dc} = \frac{141 \times 2}{2\pi \times 60} \tag{3.83}$$

$$W_{1dc} = \frac{1}{(2\pi F_{dc})^2} \tag{3.84}$$

$$W_{2dc} = \frac{\sqrt{2}}{2\pi F_{dc}} \tag{3.85}$$

Using these parameters, the state-space representation of the DC voltage filter is as:

$$\frac{dV_{dcmf}}{dt} = \omega_b x_{dcf} \tag{3.86}$$

$$\frac{dx_{dcf}}{dt} = \frac{\omega_b}{W_{1dc}}(V_{DC} - V_{dcmf} - W_{2dc}x_{dcf}) \tag{3.87}$$

3.8 Control Systems

In a typical DFIG wind turbine, both the RSC and the GSC are controlled based on vector control techniques. These techniques are utilized to provide decoupled control of active and reactive powers. The currents and voltages are projected on a rotating reference frame based on either the AC flux or the AC voltage.

The control scheme of the DFIG is illustrated in Fig. 3.11, where i_{qr} and i_{dr} are the q- and d-axis currents of the RSC, i_{qg} and i_{dg} are the q- and d-axis currents of the GSC, V_{DC} is the DC bus voltage, P_{dfig} is the active power output of the DFIG, and V_{dfig} is the positive-sequence component of the DFIG terminal voltage. In Fig. 3.11 and thereafter, the subscript ref is used to indicate the reference values.

In the control scheme of Fig. 3.11, the RSC and the GSC operate in the stator flux reference (SFR) and the stator voltage reference (SVR) frames, respectively. The DFIG power P_{dfig} and its voltage V_{dfig} are controlled using i_{qr} and i_{dr}, respectively. On the other hand, i_{dg} is used to regulate the DC bus voltage V_{DC} and i_{qg} is used to supply the grid with the required reactive power when the system is subjected to faults. Both the RSC and the GSC include two control loops, namely, the outer and the inner loop controllers. The slow outer loop control generates the reference signals for the currents ($i_{dr_{ref}}$, $i_{qr_{ref}}$, $i_{dg_{ref}}$ and $i_{qg_{ref}}$), and the fast inner loop control generates the control signals which correspond to converters terminal voltages. The inner loop control signals are used to generate the modulated switching pattern. The maximum power point tracking (MPPT) algorithm and the WFC determine the reference signals of the DFIG active power output ($P_{dfig_{ref}}$) and its positive-sequence voltage ($V_{dfig_{ref}}$), respectively.

In Fig. 3.11, i_{dr_m} is a compensating term for the reactive current absorbed by the IG and is

approximated by:

$$i_{dr_m} = \frac{V_{dfig}}{X_m} \tag{3.88}$$

where X_m is the magnetizing reactance of the induction machine.

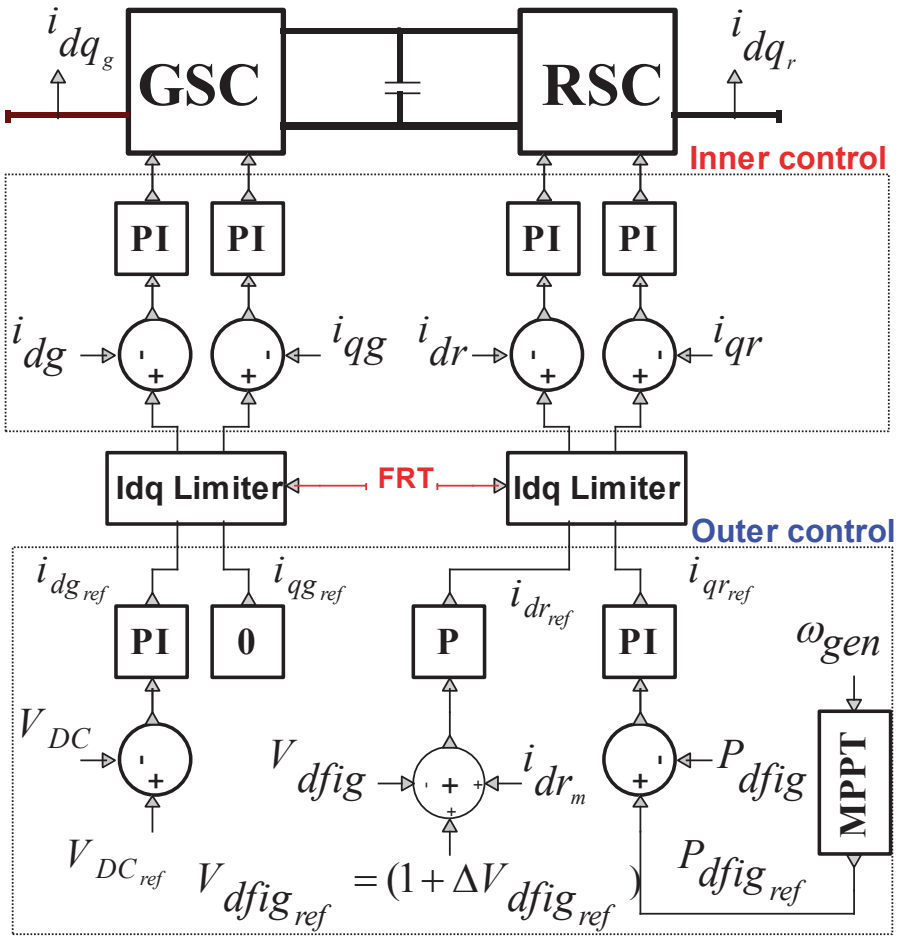

Figure 3.11 DFIG control system.

3.8.1 Rotor Side Converter (RSC) Control

In this section, the RSC control circuit and its linearized equations are discussed. The inner current control loops of the RSC (i.e., PI controllers) are expressed as:

$$v_{dr} = (K_{Pr} + \frac{K_{Ir}}{s})(i_{dr_{ref}} - i_{dr}) + FF_{dr} \tag{3.89}$$

$$v_{qr} = (K_{Pr} + \frac{K_{Ir}}{s})(i_{qr_{ref}} - i_{qr}) + FF_{qr} \tag{3.90}$$

where v_{dr} and v_{qr} are the RSC terminal voltages, and K_{Pr} and K_{Ir} are the PI control parameters. FF_{dr} and FF_{qr} are the feedforward signals calculated as:

$$FF_{qr} = v_{qrFF} = \frac{-(1-\omega_r)(L_{rc} i_{dr})}{\Gamma^2} \tag{3.91}$$

$$FF_{dr} = v_{drFF} = \frac{\frac{(1-\omega_r)(X_s + L_{rc} i_{qr})}{\Gamma} + X_s i_{qs}}{\Gamma} \tag{3.92}$$

$$L_{rc} = \Gamma L_{ls} + \Gamma^2 L_{lr} \tag{3.93}$$

where $\Gamma = \dfrac{L_s}{L_m}$. The outer loops provide the reference signals for the inner loops of the RSC and GSC. The outer-loop dynamics of the RSC are obtained as:

$$i_{dr_{ref}} = K_v(1 + \Delta V_{dfig_{ref}} - V_{dfig}) + i_{dr_m} \tag{3.94}$$

$$i_{qr_{ref}} = (K_{PP} + \frac{K_{PP}}{s})(P_{dfig_{ref}} - P_{dfig}) \tag{3.95}$$

where K_v is the gain of the voltage regulator, and K_{PP} and K_{IP} are the parameters of the PI regulator in the q-axis direction. It should be noted that in the control circuit of DFIG, V_{dfig} and P_{dfig} are calculated using the outputs of the low-pass filters (detailed in Section. 3.7) as:

$$V_{dfig} = \sqrt{v_{dsVF}^2 + v_{qsVF}^2} \tag{3.96}$$

$$P_{dfig} = v_{dsVF} i_{LdIF} + v_{qsVF} i_{LqIF} \tag{3.97}$$

After some simplifications, the linearized model of the RSC including its control circuit will be obtained as shown in Fig. 3.12 and Fig. 3.13. The apostrophe sign ($'$) represents the derivative with respect to time, and the asterisk sign (*) is used to denote the intermediate variables which are added to the feedforward signals to produce the references. The equations (3.98)-(3.101) describe the linearized model of the RSC for the d-axis control loop.

$$i_{dr}^* = (V_{dfig_{ref}} - V_{dfig})K_v + \frac{V_{dfig}}{X_m} \tag{3.98}$$

$$i_{dr_{ref}} = i_{dr}^* + i_{drFF} \tag{3.99}$$

$$\frac{dx_{dr}}{dt} = K_{Ir}(i_{dr_{ref}} - i_{dr}) \tag{3.100}$$

$$v_{dr} = x_{dr} + K_{Pr}(i_{dr_{ref}} - i_{dr}) + v_{drFF} \tag{3.101}$$

The q-axis control loop of the RSC is shown in Fig. 3.13. Equations (3.102)-(3.106) describe

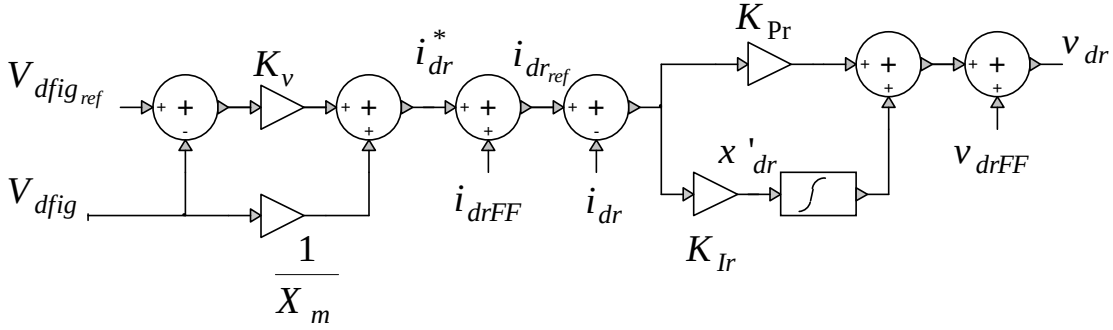

Figure 3.12 Simplified schematic diagram of the RSC in d-axis control.

the linear model of the RSC used by the q-axis controller.

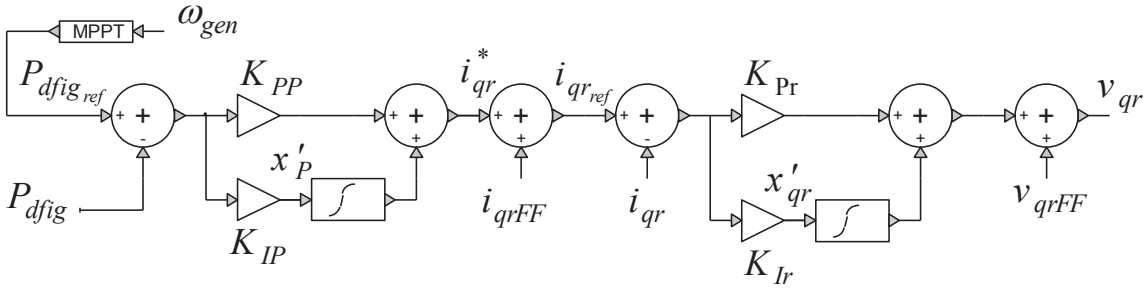

Figure 3.13 Simplified schematic diagram of the RSC in q-axis control.

$$\frac{dx_P}{dt} = K_{IP}(P_{dfig_{ref}} - P_{dfig}) \tag{3.102}$$

$$i^*_{qr} = K_{PP}(P_{dfig_{ref}} - P_{dfig}) + x_P \tag{3.103}$$

$$i_{qr_{ref}} = i^*_{qr} + i_{qrFF} \tag{3.104}$$

$$\frac{dx_{qr}}{dt} = K_{Ir}(i_{qr_{ref}} - i_{qr}) \tag{3.105}$$

$$v_{qr} = x_{qr} + K_{Pr}(i_{qr_{ref}} - i_{qr}) + v_{qrFF} \tag{3.106}$$

3.8.2 Grid Side Converter (GSC) Control

The inner current control loops of the GSC are expressed as:

$$v_{dg} = (K_{Pg} + \frac{K_{Ig}}{s})(i_{dg_{ref}} - i_{dg}) + FF_{dg} \tag{3.107}$$

$$v_{qg} = (K_{Pg} + \frac{K_{Ig}}{s})(i_{qg_{ref}} - i_{qg}) + FF_{qg} \tag{3.108}$$

where v_{dg} and v_{qg} are the GSC terminal voltages, K_{Pg} and K_{Ig} are the PI control parameters, and FF_{dg} and FF_{qg} are feedforward signals as given by:

$$FF_{qg} = v_{qgFF} = v_{qs} + R_{choke} i_{qg} - X_{choke} i_{dg} \tag{3.109}$$

$$FF_{dg} = v_{dgFF} = v_{ds} + R_{choke} i_{dg} + X_{choke} i_{qg} \tag{3.110}$$

The GSC outer loop should regulate the DC link voltage and it can be expressed as:

$$i_{dg_{ref}} = (K_{Pdc} + \frac{K_{Idc}}{s})(V_{DC_{ref}} - V_{dcmf}) \tag{3.111}$$

where K_{Pdc} and K_{Idc} are PI control parameters. The reference current $i_{qg_{ref}}$ is set to zero as the GSC often operates at unity power-factor during normal operation. The high-voltage-ride-through (HVRT) and the low-voltage-ride-through (LVRT) blocks are appended to the outer loop of the GSC q-axis to provide the system with an appropriate amount of reactive power to compensate for the DFIG terminal voltage deviations.

The equations (3.112)-(3.116) describe the d-axis control loop of the GSC, Fig. 3.14.

$$\frac{dx_{dc}}{dt} = K_{Idc}(V_{DC_{ref}} - V_{dcmf}) \tag{3.112}$$

$$i^*_{dg} = K_{Pdc}(V_{DC_{ref}} - V_{dcmf}) + x_{dc} \tag{3.113}$$

$$i_{dg_{ref}} = i^*_{dg} + i_{dgFF} \tag{3.114}$$

$$\frac{dx_{dg}}{dt} = K_{Ig}(i_{dg_{ref}} - i_{dg}) \tag{3.115}$$

$$v_{dg} = v_{dgFF} + x_{dg} + K_{Pg}(i_{dg_{ref}} - i_{dg}) \tag{3.116}$$

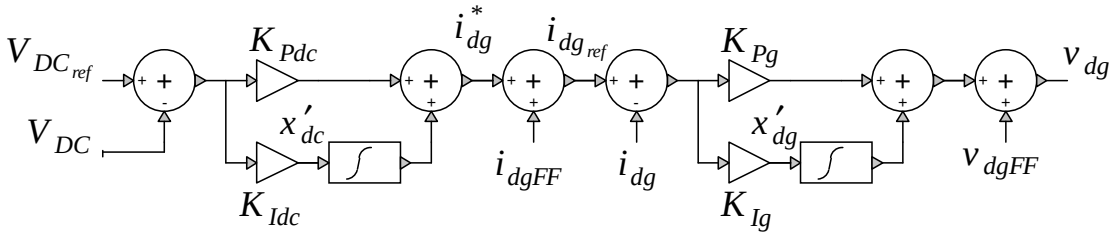

Figure 3.14 Simplified schematic diagram of the GSC in d-axis control.

The equations of the q-axis of the GSC are given in (3.117) and (3.118), Fig. 3.15. The HVRT and LVRT blocks are not considered in the linearization due to their minor effects on the subsynchronous phenomenon. However, they are included in the model for EMT simulations.

$$\frac{dx_{qg}}{dt} = K_{Ig}(0 - i_{qg}) \tag{3.117}$$

$$v_{qg} = v_{qgFF} + x_{qg} + K_{Pg}(0 - i_{qg}) \tag{3.118}$$

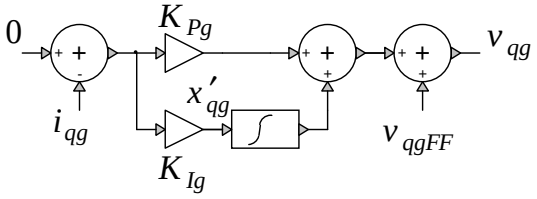

Figure 3.15 Simplified schematic diagram of the GSC in q-axis control.

3.9 Linearization

The GSC and the RSC control systems are employed to control the DFIG over a range of operating points. However, during SSCI oscillations, those controllers may not be sufficient to guarantee the system stability. Therefore, a supplementary controller should be added to the existing control systems to ensure the stability of the power system. In this thesis, the overall closed-loop system refers to the system obtained by adding this supplementary controller to the existing control system. Fig. 3.16 shows the block diagram of the closed-loop system including its supplementary SSCI damping controller. To design the SSCI damping controller, the dynamical equations of the open-loop system, as shown in Fig. 3.16, are first derived. Considering $\mathbf{u} \in \mathcal{R}^r$ and $\mathbf{y} \in \mathcal{R}^m$ to be the output and input vectors of the SSCI supplementary controller, the state-space representation of this system can be expressed as:

$$\dot{\mathbf{x}} = f(\mathbf{x}, \mathbf{u}) \tag{3.119}$$

$$\mathbf{y} = h(\mathbf{x}, \mathbf{u}) \tag{3.120}$$

where $\mathbf{x} \in \mathcal{R}^n$ is the vector of the system states, and f is a nonlinear function imposed by the nonlinear dynamics of the induction machine. The details of this function are described in Appendix A. This state-space representation can be used in the next chapters to design

the SSCI supplementary controller. The state vector $\mathbf{x}$ is defined as:

$$\mathbf{x} = (\mathbf{x}_{DC}, \mathbf{x}_{IG}, \mathbf{x}_{mech}, \mathbf{x}_{sys}, \mathbf{x}_{HF}, \mathbf{x}_{CNTL}, \mathbf{x}_{IVF})^T \tag{3.121}$$

In (3.121), $\mathbf{x}_{DC}$, $\mathbf{x}_{IG}$, $\mathbf{x}_{mech}$, $\mathbf{x}_{sys}$, $\mathbf{x}_{HF}$, $\mathbf{x}_{CNTL}$ and $\mathbf{x}_{IVF}$ denote, respectively, the states of the following parts of the system: the DC link, the induction machine, the mechanical system, the power system, the harmonic filters, the control systems, and the voltage/current filters. The output vector consists of the currents of the converters in the dq-frame, i.e., $\mathbf{y} = [i_{dr}, i_{qr}, i_{dg}, i_{qg}]$. The outputs of the supplementary controller are added into the inner control loops of the DFIG; this is expressed as: $\mathbf{u} = [u_{dr}, u_{qr}, u_{dg}, u_{qg}]$.

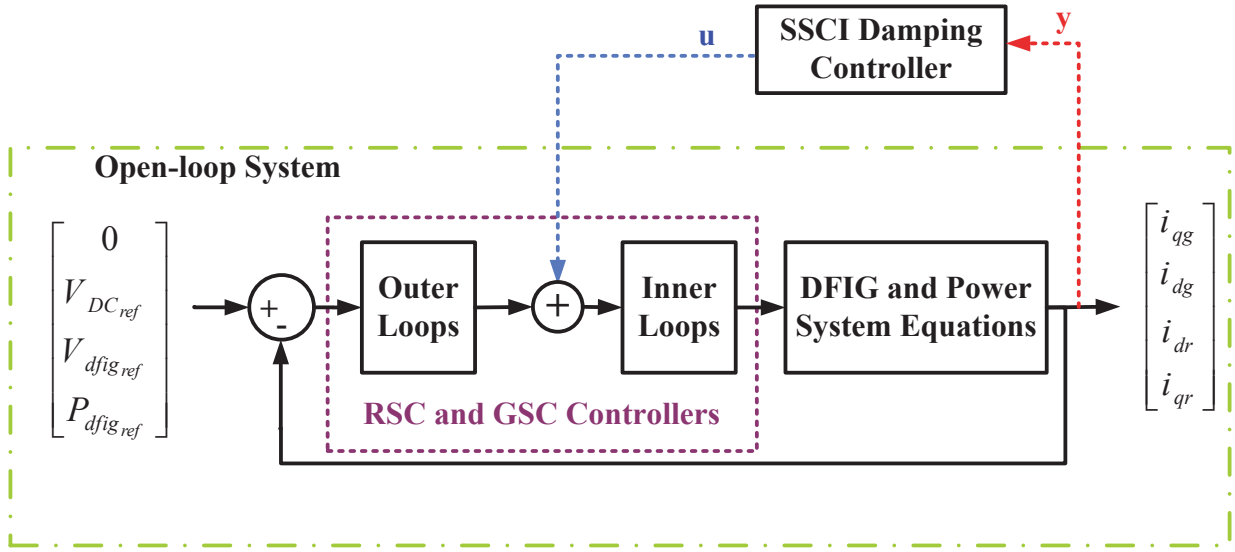

Figure 3.16 The schematic diagram of the closed-loop system.

To calculate the equilibrium point of the system $(\mathbf{x}_0, \mathbf{u}_0)$, we set $\dot{\mathbf{x}}$ equal to zero. More precisely, i.e.,

$$\dot{\mathbf{x}} = f(\mathbf{x}, \mathbf{u}) = 0 \rightarrow \mathbf{x}_0, \ \ \mathbf{u}_0 \tag{3.122}$$

Using the fzero command of MATLAB, the equilibrium point is numerically obtained. Then, using the Taylor series expansion of $f(\mathbf{x}, \mathbf{u})$ about $(\mathbf{x}_0, \mathbf{u}_0)$, the following linear model is obtained:

$$\begin{aligned} \dot{\mathbf{x}} &= \mathbf{A}\mathbf{x} + \mathbf{B}\mathbf{u} \\ \mathbf{y} &= \mathbf{C}\mathbf{x} + \mathbf{D}\mathbf{u} \end{aligned} \tag{3.123}$$

In (3.123), the Jacobian matrices **A**, **B**, **C**, and **D** are computed as follows:

$$\mathbf{A} = \frac{\partial f}{\partial \mathbf{x}}|_{(\mathbf{x}_0,\mathbf{u}_0)},\ \mathbf{B} = \frac{\partial f}{\partial \mathbf{u}}|_{(\mathbf{x}_0,\mathbf{u}_0)},\ \mathbf{C} = \frac{\partial h}{\partial \mathbf{x}}|_{(\mathbf{x}_0,\mathbf{u}_0)},\ \mathbf{D} = \frac{\partial h}{\partial \mathbf{u}}|_{(\mathbf{x}_0,\mathbf{u}_0)} \tag{3.124}$$

In the next chapters, the linear model of the described system obtained using the linearization technique will be used to design the supplementary damping controller. Moreover, we will use this linear model to perform the analysis of the subsynchronous phenomenon.

3.10 EMT Model of the Wind Farm

To simulate the overall system including the wind farm and the power system in EMTP-RV software [82], a detailed model of the system is used. This detailed modeling takes into account the fault-ride-through (FRT) function, the wind farm controller (WFC), and all nonlinear functions required to obtain the precise transient behavior of the system. The input parameters of the EMTP-RV model and the wind farm parameters are summarized in Tables 3.1 and 3.2. It should be mentioned that the parameters of the RSC inner controller can be obtained in terms of its desired rise-time, i.e.,

$$\begin{aligned} K_{Pr} &= L_{rc}\frac{log(9)}{\omega_b T_{rise-rsc}} \\ K_{Ir} &= \frac{log(9)\Gamma^2 R_{r_{pu}}}{T_{rise-rsc}} \end{aligned} \tag{3.125}$$

The parameters of the inner loop controller of the GSC can be obtained similarly.

3.10.1 Control System

In the EMT model of the wind farm, the measured voltages in the abc-frame are first per-unitized, and then low-pass filtered. The order of the LPFs and their cut-off frequencies are obtained from a realistic wind turbine model. The filtered signals are transferred to the computation block in which the corresponding dq-frame signals (SFR for RSC and SVR for RSC) and active/reactive power components are calculated. The protection block and the control circuit also use the outputs of this computation block. The control circuit produces the inputs to an average model of an IGBT-based converter, and the protection block detects possible over-voltages and over-currents. The FRT signal is applied to a limiter block in the current reference path to restrict the active current injection subsequent to a fault.

Table 3.1 Wind farm parameters in the EMTP model.

Parameter	value	Description
Mean wind speed	$11.24\frac{m}{s}$	Nominal mean wind speed
WFC mode select	1	1(Q-control) 2(V-control) 3(PF control)
Q_{POI}	0	Reactive power at POI
PF_{POI}	1	Power-factor at POI
f_n	60	Nominal frequency
N_{gen}	133	Number of WTs in the wind farm
N_{gen} in service	133	Number of WTs in service
P_{gen}	1.5 MW	Rated active power of one wind generator
S_{gen}	1.667 MVA	Rated apparent power of one wind generator
$V_{gen_{KVRMSLL}}$	0.575 kV	Generator nominal voltage kV RMS line to line
$V_{collector_{KVRMSLL}}$	34.5 kV	Collector grid nominal voltage kV RMS line to line
$V_{POI_{KVRMSLL}}$	500 kV	Transmission grid voltage kV RMS line to line
$S_{dfig_{trans}}$	1.75 MVA	Rated apparent power of DFIG transformer
$X_{dfig_{trans}}$	0.06 pu	DFIG transformer inductance in pu
$R_{dfig_{trans}}$	0.002 pu	DFIG transformer resistance in pu
$R_{collector}$	0.04Ω	Equivalent collector resistance in Ohms
$L_{collector}$	12×10^{-5} H	Equivalent collector inductance in H
$C_{collector}$	23.5×10^{-6} F	Equivalent collector capacitance in F
$S_{WF_{trans}}$	222 MVA	Rated apparent power of wind farm transformer
$X_{WF_{trans}}$	0.15 pu	Wind farm transformer inductance in pu
$R_{WF_{trans}}$	0.005 pu	Wind farm transformer resistance in pu
$Tap_{WF_{trans}}$	1	Wind farm transformer tap ratio
$f_{sampling_{RSC}}$	11.25KHz	Sampling rate at RSC
$f_{sampling_{GSC}}$	22.5KHz	Sampling rate at GSC
$f_{PWM_{RSC}}$	2250Hz	PWM frequency at RSC
$f_{PWM_{GSC}}$	4500 Hz	PWM frequency at GSC
$T_{risetime_{RSC}}$	20ms	RSC rise time
$T_{risetime_{GSC}}$	10ms	GSC rise time
K_v	2	Voltage regulation gain
K_p	1	Proportional gain of P control loop
T_{ip}	0.1	Integral gain of P control $Ki = \frac{K_p}{T_{ip}}$

Table 3.2 Internal wind farm parameters.

H_t	4 s	K_{tg}	1.2 pu
D_{tg}	1.5 pu	n_{pp}	3
H_{gen}	0.9 s	D_{gen}	0
R_s	0.033 pu	L_{ls}	0.18 pu
R_r	0.026 pu	L_{lr}	0.16 pu
L_m	2.9 pu	K_{tg}	1.2
R_{choke}	0.015 pu	L_{choke}	1.5 pu

Wind Farm Controller (WFC)

The reactive power control in a wind farm is based on the secondary voltage control concept in which the WFC determines the voltage reference of the outer loop control system of the RSC. The outer loop controller is a constant gain K_v, Fig. 3.17. Therefore, the desired reactive power injected to the POI is determined by the WFC. The WFC can also regulate the voltage (V-control mode) or the power-factor (PF-control mode) at the POI. Assuming that the WFC operates in V-control mode, the reactive power reference $Q_{POI_{ref}}$ in Fig. 3.17 is the output of the proportional voltage controller, i.e.,

$$Q_{POI_{ref}} = K_{V_{POI}}(V_{POI_{ref}} - V_{POI}) \tag{3.126}$$

In (3.126), V_{POI} is the positive-sequence voltage at the POI. If the WFC operates in the PF-control mode, the active power at the POI (P_{POI}) and the pre-specified power-factor ($PF_{POI_{ref}}$) will be used to obtain the injected reactive power ($Q_{POI_{ref}}$). To avoid any over voltage following a fault removal or a severe voltage sag at the POI (e.g., due to a fault), the output signal of the WFC ($\Delta V_{dfig_{ref}}$) is kept constant by blocking its input ($Q_{POI_{ref}} - Q_{POI}$). In this study, the WFC is assumed to operate in Q-control mode in order to independently control the injected reactive power. However, the other operating modes (i.e., the PF-control mode or the V-control mode) can be used similarly.

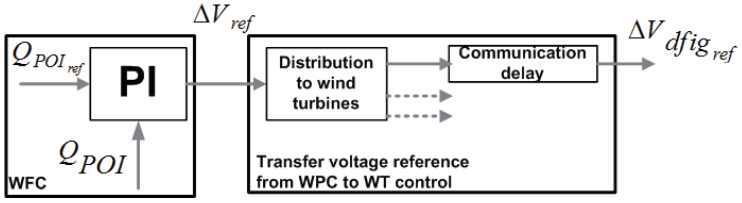

Figure 3.17 Reactive power control at the POI.

3.10.2 Protection System

The protection scheme of the DFIG includes the following functions:

1. Resistive chopper.
2. Crowbar.
3. Low- and over-voltage relays.
4. RSC and GSC over-current relays which temporarily block the converters during over current.
5. Voltage sag detector which temporarily disables the converters to withstand the FRT operation against faults that occur outside of the wind farm.

Fault Ride Through (FRT) Function

Under normal operation, the GSC injects zero reactive power ($i_{qg_{ref}} = 0$), while the active current injection has the main priority for the RSC control circuit, i.e.,

$$\begin{aligned} i_{dr_{ref}} &< I_{dr}^{lim} \quad , I_{dr}^{lim} = 1pu \\ i_{qr_{ref}} < I_{qr}^{lim} &= \sqrt{(I_r^{lim})^2 + (i_{dr_{ref}})^2)} \quad , I_r^{lim} = 1.1pu \end{aligned} \tag{3.127}$$

where I_{dr}^{lim}, I_{qr}^{lim} and I_r^{lim} are the limits of the dq-components and the limit of the magnitude of the RSC current, respectively. A wind turbine is always equipped with an FRT function to fulfill the grid code requirements regarding voltage support [83], Fig. 3.19. In Fig. 3.19, $I_{reactive}(pu)$ and $V(pu)$ are the DFIG reactive current and voltage, respectively. Upon the FRT activation, the DFIG injects reactive current whose amount is proportional to the voltage deviation.

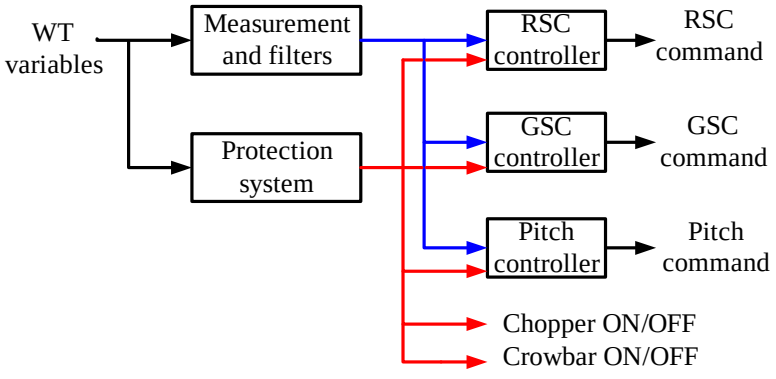

Figure 3.18 Protection of the wind farm.

The FRT function is activated when the voltage deviation, i.e., $V_{dfig} - 1$ pu, exceeds the pre-defined value of V_{FRT-ON}, and is deactivated when the voltage deviation stays less than the value $V_{FRT-OFF}$ for a minimum pre-specified release time t_{FRT} [84]. During the FRT operation, the RSC control circuit primarily injects reactive current by reversing the d- and q-axis current limits in (3.127). Due to the consumption of reactive power by the induction generator, the RSC reactive current contribution may not be sufficient to satisfy the grid code requirement; therefore, the GSC is designed to inject reactive currents during the faults in such circumstances.

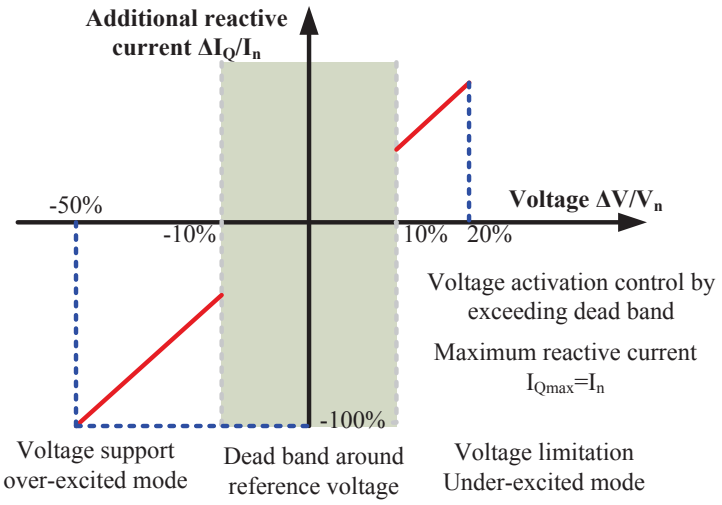

Figure 3.19 Reactive power control at the POI.

3.11 Benchmarks

The following four topologies for the power system and wind farm are used as benchmarks in this thesis.

1. Single-mode aggregated benchmark
2. Single-mode detailed benchmark
3. Multi-mode benchmark
4. IEEE SSR first benchmark model [38]

It should be noted that the benchmarks 1, 2, and 3 are developed in this study. The IEEE SSR first benchmark model (benchmark 4) can be found in the literature as it is a well-established benchmark for SSR analysis of conventional plants [38].

3.11.1 Single-Mode Aggregated Benchmark

The DFIG-based wind farm shown in Fig. 3.20 consists of 266 wind turbines. Each turbine has 1.5 MW capacity and operates at 0.575 kV and 60 Hz. The power system includes two 500 kV transmission lines (lines A and B), Fig. 3.20. Two capacitor banks are placed at both ends of the line A (500 Km) to provide a 50% compensation level. In addition, two shunt reactors with a quality factor of 100 are also installed at both ends of Line A to prevent the Ferranti effect and to support the system voltage when the system is lightly loaded. The power systems at the end of lines A and B (100 km) are modeled with their Thevenin equivalent circuits. B1 and B2 are the circuit breakers of Line B. The operating times for the close and remote breakers are 60 ms and 80 ms, respectively. This structure is inspired by an actual power system. Following the disconnection of Line B, the wind farm becomes radially connected to the series capacitor compensated transmission line.

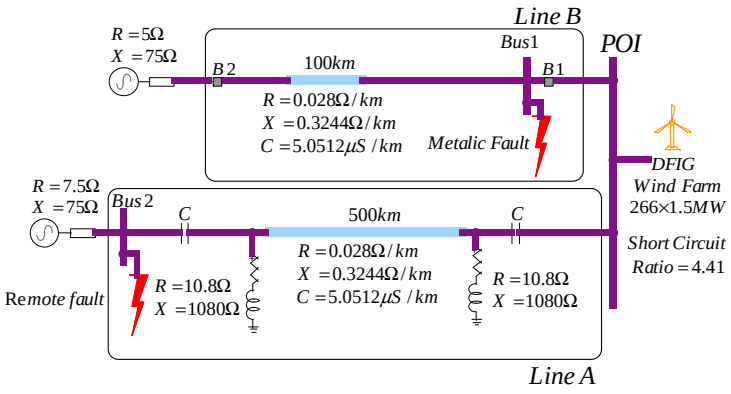

Figure 3.20 Single-mode benchmark with aggregated wind farm model.

3.11.2 Single-Mode Detailed Benchmark

In this benchmark, the wind farm consists of 268 DFIGs with 1.5 MW capacity operating at 575 V and 60 Hz. The wind farm is subdivided equally into four clusters as shown in Fig. 3.21. Each cluster is connected to the power system with a 34.5 kV feeder through a 500/34.5/34.5 kV delta-delta-grounded star three-winding transformer.

The wind turbines of cluster-1 and their internal transformers are represented using their aggregated model behind an RLC branch, Fig. 3.22. The internal circuit of cluster-2 and cluster-3 is comprised of five equivalent 34.5 kV feeders connected to the aggregated model of the DFIG wind turbines, Fig. 3.22. The parameters of these feeders are calculated using the aggregation method based on the active and reactive power loss of the feeder at 1 pu

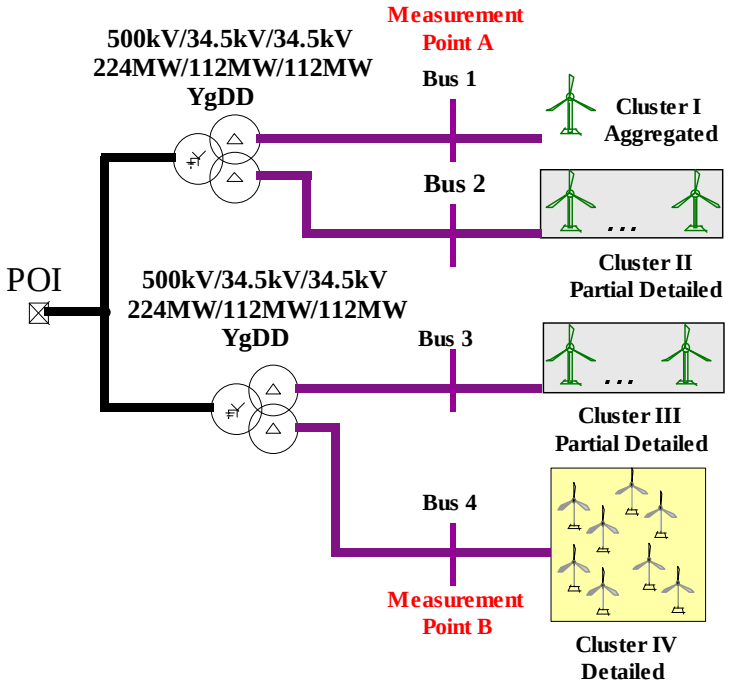

Figure 3.21 Single-mode benchmark with a detailed wind farm model.

power flow rating [85]. Cluster-4 consists of 67 DFIGs and is modeled precisely by including the complete collector grid, Fig. 3.23-Fig. 3.26. This cluster has 5 groups of DFIGs (18, 10, 15, 12 and 12 DFIG wind turbines) which are modeled in detail. This structure is inspired from an actual wind farm and used to illustrate the impact of aggregation on the system response. To simulate and study a more realistic wind farm scenario, the distribution of the wind speed over the turbines is assumed to be Gaussian. The data for the cables are provided in Table 3.3.

This structure has been proposed to compare the aggregated model of the system with its detailed model (i.e., by comparing cluster I and IV) in terms of damping and transient behavior. The voltage, the active power and the reactive power are measured at the measurement

Table 3.3 Cables data.

Cable	Resistance $(\frac{\Omega}{Km})$	Inductance $(\frac{H}{Km})$	Capacitance $(\frac{F}{Km})$
3/0 AWG	0.3815	44×10^{-5}	8×10^{-8}
350 kcmil	0.164	38×10^{-5}	10.5×10^{-8}
500 kcmil	0.125	37×10^{-5}	11.5×10^{-8}
750 kcmil	0.0778	35×10^{-5}	14×10^{-8}

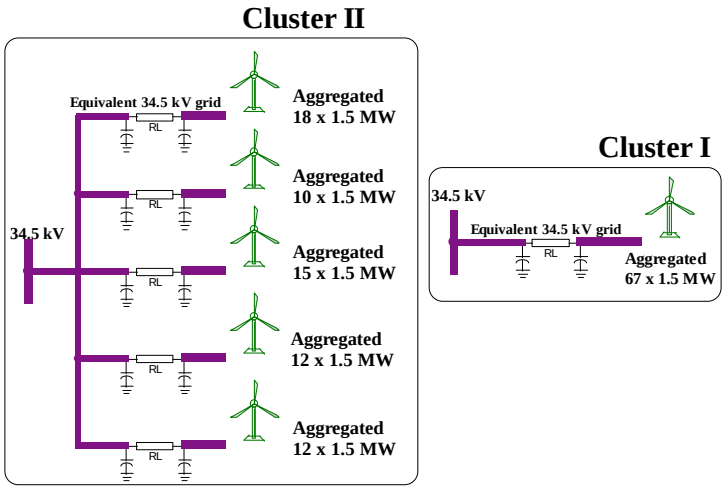

Figure 3.22 Cluster I and II model.

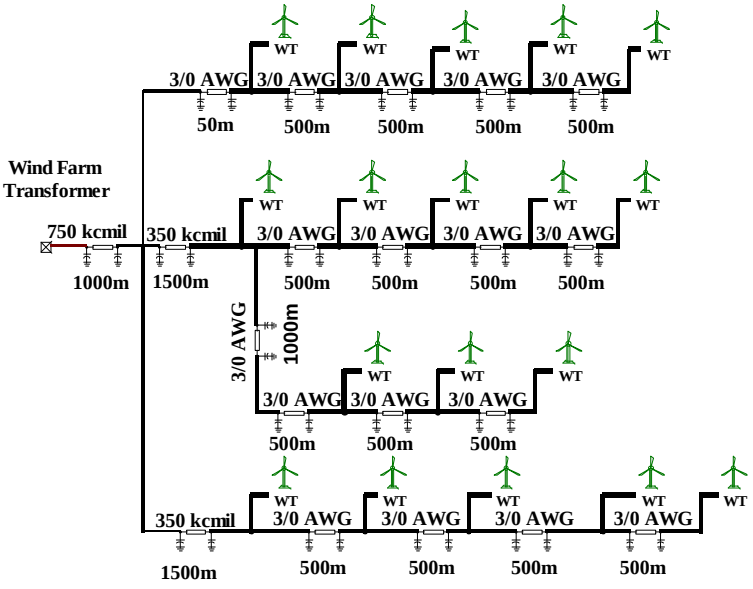

Figure 3.23 Cluster IV model (feeder including 18 DFIGs).

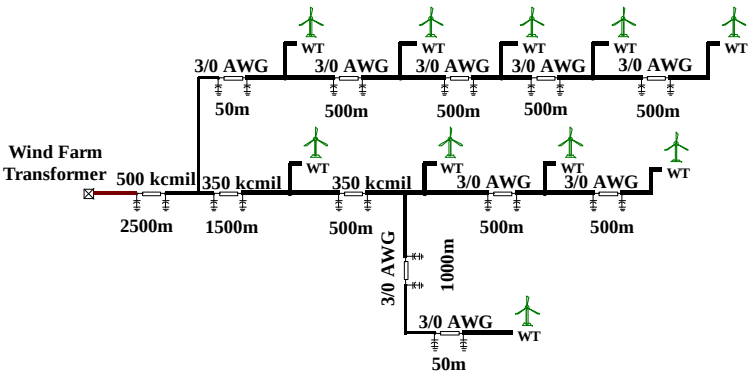

Figure 3.24 Cluster IV model (feeder including 10 DFIGs).

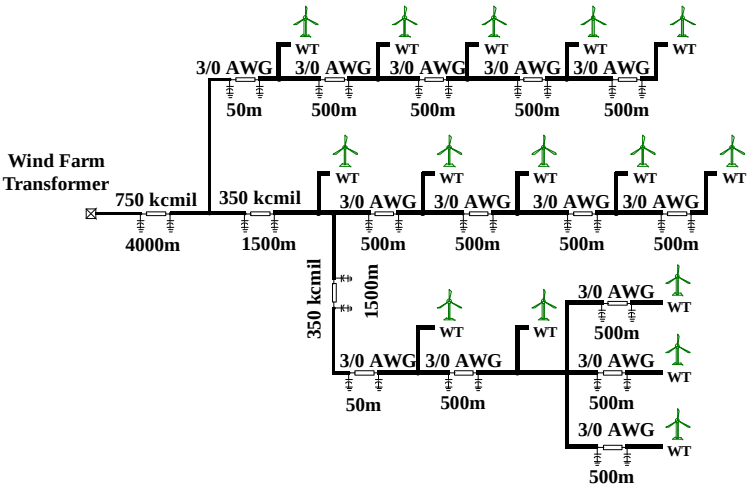

Figure 3.25 Cluster IV model (feeder including 15 DFIGs).

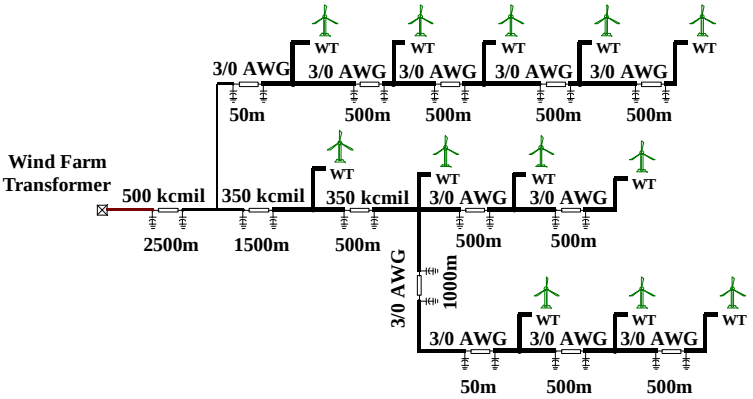

Figure 3.26 Cluster IV model (feeder including 12 DFIGs).

points A and B.

The transformers of the wind farm are connected to a 500 kV power system at the POI. The power system is similar to the single-mode benchmark of Fig. 3.20. Disconnection of the 100 km line results in a radial connection of the wind farm and the series compensated line (line A).

3.11.3 Multi-Mode Benchmark

In this benchmark, the wind farm consists of 266 DFIGs each with a capacity of 1.667 MVA. The wind farm is connected to three power systems through 500 kV transmission lines A, B and C which are 100 km, 500 km and 700 km long, respectively.

In this configuration, lines B and C are compensated at 50% compensation level. To disconnect the transmission lines following a fault, the breakers B1, B2 and B3 are placed between the POI and the lines A, B and C, respectively. The close and remote breakers operate in 60 ms and 80 ms, respectively. This power system has several resonance modes depending on the transmission lines outages and connections which will be discussed in Chapter 4.

3.11.4 IEEE SSR First Benchmark Model

The IEEE SSR first benchmark model has been used as a simple case study in [38]. This benchmark does not include any nonlinearities and therefore, their controllers are not designed for realistic scenarios. However, the main advantage of this benchmark is its structural simplicity. A single-line diagram representing this benchmark is shown in Fig. 3.28.

Fig. 3.29 shows the GSC and RSC control loops of the IEEE benchmark. The control system of the GSC may inject some reactive power following a fault. The injected reactive power may be absorbed by the neighboring DFIGs which results in the circulation of reactive power and power quality degradation. The IEEE benchmark does not include any FRT function and wind farm controller. Tables 3.4-3.5 summarize the parameters of the wind farm, the controllers, and the power system.

Table 3.4 MPPT data of the IEEE first benchmark.

wind speed	7 m/s	8 m/s	9 m/s	10 m/s	11 m/s	12m/s
Wm	0.75	0.85	0.95	1.05	1.15	1.25
Pm	0.32	0.49	0.69	0.95	1.25	1.6
Tm= Pm/Wm	0.43	0.58	0.73	0.9	1.09	1.28

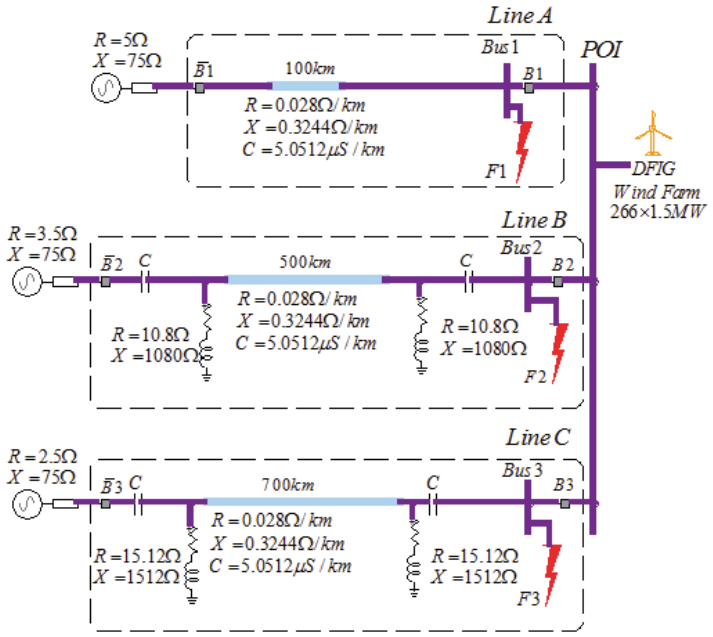

Figure 3.27 Multi-mode benchmark.

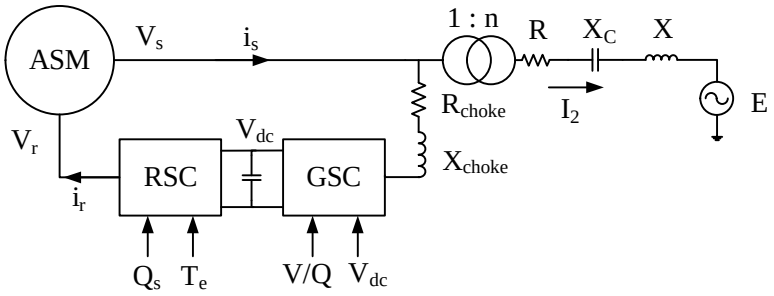

Figure 3.28 Simple IEEE first benchmark.

3.12 Summary

A state-space representation for a simplified model of the system is obtained in this chapter. The system considered is comprised of three parts: a DFIG-based wind farm, a compensated transmission line, and a power system. State-space representation for each part is obtained first. The state-space models obtained for the parts are combined to arrive at an augmented state-space model. A linearization is then performed to obtain a linear model for the whole system. The linear model obtained here is used in the next chapters to analyze and mitigate the SSCI phenomenon. Also in the present chapter, the EMT model of the system is briefly discussed, and four benchmarks are introduced to be used for the validation of the mitigation techniques presented in the next chapters.

Table 3.5 System parameters.

Rated Power	100 MW	K_{1p}	0.1
Rated Voltage	690 V	K_{1i}	4
X_{ls}	0.09231pu	K_{2p}	0
X_{lr}	0.09955pu	K_{2i}	0
X_m	3.95279	K_{3p}	0.1
R_s	0.00488 pu	K_{3i}	2
R_r	0.00549 pu	K_{4p}	0
H	3.5	K_{4i}	0
X_f	0.3 pu = 37.8 mH	K_{5p}	0.1
DC link capacitor	50*1400 uF	K_{5i}	0.05
DC link Voltage	1200 V	K_{6p}	1
Transformer ratio	690V 161KV	K_{6i}	100
Base MVA	100	K_{7p}	0.1
R_l	0.02 pu (5.1842)	K_{7i}	0.05
X_l	0.5 pu (129.605)	K_{8p}	1
X_c at 50% compensation level	64.8	K_{8i}	100
Series compensation C	40uF	Line length	154 mile

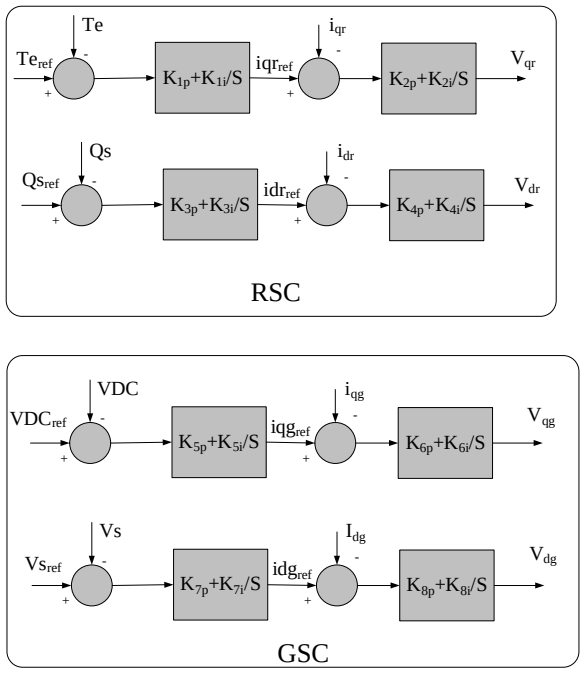

Figure 3.29 RSC and GSC controllers of the simple IEEE first benchmark.

CHAPTER 4 ANALYSIS OF SUBSYNCHRONOUS PHENOMENON

In this chapter, we first present the subsynchronous phenomenon and its various types. Then, we employ several techniques to analyze the subsynchronous control interaction (SSCI) problem using the linearized model and benchmarks introduced in Chapter. 3. The most commonly used techniques for the simulation and analysis of SSCI are:

– Frequency scan method
– Eigenvalue analysis method
– Impedance-based stability analysis technique
– Residue-based analysis method
– EMT simulation

The frequency scan method is used to identify the risk of the SSCI phenomenon. In other words, this method aims to determine whether or not a power system can undergo unstable subsynchronous oscillations. Frequency scan is the first step in the subsynchronous analysis of a power system. If an SSCI risk exists in a power system, then other techniques must be used to obtain the guidelines for the safe operating conditions of the system. Frequency scan can also be used to obtain the frequency of oscillations and approximate the system damping. The frequency scan method does not require a detailed mathematical model of the system, i.e., the EMT model of the system is sufficient. However, the frequency scan method can be time-consuming depending on the number of scenarios considered and thus it is not suitable for a sensitivity analysis. Moreover, the screening methods only obtain the resonance conditions of the system and cannot be used to draw conclusions about system behavior in the frequency or time domains.

The eigenvalue analysis provides the dampings and the frequencies of the system modes. Therefore, this method can be used to perform a sensitivity analysis and study the impacts of different power system parameters and wind farm operating conditions on the subsynchronous modes. However, the eigenvalue analysis method requires detailed modeling of the system which may result in complexity for large-scale systems. Moreover, in a realistic power system, the exact values of the system parameters may not be available and exact modeling may not be feasible.

The impedance-based stability analysis models the system in terms of impedances, and makes conclusions about its stability using the Nyquist criteria. This method is well-suited for fast and simple analysis of the subsynchronous phenomenon as it does not require a detailed modeling of the system. However, this method fails to obtain accurate results due to several

simplifications, e.g., measurement filters in the abc-frame. Moreover, this analysis becomes complicated as the size of the system increases. Therefore, the application of this method is limited.

The residue-based analysis provides the most efficient feedback signal and feedback location for the supplementary damping controller. However, this analysis technique has several disadvantages. The first drawback is that it may result in an unfeasible or unavailable set of feedback signals for the wind farm operator, e.g., parameters outside of the wind farm. The second drawback is that this method is mostly a single-input single-output (SISO) analysis and the maximum available capacity of the converters may not be utilized efficiently to damp the oscillations using the suggested feedback loops. Therefore, this method provides several weak suggestions for the power system operator.

EMT simulations use a detailed three-phase model of the system to obtain its transient behavior in the time domain. Therefore, this method can be used to verify the results obtained from the other techniques. However, as a detailed mathematical model of the system is not available in this method, it cannot be used for design purposes.

In summary, it is observed that none of these analysis techniques is individually adequate to make conclusions about system stability and behavior. An appropriate analysis technique should be selected according to the data available from the system and the objectives of the analysis. In this research, safe operating conditions for the systems under study are obtained and verified using the frequency scan, the eigenvalue analysis and EMT simulations. The residue-based analysis is performed to obtain initial suggestions for the feedback signals and feedback loops. The impedance-based stability analysis is not explained in this thesis as its application is limited in the literature. Fig. 4.1 summarizes the advantages as well as the disadvantages of each analysis technique.

The main objective of this chapter is to introduce the subsynchronous phenomenon, analyze it and propose guidelines for the safe operation of the system. The first section of this chapter briefly introduces and categorizes the subsynchronous phenomenon. Then, several techniques are introduced and performed to analyze the phenomenon. The results obtained from some of these analysis techniques are used to obtain guidelines for the safe operation of power systems and wind farms.

4.1 Different Types of Subsynchronous Phenomenon

In general, the subsynchronous phenomenon can be categorized into three types:
– Subsynchronous resonance (SSR): SSR occurs due to the interaction between turbine-

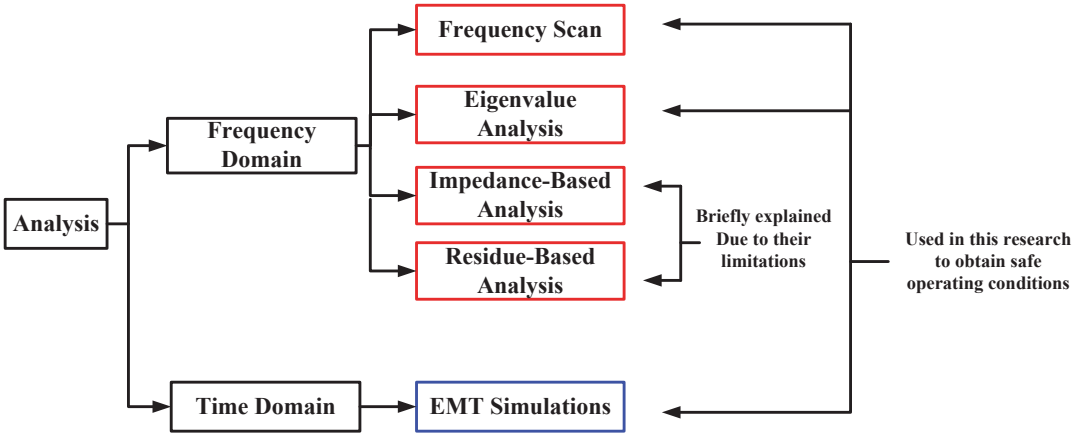

Technique	Features	Limitations
Frequency scan	- Provides the preliminary results for subsynchronous analysis - Effective in study of IGE - Effective and cost-efficient technique - Identifies possible TI and TA problems	- Limited to impedance seen from the network - Tends to be an approximate method - Only identify the risk of SSCI - Needs to be supported by time domain simulations - Time consuming technique depending on the number of scenarios and used signals
Eigenvalue analysis	- Based on mathematical model of system - Provides frequency and damping of system modes - Used for study of TI and IGE	- Requires detailed model of system which may not be available - Not suitable for TA analysis - Complexity arises as the size of system increases
Impedance-based analysis	- Save time in analysis - Frequency domain analysis - Used for IGE analysis - Provides modular approach for SSR Analysis.	- Not accurate results - Not much literature available - Complexity arises as the size of system increases - Difficulty in implementation of several functions in terms of Impedance i.e., filters in abc-frame
Residue-based analysis	- Provides the best feedback signals and feedback locations for damping controller - Frequency domain analysis	- Proposed feedback signals may not be available in wind farm structure - Proposed feedback loops may not efficiently use the capacity of converters
EMT simulations	- Time domain analysis - Can be used to show the impact of time varying parameters - Suggests the utilization of simulation software - Used for IGE, TI and TA analysis	- Cannot be used for design purposes - New system models are not available easily

Figure 4.1 Features and limitations of the existing analysis techniques.

generator and series compensated transmission line systems.

– Subsynchronous control interaction (SSCI): SSCI, also known as subsynchronous interaction (SSI), occurs when there is an interaction between the control system of power electronic devices and the series compensated transmission system.
– Subsynchronous torsional interaction (SSTI): This phenomena occurs due to the interaction between turbine-generator mechanical system and transmission-level devices (such as compensated lines and HVDC).

The SSR itself can be categorized into two phenomena with different characteristics, Fig. 4.2:

– Self-excitation
– Transient torque amplification (TA)

The self-excitation phenomenon is initially triggered by a small disturbance signal. Using the linearization approach, we can determine the possibility of occurrence of self-excitation and analyze the system behavior.

The TA phenomenon often occurs due to a large perturbation that changes the operating point of the system. The TA is a non-linear and complex phenomenon which is often analyzed by time domain simulations (e.g., EMT simulations).

Self-excitation phenomenon itself is categorized into two types:

– Induction generator effect (IGE)
– Torsional interaction (TI)

In [86, 87], it has been shown that an occurrence of the IGE results in the occurrence of the TI, and vice versa. The TI brings about a negative resistance which triggers the IGE, whereas the IGE results in a negative damping for the TI. The IGE occurs if the equivalent resistance observed from the rotor neutral point (i.e., the SSR impedance) is negative, and if a frequency exists at which the SSR reactance is almost zero. The equivalent resistance

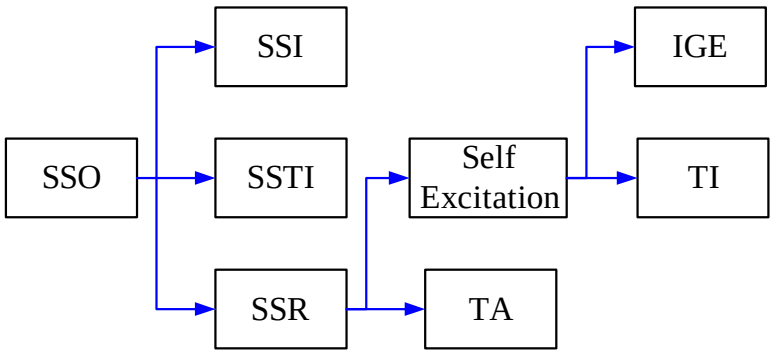

Figure 4.2 Different types of subsynchronous phenomena.

observed from the rotor neutral point is [88]:

$$R_{ef} = \frac{R_r}{s} + R_s + R_t, \tag{4.1}$$

where s is the machine slip and R_r, R_s and R_t are the rotor, stator and transmission line equivalent resistances, respectively. It should be noted that, in a DFIG-based wind farm, the resistance resulting from the operation of the RSC should also be added to the above expression, i.e.,

$$R_{ef} = Z_{RSC} + \frac{R_r}{s} + R_s + R_s \text{ and } Z_{RSC} = -\frac{V_r}{sI_r} \tag{4.2}$$

where V_r, I_r are, respectively, the steady-state rotor voltage and the rotor current. The severity of oscillations corresponds to the magnitude of the negative resistance.

Tortional interaction or TI is an unstable electromechanical condition in which the power system and the mechanical system of the DFIG exchange energy at low frequencies. More specifically, the TI occurs when the sum of the power system resonance frequency and the natural frequency of the shaft becomes equal to 60 Hz. Subsequent to a TI occurrence, the rotor oscillations induce a voltage on the stator of the generator. The induced voltage includes two components of frequencies $f_r - f_n$ and $f_r + f_n$, where f_r and f_n are the resonance and nominal frequencies of the power system, respectively. The sub-resonance frequency component $(f_r - f_n)$ may become unstable depending on the damping value of the mechanical shaft. The supersynchronous component $(f_r + f_n)$ will be always damped as demonstrated in [89]. If the torque resulting from the subsynchronous current is greater than or equal to the natural damping of the shaft, the generator becomes self-excited. Such a condition results in shaft aging or even failure.

Hydro power plants are immune to the TI phenomenon due to the higher inertia of the generator in comparison to that of the turbine [87]. The TI also has a low impact on a DFIG wind turbine where the shaft is designed to have very low natural frequencies (e.g., below 10 Hz).

The SSI, or SSCI as it is sometimes called, is the interaction between a series compensated transmission system (or an HVDC system) and the control circuit of the wind turbine generator [90]. Various faults or disturbances can trigger an unstable SSI between the power network and the current control loops of the RSC. The SSCI is a purely electrical phenomenon which results from the fast response of the RSC controller following faults and disturbances [20, 91]. In other words, due to disturbances or faults, the current control loops of the RSC change the rotor resistance so that the resistance observed from the stator side becomes negative.

The SSCI may occur if the resistance observed from the rotor neutral point becomes negative where the reactance crosses zero [20]. It should be noted that the magnitude of the equivalent resistance is a measure of damping at resonance frequency.

The SSTI is an electromechanical phenomenon where there is a huge energy exchange between the series compensated transmission system and the wind turbine's rotating masses. This phenomenon is similar to the turbine-generator shaft torsional interaction as detailed in [79].

4.2 Frequency Scan

The frequency scan analysis calculates the observed impedance from an arbitrary point of the system over the subsynchronous frequency range. This method can provide useful information about the system behavior including the resonance frequencies and their approximate damping. This method has been extensively used in the literature due to its simplicity for large-scale systems [20]. To discover the possibility of subsynchronous phenomenon, screening techniques are often combined with time domain simulations.

In frequency scan analysis, a voltage or current signal is superimposed on the system voltage or current for each single frequency. This signal should be large enough to be distinguishable from noise, and small enough not to move the operating point of the system. In this chapter, voltage has been chosen as the excitation signal. Therefore, the impedance of the system for each frequency is equal to the excitation signal divided by the measured current. The impedance of the power system regardless of its active or passive components (e.g., machines and loads with power electronic devices such as converters/inverters) can be determined using this method.

The frequency scan should be performed for both the wind turbine and the power system in order to assess the risk of the subsynchronous phenomenon. It should be noted that the measurement point for both the turbine scan and the power system scan are the LV bus of the DFIG. The procedure for computing the impedances of the turbine side and the power system side are shown in Figs. 4.4-4.3.

The following signals are usually injected to perform the frequency scan analysis:
– Sinusoidal signals
– Impulse signals
– Gaussian white noise

The frequency scan based on sinusoidal signal injection is a time-consuming process since the impedances should be measured at various frequencies, and the number of the simulations depends on the desired precision. In the impulse signal injection method, the accuracy of the

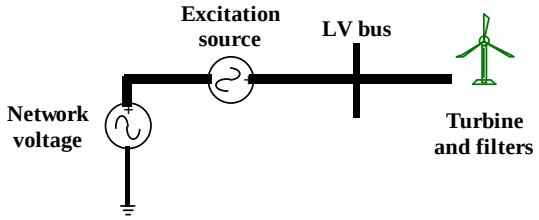

Figure 4.3 Schematic diagram demonstrating the frequency scan of a turbine.

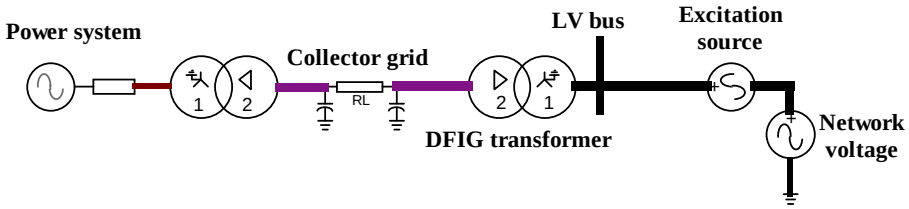

Figure 4.4 Schematic diagram demonstrating the frequency scan of a power system.

computed impedance at each frequency depends on the magnitude of the impulse at that frequency. In this method, the FFT or the DFT are required to obtain the frequency response of the system. The white noise excitation method leads to accurate results at each frequency and consequently it is an appropriate method for nonlinear systems. In this chapter, we will use the sinusoidal waveform to perform the frequency scan analysis.

Based on the results of the frequency scan method, the following criteria concerning a higher risk of SSCI have been concluded:

– Any reactance crossovers on the turbine side that coincide with the resonance conditions on the system side, even if the resistance at the subsynchronous frequency is positive.
– Any resonance conditions on the power system side if the turbine resistance at that subsynchronous frequency is negative.

The following sections show the results of the frequency scan on the system side for different benchmarks and various scenarios.

4.2.1 Frequency Scan for Single-Mode Benchmark

In this benchmark, the disconnection of Line B leaves the wind farm radially connected to the series capacitor compensated transmission line. The electrical system observed from the DFIG terminals has a reactance crossover at about 30 Hz as shown in Fig. 4.5.

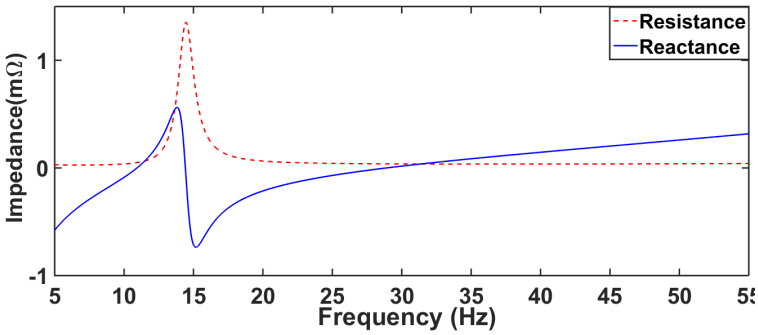

Figure 4.5 Impedance observed by the wind farm for the single-mode benchmark.

4.2.2 Frequency Scan for Multi-Mode Benchmark

The multi-mode benchmark is presented in Section. 3.11.3. In Fig. 3.27, the F1, F2 and F3 denote the metallic faults near the POI at lines A, B and C, respectively. The following scenarios are considered:

(a) A three-phase metallic fault F1 occurs at t=1 s on Bus 1 (as shown in Fig. 3.27) and, consequently, line A will be disconnected from the power system by opening breaker B1.

(b) A fault condition is imposed by applying a three-phase metallic fault F3 at t=1 s when the system consists of two compensated lines (line B and C). Under such circumstances, the breaker B3 operates and the wind farm becomes radially connected to line B.

(c) A three-phase metallic fault F2 occurs at t=1 s assuming line A is out of service. Hence, line B is disconnected due to the operation of breaker B2. The wind farm and line C will be radially connected.

The impedances observed from the DFIG terminals for the three scenarios are shown in Fig. 4.6. The reactance crossovers of the three scenarios occur at the frequencies 25 Hz, 27.5 Hz and 30 Hz, respectively. Each scenario shows different damping and thus, the system possesses different SSI modes that may be excited depending on the power system structure and contingencies.

The operating conditions of the wind farm have meaningful impacts on the system impedance. Therefore, the frequency scan of the wind turbine is performed for different wind speeds, as shown in Fig. 4.7. As expected, lower wind speeds result in lower dampings of the turbine in the subsynchronous frequency range and, consequently, in severer oscillations.

Using the method proposed in [27], we can obtain the combined impedances of the turbine and power system by adding them together, Fig. 4.8. This method provides accurate results

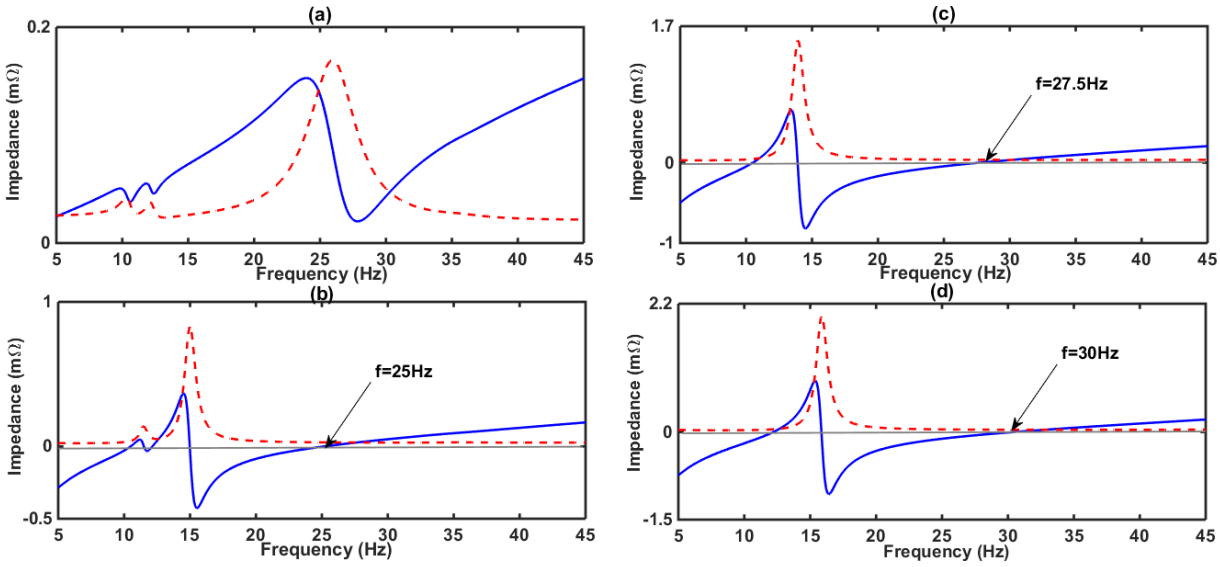

Figure 4.6 Frequency scan of (a) base case, (b) scenario a, (c) scenario b, and (d) scenario c.

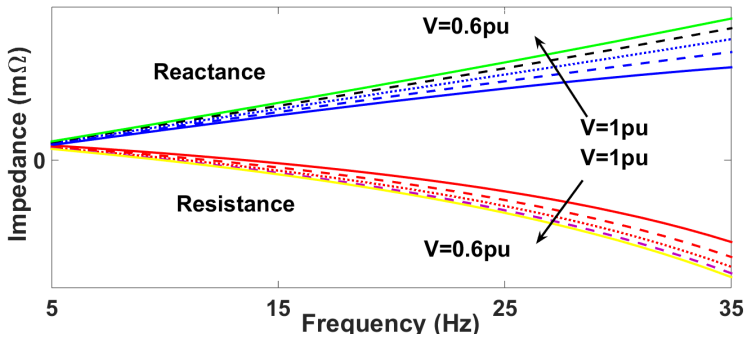

Figure 4.7 Impedance of DFIG wind turbine.

regarding the possibility of SSI as it considers both turbine and power system impedances. The results illustrate the impact of wind speed variations on the resonance frequency and the damping of the overall system. The results also emphasize the necessity of a robust controller for the SSI damping as the frequency and damping of the subsynchronous mode may vary depending on the wind farm operating conditions.

4.3 Eigenvalue Analysis

In this method, based on the linear state-space model of the system, the eigenvalues of the system, i.e., the system modes, are first computed. Then, the impact of the system parameters on the system modes are assessed. This method has been extensively used and detailed in

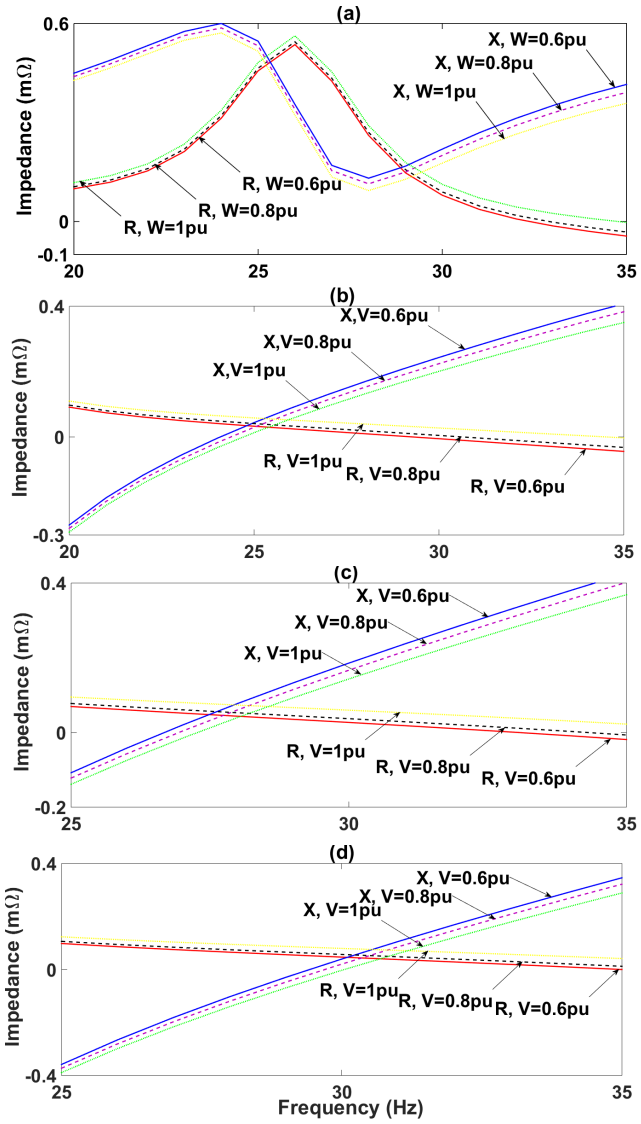

Figure 4.8 Frequency scan of (a) base case, (b) scenario a, (c) scenario b, and (d) scenario c.

the technical literatures [29, 31, 32].

4.3.1 Eigenvalue Analysis of the First IEEE Benchmark

Table 4.1 shows the eigenvalue analysis results of the first IEEE benchmark detailed in [38]. The modes of the system are distinguishable as observed from the results.

Table 4.1 Eigenvalue analysis of the IEEE first benchmark.

Mode	Eigenvalues	Frequency	Damping
Subsynchronous mode	$4.12 \pm 137.05j$	21.8Hz	-0.03
Supersynchronous mode	$-5.56 \pm 627.15j$	99.81Hz	0.0089
Electromechanical mode	$-9.31 \pm 97.33j$	15.4 Hz	0.0952
Mechanical mode	$-0.99 \pm 15.92j$	0.942Hz	0.1699

4.3.2 Eigenvalue analysis of the Single-Mode Benchmark

The eigenvalue analysis of this benchmark is shown in Figs. 4.9-4.11, where the sensitivity of the SSI mode with respect to resistance, reactance and capacitor impedance variations are shown as well. An increase in the resistance results in the reduction of resonance frequency and the enhancement of the SSI mode damping. The larger the parameter X is, the larger the damping and the frequency of oscillations will be. As expected, an increase in capacitor impedance results in a lower damping and a lower resonant frequency. The results obtained also indicate that at lower wind speeds, the SSI oscillations will be more severe.

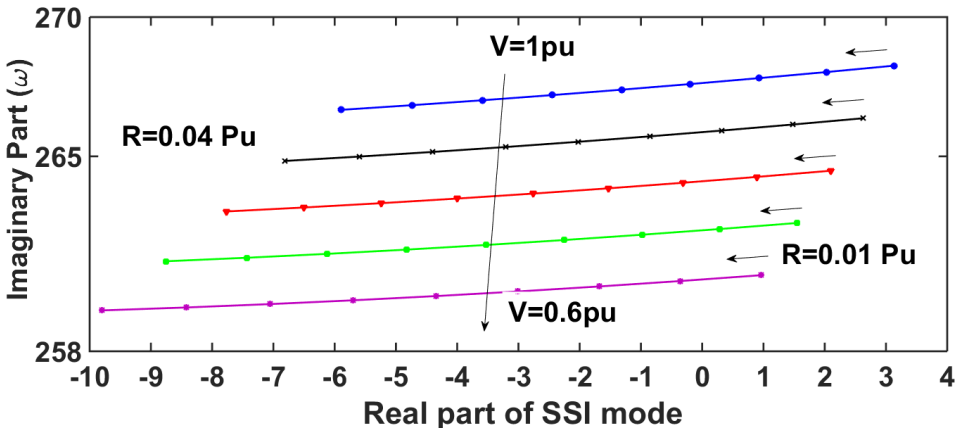

Figure 4.9 Effect of R and wind speed variations on the real part of SSI mode.

Figs. 4.12-4.17 show the impacts of the internal wind farm parameters and the operating conditions on the system stability. The impact of the RSC rise-time on the loci of the SSI mode is significant. As observed from Fig. 4.12, increasing the RSC rise-time (i.e., an inner loop controller with a slower response) will solve the SSI problem and, conversely, decreasing this rise-time will cause severer oscillations. It should be noted that reducing the rise-time of the inner loop control degrades the transient behavior of the wind turbine. As seen from Fig. 4.13, the GSC rise-time has a negligible impact on SSI oscillations. The impacts of the gain of the active power control loop K_p and the gain of the voltage regulator K_v are shown

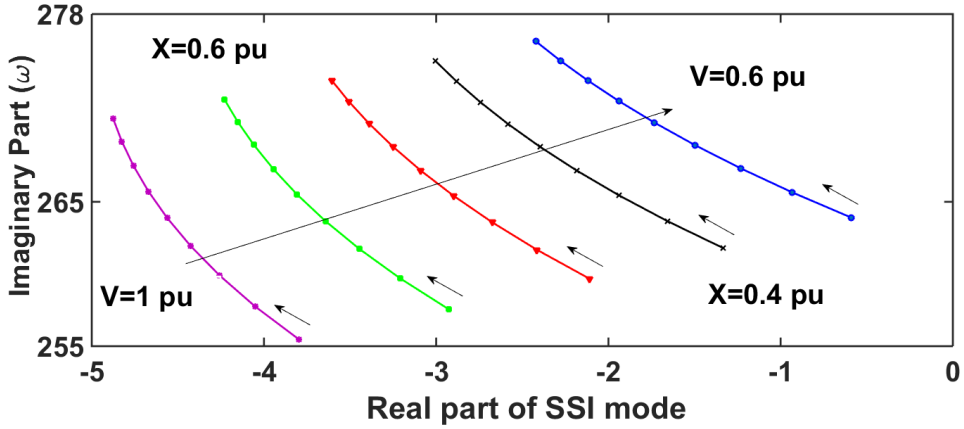

Figure 4.10 Effect of X and wind speed variations on the real part of SSI mode.

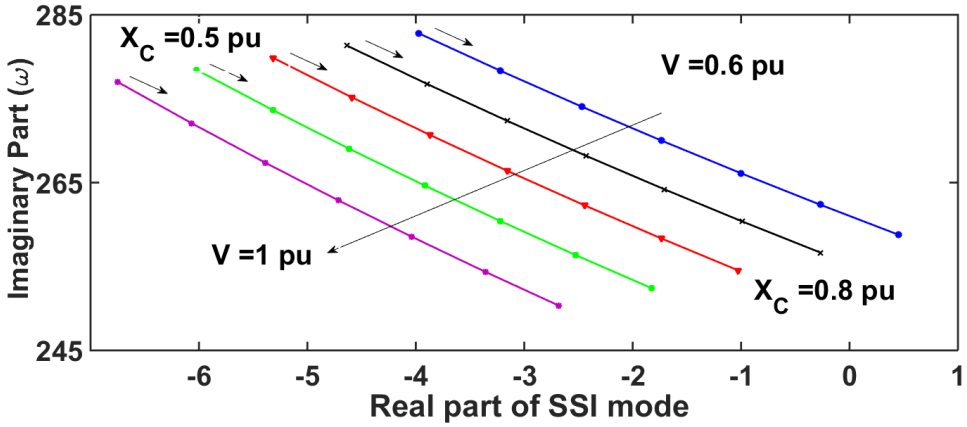

Figure 4.11 Effect of X_C and wind speed variations on the real part of SSI mode.

in Fig. 4.14 and Fig. 4.15, respectively. As observed from these figures, increasing K_p results in a system more vulnerable to SSCI oscillations, while increasing K_v results in less severe oscillations. The impacts of injected reactive power and wind turbine outages on the SSI mode are illustrated in Fig. 4.16 and Fig. 4.17, respectively. It can be observed that the injected reactive power has a negligible impact on the subsynchronous phenomenon. However, the damping is reduced as the wind speed decreases. The SSI mode damping is also smallest when there are 150 WTs in service inside the wind farm.

4.4 EMT Simulations

The EMT-type programs are able to simulate three-phase systems while considering all model details and non-linearities. The negative damping of signals can be calculated by measuring their growth rates. This method is used to verify the results obtained from the other methods.

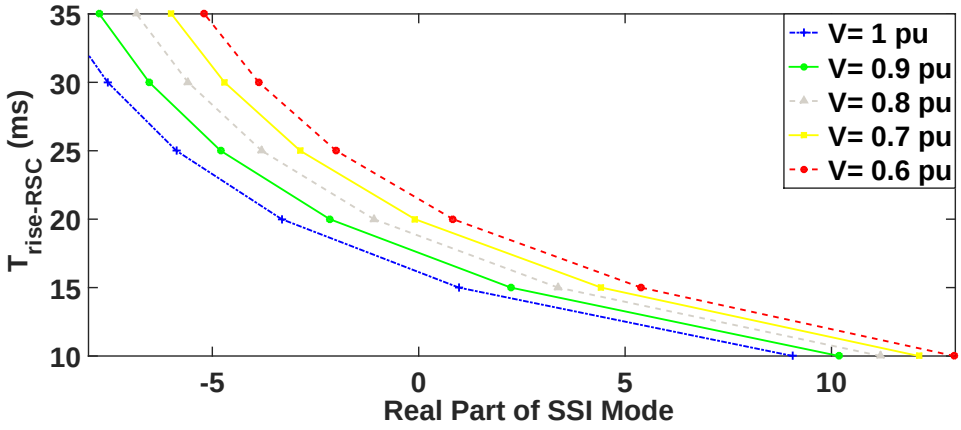

Figure 4.12 Effect of $T_{rise-RSC}$ and wind speed variations on the real part of SSI mode.

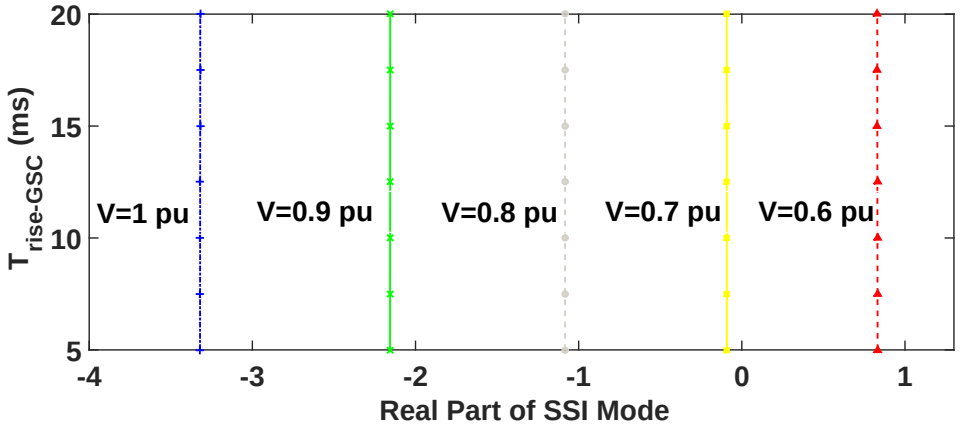

Figure 4.13 Effect of $T_{rise-GSC}$ and wind speed variations on the real part of SSI mode.

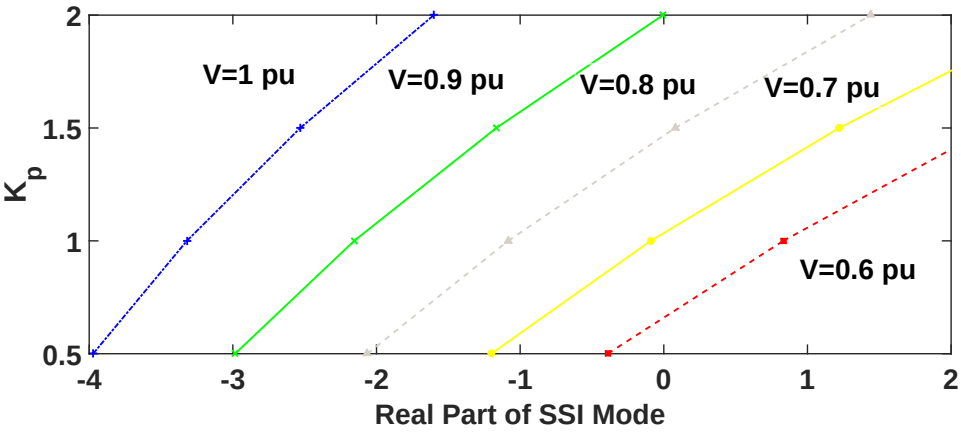

Figure 4.14 Effect of K_p and wind speed variations on the real part of SSI mode.

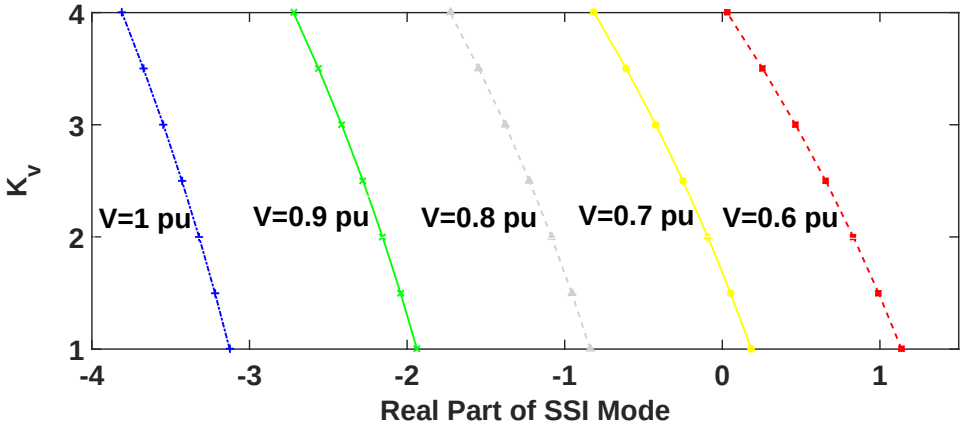

Figure 4.15 Effect of K_v and wind speed variations on the real part of SSI mode.

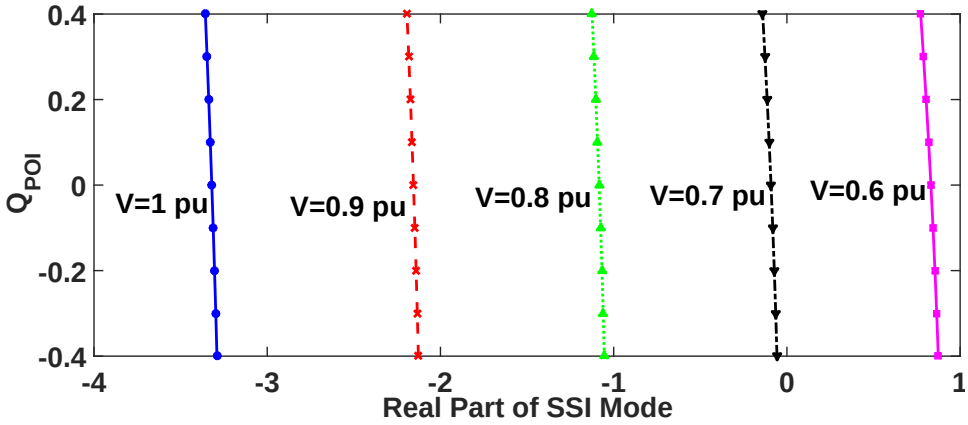

Figure 4.16 Effect of Q_{net} and wind speed variations on the real part of SSI mode.

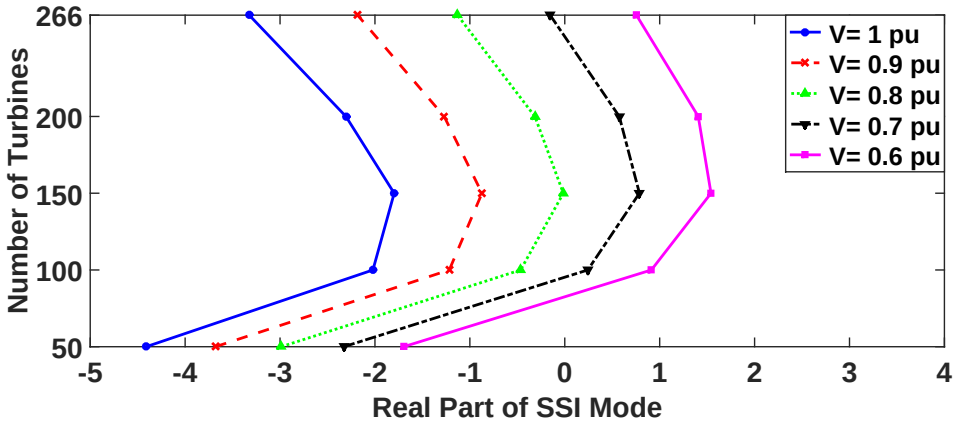

Figure 4.17 Effect of N_{gen} and wind speed variations on the real part of SSI mode.

Fig. 4.18 shows the effect of the RSC rise-time on active/reactive powers, positive-sequence voltage and DC link voltage of the DFIG-based wind turbine. The results of the analyses discussed before are verified by such EMT simulations (e.g., as the RSC rise-time increases, the system shows less severe oscillations).

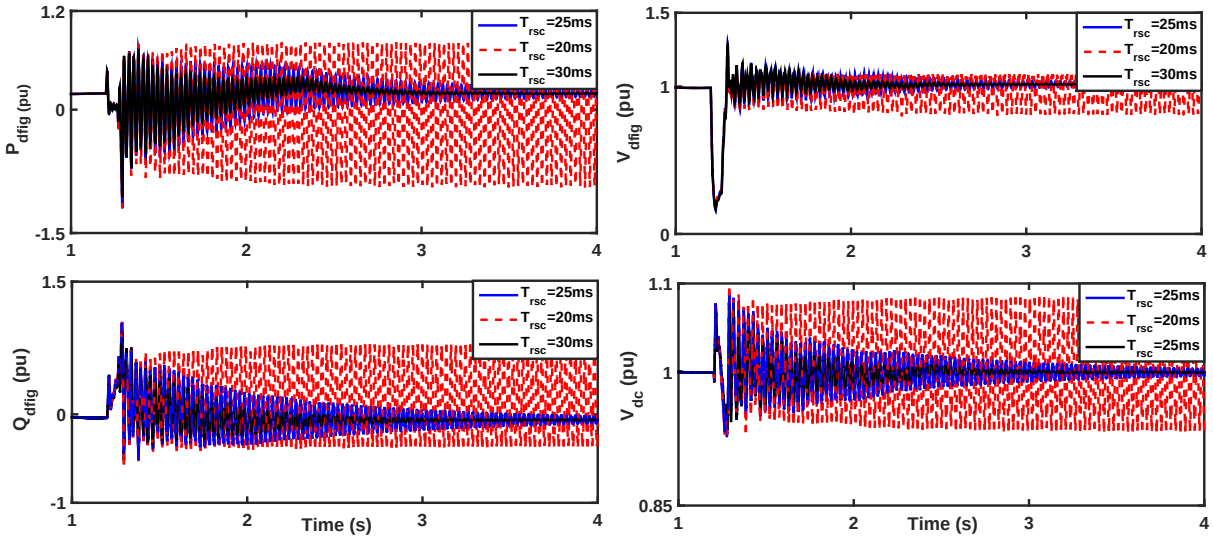

Figure 4.18 Effect of RSC rise-time on P_{dfig}, Q_{dfig}, V_{dfig} and V_{dc}.

4.5 Residue-Based Analysis Results

The residue-based analysis uses the modal information of a linear model and provides some useful suggestions about the supplementary control design [32]. The mathematical model of a linear system can be expressed as:

$$\dot{\mathbf{x}} = \mathbf{A}\mathbf{x} + \mathbf{B}\mathbf{u} \tag{4.3}$$

$$\mathbf{y} = \mathbf{C}\mathbf{x} + \mathbf{D}\mathbf{u} \tag{4.4}$$

where $\mathbf{A}$, $\mathbf{B}$, $\mathbf{C}$, and $\mathbf{D}$ are matrices of appropriate dimensions. The square matrix $\mathbf{A}$ is of order n. The matrices $\mathbf{V}$, $\mathbf{W}$, and $\mathbf{\Lambda}$ are defined as:

$$\mathbf{V} = [\mathbf{V}_1, \mathbf{V}_2, ..., \mathbf{V}_n] \tag{4.5}$$

$$\mathbf{W} = [\mathbf{W}_1^T, \mathbf{W}_2^T, ..., \mathbf{W}_n^T] \tag{4.6}$$

$$\mathbf{\Lambda} = diag(\lambda_1, \lambda_2, ..., \lambda_n) \tag{4.7}$$

where $\mathbf{V}_i$, $\mathbf{W}_i^T$, and λ_i are the normalized right eigenvectors, left eigenvectors, and eigenvalues of the matrix $\mathbf{A}$. It is assumed that matrix $\mathbf{A}$ has n independent eigenvectors [32, 92]. Applying the similarity transformation $\tilde{\mathbf{x}} = \mathbf{W}\mathbf{x}$ yields

$$\begin{aligned} \dot{\tilde{\mathbf{x}}} &= \Lambda\tilde{\mathbf{x}} + \mathbf{WBu} \\ \mathbf{y} &= \mathbf{CV}\tilde{\mathbf{x}} + \mathbf{Du} \end{aligned} \tag{4.8}$$

where $\mathbf{\Lambda} = \mathbf{WAV}$. As it is observed from (4.8), since $\mathbf{\Lambda}$ is diagonal, there is no coupling between the states $\tilde{x_i}$ $(i = 1, ..., n)$.

The participation factor shows the effect of the i^{th} state on the k^{th} eigenvalue, and is calculated as [88]:

$$P_{ki} = \frac{\mid v_{ik} \mid . \mid w_{ki} \mid}{\sum_{j=1}^{n} \mid v_{ij} \mid . \mid w_{ji} \mid} \tag{4.9}$$

The participation factor can provide valuable insight into the system behavior. The main drawback of the participation factor is that it ignores the impacts of input/output signals. In contrast, the residue-based analysis uses the state-space representation of the system and the input/output signals to obtain the optimal location and signals for applying the supplementary controller. The matrix $\mathbf{WB}$ in (4.8), also known as the modal controllability matrix, can be used to determine the most effective control loops (i.e., those stabilizing the system with less control efforts). Moreover, the matrix $\mathbf{CV}$ in (4.8), also known as the modal observability matrix, indicates the contribution of each state to the system output. This contribution helps to determine the most effective set of measured signals which can be used in the feedback loop. The residues R_i $(i = 1, ..., n)$ can be calculated from the following expansion [30, 32]:

$$G(s) = \mathbf{CV}(s\mathbf{I} - \mathbf{\Lambda})^{-1}\mathbf{WB} = \sum_{i=1}^{n} \frac{CV_iW_iB}{s - \lambda_i} = \sum_{i=1}^{n} \frac{R_i}{s - \lambda_i} \tag{4.10}$$

As the magnitude of a certain residue increases, less control gain is required to stabilize the system when the corresponding output is used as a feedback signal. On the other hand, the higher values of phase-lag of a residue create damping (stability) issues. The residue-based analysis is applied to the first IEEE benchmark [38] where the control signals of the supplementary controller are used in the RSC control loops. The results are summarized in Table 4.2.

The results of the residue-based analysis with the control signals of the supplementary controller appended to the GSC controllers are demonstrated in Table 4.3.

The results of the residue analysis conclude that:

Table 4.2 RSC residue analysis results.

Signal	Location	Controllability (||,∠)		Observability (||,∠)		Residue (||,∠)	
Line active power	T control outer loop	0.00017	0.7681	0.1647	-3.1295	3×10^{-5}	2.3856
	T control inner Loop	1.738	-0.6477	0.1635	-3.1333	0.2843	2.5023
	Q control Outer Loop	0.0017	-2.506	0.1644	-0.0215	3×10^{-4}	-2.484
	Q control iuter Loop	17.223	-2.2758	0.1632	-0.0176	2.8116	-2.258
ω_m	T control Outer Loop	0.00017	0.7681	0.0007	-1.5028	10^{-6}	-2.27
	T control inner Loop	1.738	-0.6476	0.0007	1.5059	0.0012	-2.153
	Q control Outer Loop	0.0017	-2.5060	0.0007	-1.6456	10^{-7}	-0.860
	Q control inner Loop	17.2234	-2.2758	0.0007	-1.6424	0.012	-0.633
Line current	T control Outer Loop	0.00017	-0.7681	0.2304	3.1302	0.00004	2.3840
	T control inner Loop	1.738	0.6477	0.2288	3.1339	0.3978	2.5016
	Q control Outer Loop	0.0017	-2.5059	0.2302	-0.0202	0.0004	-2.485
	Q control inner Loop	17.225	-2.2757	0.2285	-0.017	3.9352	-2.258

– The rotor speed is not an appropriate choice to use as the input of the supplementary SSI damping controller due to its low observability.
– The outer control loops (both RSC and GSC) are not suitable choices to be augmented by the supplementary SSI damping control signals due to their low controllability.
– The best location to add the supplementary control signals, and the best feedback signal to be used by the supplementary controller, respectively, are the GSC d-axis current control loop and the transmission line current, due to their high controllability and observability.

In some systems, to achieve the maximum available damping capabilities of the converters, the supplementary control signals are added to the inputs of the controllers of all inner loops. Moreover, in some cases, the measurement signals are polluted by noise, or may be inaccessible (e.g., transmission line current) thus, cannot be chosen as feedback signals. Therefore, in practice, the currents of the DFIG converters are often selected as the feedback signals when

Table 4.3 GSC residue analysis.

Signal	Location	Controllability (||,∠)		Observability (||,∠)		Residue (||,∠)	
Line active power	VDC control, inner loop	1.222	-0.2527	0.0006	-1.642	0.0007	1.389
	VDC control outer loop	0.113	-0.3653	0.0006	-1.642	0.0007	1.2771
	Second Loop	40.869	-0.3247	.0007	-1.642	0.0287	1.3204
ω_m	VDC control inner loop	1.221	-0.2527	0.2285	-0.017	0.2564	-0.235
	VDC control outer loop	-0.365	0.1130	0.2285	-0.017	0.0258	-0.348
	Second Loop	40.869	-0.3247	0.2298	-0.016	9.3929	-0.308
Line current	VDC control inner loop	1.22	-0.2527	0.1632	-0.017	0.1832	-0.235
	VDC control outer loop	0.113	-0.3653	0.1632	-0.017	0.0184	-0.347
	Second Loop	40.86	-0.3247	0.2643	-0.020	0.7139	-0.303

it comes to the design of the SSI damping supplementary controller.

4.6 Guidelines for Safe Operation of the Power System

In this section, guidelines for the safe operation of a DFIG-based wind farm which is connected to a compensated transmission line is discussed. The procedure for obtaining such guidelines is as follows:

- **Frequency Scan**: Performing the frequency scan of a power system is the first step in identifying the potential risk of SSCI. A reactance crossover indicates a resonance condition in the electrical network, i.e. a potential risk of SSCI. To perform the frequency scan, several scenarios should be considered as discussed in Section. 4.2. These simulation scenarios should consider
  - Transmission network outage scenarios
  - Different loading and generator dispatch scenarios
  - Future transmission expansion scenarios

  This study is often performed by the transmission system operator. To support the results obtained from the frequency scan method, time domain simulations should also be carried out. If the system is vulnerable to the SSCI phenomenon, the next step is to perform the eigenvalue analysis and EMT simulations to demonstrate the impact of system parameters and wind farm operating conditions on the stability and transient behavior of the system.

If the results obtained from the frequency scan and EMT simulations indicate that the system is not vulnerable to SSCI, further study is not required. All of the introduced benchmarks have potential SSCI risk considering their frequency scan results presented in Section. 4.2.

- **Eigenvalue Analysis**: To perform this analysis technique, the state-space representation of the linearized model of the system is required. The obtained results of the eigenvalue analysis are summarized as:
  - Wind speed: As the damping of the SSCI modes decrease following a decrease in the wind speed, the permissible slowest wind speed should be considered in the studies and/or simulations. It can be observed from Section. 4.3 that subsynchronous oscillations are unstable for wind speeds lower than 0.7 pu.
  - RSC current control parameters: The parameters of the RSC current controller have a significant impact on the SSCI modes. Hence, the damping of these modes can be improved (when necessary) by increasing the RSC current control rise-time. However, the transient performance of wind turbines may deteriorate following the usage of controllers with large rise-times. If very large RSC current control rise-time usage is required for the desired damping of the SSCI modes, the transient (FRT) voltage regulator gain should be increased to achieve the desired transient performance during faults or over-voltage conditions. It should be noted that in this case, the transient behavior of the system may be affected by large values of K_v. Fig. 4.12 shows that for each wind speed there is a value for the rise-time that stabilizes the system (e.g., for 0.6 pu wind speed, the rise-time should be more than 22 ms, Fig. 4.18).
  - RSC outer control parameters: The impact of the RSC outer control parameters (K_v and K_p) on the damping of the SSCI modes is high. The larger K_p is, the smaller is the system damping. By increasing the voltage regulation gain, the damping increases slightly. It should be noted that the impact of the voltage regulator gain is less noticeable for higher wind speeds as the damping of the SSCI modes becomes higher. As an example, considering 0.6 pu wind speed, K_v should be higher than 4 and K_p should be lower than 0.65 to ensure system stability, Figs 4.14-4.15.
  - GSC current control parameters: The inner loop of the GSC has a negligible impact on the damping of the SSCI modes.
  - Wind farm reactive power generation: As it can be observed from the eigenvalue analysis, the injected reactive power of the wind farm has almost no impact on the damping of the SSCI modes.
  - Wind turbine outage: The eigenvalue analysis results demonstrate that the impact of wind turbine outages on the SSCI modes is significant. SSCI modes have the lowest

damping if 150 wind turbines are in service (i.e., half the turbines available in the wind farm), Fig. 4.17. It should be noted that a large number of wind turbine outages is expected to occur due to collector grid feeder outages or low wind speeds. This will result in an increase in the equivalent collector grid impedance (both resistance and reactance). When the increase in equivalent collector grid impedance is considered in the linearized model, the corresponding damping of the SSCI modes will increase.

– Power system impedance: As demonstrated in Section. 4.3, X_C has a significant impact on the SSCI modes. When X_C increases, the wind farm becomes more vulnerable to SSCI. It should be also noted that smaller X result in a more vulnerable system as it can be considered as an increase of the effective compensation level. The small value of resistance can cause severer oscillations as it results in a decrease in the damping of the system.

Table 4.4 summarizes the obtained results.

Table 4.4 The guidelines for safe operating conditions of the system.

	Impact on SSCI	
Power system parameters	Very High	SSCI mode damping decreases with the increase in X_C
		SSCI mode damping increases with the increase in X
		SSCI mode damping increases with the increase in R
Wind speed	Very High	SSCI mode damping decreases with the decrease in wind speed
Wind turbine outages	High	SSCI mode damping decreases in extreme WT outage scenarios
Wind farm reactive power generation	Very Low	-
RSC current control parameters	VeryHigh	SSCI mode damping decrease with the decrease in RSC rise time
RSC outer control parameters	High	SSCI mode damping decreases with the decrease in voltage regulator gain
		SSCI mode damping increases with the decrease in K_p
GSC current control parameters	Very Low	-

– **EMT Simulations**: EMT simulations can be used to obtain the transient behavior of the system and to support the results obtained from other techniques. EMT simulations consider a three-phase detailed model of the system including WFC, FRT and nonlinearities.

The impact of large disturbances, unbalanced conditions, power system faults, and variations in operating conditions can be obtained using this method. The EMT simulations verify the results obtained from the eigenvalue analysis. The damping of the SSCI mode obtained through the EMT simulations is smaller than that obtained through the eigenvalue analysis. The main reason for this difference is that the effects of low-pass measuring filters and the PLL dynamics are ignored in the linearized model of the system [27].

4.7 Summary

This chapter begins by notational explanations and brief descriptions of different types of the subsynchronous phenomenon. Then, the frequency scan method is discussed and applied to single-mode and multi-mode benchmarks in order to identify the risk of the SSCI occurrence. An eigenvalue analysis is applied to assess the impacts of system parameters and wind farm operating conditions on the damping of the SSCI modes. A residue-based analysis is done to provide suggestions about appropriate feedback signals and control loops with which to augment the SSCI damping controller for the IEEE SSR first benchmark model. The chapter concludes by using results from the frequency-scan method, eigenvalue analysis, and EMT simulations to arrive at guidelines for the safe operating conditions of power systems and wind farms amenable to SSCI.

CHAPTER 5 MITIGATION OF SUBSYNCHRONOUS OSCILLATIONS: SUPPLEMENTARY CONTROL DESIGN, EFFECT OF DELAY, SENSOR FAILURE

The control parameters of a DFIG, particularly those of the RSC current controllers, can significantly affect the system response during an SSCI event. SSCI oscillations can be mitigated by shaping a relatively slow RSC controller, i.e., by increasing the rise-time of the RSC response. However, slow controllers will result in sluggish transient behavior of the system following the faults. Moreover, the wind farm may not be able to fulfill the grid code requirements regarding the FRT. Therefore, a supplementary controller is required to damp the SSCI oscillations and ensure acceptable transient behavior.

In this chapter, LQR, mixed sensitivity H^∞ and μ-synthesis techniques are utilized to design the SSCI damping controller. Each of these techniques can be used to stabilize the system depending on the control objectives and power system topology. It should be noted that there is always a dilemma in the design procedure of the SSCI damping controller for a practical case. The more complex the control strategy is, the more control objectives can be included in the design procedure. However, using complex control schemes may require detailed mathematical model of the system or a certain level of control theory expertise. Moreover, complex control methods often result in high order controllers which are not desirable due to difficulties in implementation and noise sensitivity. In this thesis, we employ different techniques to design the SSCI damping controller for the aggregated single-mode, the detailed single-mode and the multi-mode benchmarks.

The LQR technique provides a simple and efficient SSCI damping controller which is desirable for the industry. This technique results in a closed-loop system whose order is the same as that of the plant, achieves infinite gain margin and guarantees a phase margin of more than 60 degrees [93]. However, this technique often requires an observer, which results in implementation challenges in a wind farm. Some of these implementation challenges are addressed in Section. 5.1.3. Moreover, there is no straightforward guideline for the selection of the matrices used to calculate the controller gains. Therefore, repetitive time domain simulations are required to obtain the best available damping for the SSCI modes and avoid converter saturation. The LQR technique cannot be used to achieve several control objectives, e.g., disturbance rejection and noise attenuation. Moreover, this technique cannot guarantee stability in the presence of parametric uncertainty. Therefore, it cannot stabilize the subsynchronous oscillations for certain power system topologies, e.g., the multi-mode benchmark.

The mixed-sensitivity H^∞ method results in a more complex control structure in which several control objectives such as disturbance rejection, noise attenuation and minimizing the control effort can be achieved together. In this technique, the calculation of the controller parameters can be easily translated into a set of LMIs and mixed with other control objectives, e.g., pole placement. However, use of this technique requires a certain level of control expertise which may not be available in the power system industries. This technique also results in high order controllers (the order of the obtained controller is sum of the system order and the filter order) which are noise sensitive. Moreover, to apply this technique, an accurate mathematical model of the system is required.

The last method used in this research is the μ-synthesis technique. This method is well-suited for power systems with a high level of uncertainties, e.g., frequent line outages and changes in loading patterns. The main advantage of this technique is its ability to stabilize the wind farm considering the uncertain power system parameters. However, this type of controller cannot be designed for arbitrary parameter ranges of the power system. Similar to mixed-sensitivity H^∞, the μ-synthesis technique results in high order controllers (often higher than that of the mixed-sensitivity H^∞ approach).

The detailed single-mode benchmark (detailed in Section. 3.11.1) is similar to the aggregated single-mode benchmark (detailed in Section. 3.11.2) except for the modeling of the MV feeders, the distribution of wind speed among the turbines and the number of the DFIGs modeled. The detailed single-mode benchmark is introduced to demonstrate different implementations of the SSCI damping controller and to observe the impact of wind turbine aggregation on the transient behavior of the system. Therefore, both the LQR and the mixed-sensitivity H^∞ controllers are able to alleviate the SSCI phenomenon in these power systems.

The subsynchronous oscillations in the multi-mode benchmark cannot be damped using the LQR and the mixed-sensitivity H^∞ controllers due to the multitude of the SSCI modes with different dampings and frequencies. The μ-synthesis technique is used to stabilize the system in this benchmark.

The performances of the designed controllers are evaluated using EMT simulations of the benchmarks introduced in Chapter. 3. The results obtained support the effectiveness of the proposed supplementary controllers in damping the SSCI oscillations, and in providing the excellent transient behavior of the closed-loop system regarding the FRT capabilities.

The proposed SSCI damping controllers receive the currents of the RSC and the GSC as inputs, and produce control signals which are added to the inner current control loops of the converters. The supplementary signals are dynamically limited by considering the available capacities of the RSC and the GSC to maintain them in linear operation, and to achieve the

desired transient response against the faults.

The subsynchronous damping controller can be implemented at the primary control level (wind turbine control) or at the secondary control level (WFC). In this chapter, the impact of these implementation schemes on the transient behavior of the system is investigated using the single-mode detailed benchmark whose oscillations are damped by the LQR controller. Then, an adaptive local implementation scheme is proposed to achieve better transient response and to obviate the need for high rate data transfer between the turbines and the designed damping controller.

The implementation of the SSCI damping controller at the secondary control level results in the vulnerability of the wind farm to delays. Therefore, the time-delay analysis is inevitable in order to decide on the stability of such systems. In this chapter, a delay analysis of the multi-mode benchmark, which is stabilized using the μ-synthesis technique, is performed and the delay margin is calculated by employing the Rekasius substitution technique. Since this technique results in complexities for high order systems, the Guardian Map Theory is combined with the Rekasius substitution technique to obtain the delay margin of the system. Moreover, we investigate the impact of power system parameters and wind farm operating conditions on the delay margin using sensitivity analysis. The obtained results can help wind farm operators to assess the SSCI instability risk even when an SSCI damping controller is employed. The obtained delay margin may not be sufficient depending on the technology used in the communication links and the system parameters. Therefore, a Smith predictor scheme is employed to extend the obtained delay margin.

The good performance and stability of a control system can be lost due to sensor failure. Similarly, the designed SSCI damping controller may not be able to damp the oscillations if the measurement sensors are faulty. In this chapter, a framework is proposed to detect the sensor failures in a power system and distinguish them from electrical faults as they both result in an abrupt change in the measurement signals. The proposed framework benefits from the robust residue generation technique to detect failures and to switch the controller in a gain scheduling scheme. This framework ensures the stable operation of a system which is subjected to the SSCI phenomenon following sensor failure.

5.1 Optimal LQR

The linear-quadratic regulator (LQR) method [93] has been widely used to control the power system apparatus due to its simplicity and robustness [94, 95]. This section proposes an LQR controller to damp the SSCI oscillations in a series compensated DFIG-based wind farm. The

proposed controller includes a full-state observer which estimates the state variables, and an LQR-based state feedback controller to damp the SSCI oscillations. To design the LQR controller, a reduced order model of the linearized system (presented in Chapter. 3) which includes 22 state variables is employed. This model is obtained by ignoring the dynamics that have a low impact on the SSCI modes. Two observers are designed using the Lyapunov equation and LQR technique. Then, the performance of the designed controllers in terms of damping and transient behavior are compared. It should be noted that EMT simulation of the single-mode aggregated benchmark (Section. 3.11.1) is used to demonstrate the effectiveness of the designed controller.

The LQR technique determines the optimal state feedback gain for the LTI system:

$$\begin{aligned} \dot{\mathbf{x}} &= \mathbf{A}\mathbf{x} + \mathbf{B}\mathbf{u} \\ \mathbf{y} &= \mathbf{C}\mathbf{x} + \mathbf{D}\mathbf{u} \end{aligned} \tag{5.1}$$

with the quadratic cost function as below:

$$J_{LQR} = \int_0^\infty (\mathbf{x}^T\mathbf{Q}\mathbf{x} + \mathbf{u}^T\mathbf{R}\mathbf{u})dt \tag{5.2}$$

where $\mathbf{x}$, $\mathbf{u}$ and $\mathbf{y}$ are the vectors of states, control inputs and system outputs, respectively. The matrices $\mathbf{A}$, $\mathbf{B}$, $\mathbf{C}$ and $\mathbf{D}$ are obtained from the linearization process and describe the small signal behavior of the system. The positive-definite matrix $\mathbf{R}$ is associated with the input cost, and the positive-semidefinite matrix $\mathbf{Q}$ is associated with the state cost. The equation (5.2) demonstrates a trade-off between the energy of control signals and state variations.

The optimal and stabilizing state-feedback controller which minimizes the cost J_{LQR} , i.e., $\mathbf{u} = -\mathbf{K}\mathbf{x}$, is obtained as [93]:

$$\mathbf{K} = \mathbf{R}^{-1}\mathbf{B}^T\mathbf{P} \tag{5.3}$$

where $\mathbf{P}$ is the solution for the following Riccati equation:

$$\mathbf{P}\mathbf{A} + \mathbf{A}^T\mathbf{P} - \mathbf{P}\mathbf{B}\mathbf{R}^{-1}\mathbf{B}^T\mathbf{P} + \mathbf{Q} = 0 \tag{5.4}$$

To obtain a unique solution for the matrix $\mathbf{P}$, the pair ($\mathbf{A}$,$\mathbf{B}$) is assumed to be controllable. Moreover, the pair ($\mathbf{A}$,$\mathbf{Q}$) needs to be observable.

In our design, we set $\mathbf{Q} = \mathbf{C}^T\mathbf{C}$, and $\mathbf{R}$ is chosen so that excellent transient behavior is obtained from the time-domain simulations, particularly during large disturbances. This step requires performing several EMT simulations and updating the initial value of $\mathbf{R}$ accordingly.

It should be noted that large control effort will result in converter saturation. Moreover, matrix $\mathbf{R}$ should be selected such that the maximum available capacity of converters is used to damp the oscillations. Initially, we set $\mathbf{R} = \mathbf{I}$ and check the EMT simulations for system stability and converter saturations considering the designed controller and a metallic three-phase fault at POI. To achieve better damping, we increase $\mathbf{R}$ until the maximum available capacity of the converter is used. Using this iterative approach one can obtain $\mathbf{R} = 5\mathbf{I}_{4\times4}$ assuming fixed $\mathbf{Q} = \mathbf{C}^T\mathbf{C}$.

In practice, the access or measurement of all states are not possible. Hence, full-state feedback implementation requires an observer as shown in Fig. 5.1. We use a hat sign to refer to the estimated signals.

The dynamics of full-order Luenberger observer can be expressed as:

$$\dot{\hat{\mathbf{x}}} = \mathbf{A}\hat{\mathbf{x}} + \mathbf{B}\mathbf{u} + \mathbf{L}(\mathbf{y} - \hat{\mathbf{y}}) \tag{5.5}$$

where $\mathbf{L}$ is the observer gain. By defining $\mathbf{e} = \mathbf{x} - \hat{\mathbf{x}}$ as the estimation error, and by substituting (5.1) and (5.5) into it, we can obtain the error dynamic as:

$$\dot{\mathbf{e}} = (\mathbf{A} - \mathbf{L}\mathbf{C})\mathbf{e} \tag{5.6}$$

Based on (5.6), the estimation error $\mathbf{e}$ will asymptotically converge to zero if the observer gain $\mathbf{L}$ is selected such that the matrix $\mathbf{A} - \mathbf{L}\mathbf{C}$ is Hurwitz. According to the separation theorem [93], the design of the observer and LQR gains can be performed separately.

In this section, we use both the LQR and Lyapunov techniques to determine the observer gain.

5.1.1 LQR-Based Observer Design

Since the eigenvalues of $(\mathbf{A} - \mathbf{L}\mathbf{C})$ are equal to those of $(\mathbf{A}^T - \mathbf{C}^T\mathbf{L}^T)$, the observer gain can be obtained from the following Riccati equation:

$$\mathbf{L} = \mathbf{P}_0\mathbf{C}^T{\mathbf{R}_\mathbf{0}}^{-1} \tag{5.7}$$

$$\mathbf{P}_0\mathbf{A}^T + \mathbf{A}\mathbf{P}_0 - \mathbf{P}_0\mathbf{C}^T{\mathbf{R}_\mathbf{0}}^{-1}\mathbf{C}\mathbf{P}_0 + \mathbf{Q}_0 = 0 \tag{5.8}$$

where $\mathbf{P}_0$, $\mathbf{R}_0$, and $\mathbf{Q}_0$ are the solution of Riccati equation, the input and the state weight matrices corresponding to the observer, respectively.

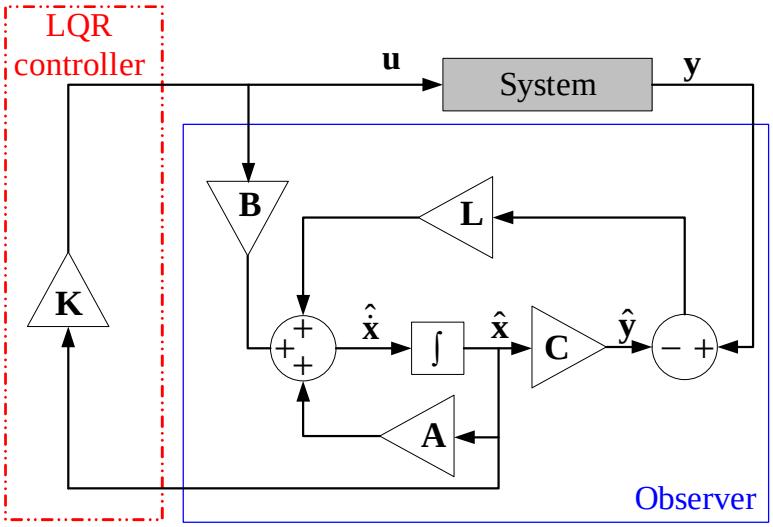

Figure 5.1 State feedback control with a Luenberger full-state observer.

5.1.2 Lyapunov-Based Observer Design

The other technique used for the observer design is the pole placement of $\mathbf{A}-\mathbf{LC}$ eigenvalues. This technique enables the designer to adjust the fastness of the error dynamic $(\mathbf{A}-\mathbf{LC})$ by moving its eigenvalues far to the left half plane. However, a very fast observer will result in a control system which is sensitive to measurement noise. It should be noted that subsynchronous modes of the $\mathbf{A}-\mathbf{LC}$ move horizontally in the s-plane as their frequency is imposed by the power system. The corresponding observer gain matrix $(\mathbf{L})$ is designed based on the method discussed in [96] as:

$$\mathbf{L} = (\mathbf{W}\mathbf{P}_{LYP}^{-1})^T \tag{5.9}$$

where

$$\begin{gathered}\mathbf{A}^T\mathbf{P}_{LYP} + \mathbf{P}_{LYP}\mathbf{A} - \mathbf{C}^T\mathbf{W} - \mathbf{W}^T\mathbf{C} + 2\alpha\mathbf{P}_{LYP} < 0 \\ \mathbf{P}_{LYP} > 0\end{gathered} \tag{5.10}$$

where $\mathbf{P}_{LYP}$ and $\mathbf{W}$ are solutions of inequalities (5.10), and α is a measure for the fastness of the controller, as shown in Fig. 5.2. The MATLAB LMI toolbox is used to calculate the matrices $\mathbf{P}_{LYP}$ and $\mathbf{W}$ and, consequently, observer gain matrix $\mathbf{L}$.

The SSCI damping controller is designed considering the radially compensated DFIG-based wind farm and its linearized equations obtained in Chapter. 3. However, the described observers are used to provide the estimated value of the state vector for the designed LQR controller to damp the subsynchronous oscillations considering $\alpha = -30$, $\mathbf{R} = \mathbf{I}_{4\times4}$ and $\mathbf{Q} = 30\mathbf{I}_{22\times22}$. These values are obtained to achieve the best possible transient response and fast observer in EMT simulations of the single-mode aggregated benchmark.

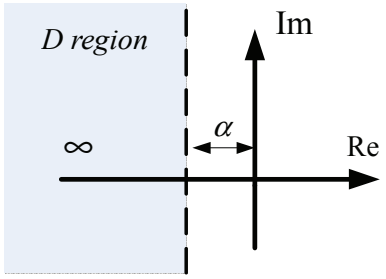

Figure 5.2 Observer pole placement region.

Similar to WFC, the supplementary SSCI damping controller is located at the wind farm secondary control level. The proposed observer uses the DFIG converter currents (i.e. $\mathbf{y} = [i_{qr}, i_{dr}, i_{qg}, i_{dg}]^T$) as input. These feedback signals eliminate the necessity for new measurements as they have already been used in the control scheme. Moreover, such signals are less noise sensitive.

The SSCI damping controller is designed for the slowest permissible wind speed (i.e., 0.6 pu) and when no wind turbine outage exists. The performance of the proposed SSCI damping controller is evaluated by EMT simulations using EMTP-RV software [82] for several scenarios. In all scenarios listed below, the wind speed is set to 0.6 pu and the wind farm operates with the unity power-factor (i.e., $Q_{POI} = 0$).

Scenarios:

– S1: A three-phase metallic fault is applied to BUS1 (end of Line B) at t=1 s (electrically close fault). The fault is cleared with the operation of circuit breakers B1 and B2.
– S2: An electrically distant fault condition is imposed to the system by applying a three-phase fault at BUS2 with an impedance of 0.3162 ($\frac{X}{R} = 3$) at t=1 s and is removed at t =1.3 s. The long fault clearing time (0.3 s) imitates delayed operation of the relays due to either breaker failure or disoperation of the protection system.
– S3: The distant fault in scenario S2 is applied at t=4 s following the close fault occurred in scenario S1.

In scenarios S1 and S2, all wind turbines are in service, whereas in scenario S3, only 150 of them are operating. We have repeated scenario S2 for a wide range of fault impedances resulting in 0.5 pu to 0.8 pu voltage sag at the DFIG terminals. The performance of the SSCI damping controller is similar for all other fault impedance cases.

To achieve the desired transient response, the SSCI damping controller output is blocked when the FRT function of DFIG is activated as detailed in [44]. However, blocking the SSCI damping controller during a fault may significantly deteriorate the performance of the damping

controller, particularly when the faulted system has an undamped SSCI mode. Therefore, blocking (or restricting) of the supplementary controller outputs is examined considering extreme fault scenarios.

The waveforms of Fig. 5.3 demonstrate the effectiveness of the proposed SSCI damping controller for scenarios S1-S2. It can be observed that the system is unstable in both S1 and S2 after the disconnection of Line B following the fault. However, the proposed damping controller damps the oscillations in both scenarios. Moreover, the damping controller exhibits similar performance with both Lyapunov and LQR based observers. In scenario S2, the SSCI mode has negative damping during the fault even when the proposed SSCI damping controller is in service, Fig. 5.3. However, the system will be stabilized by the damping controller following fault removal. The results also show that the performance of the Lyapunov based observer is slightly better than that of the LQR one.

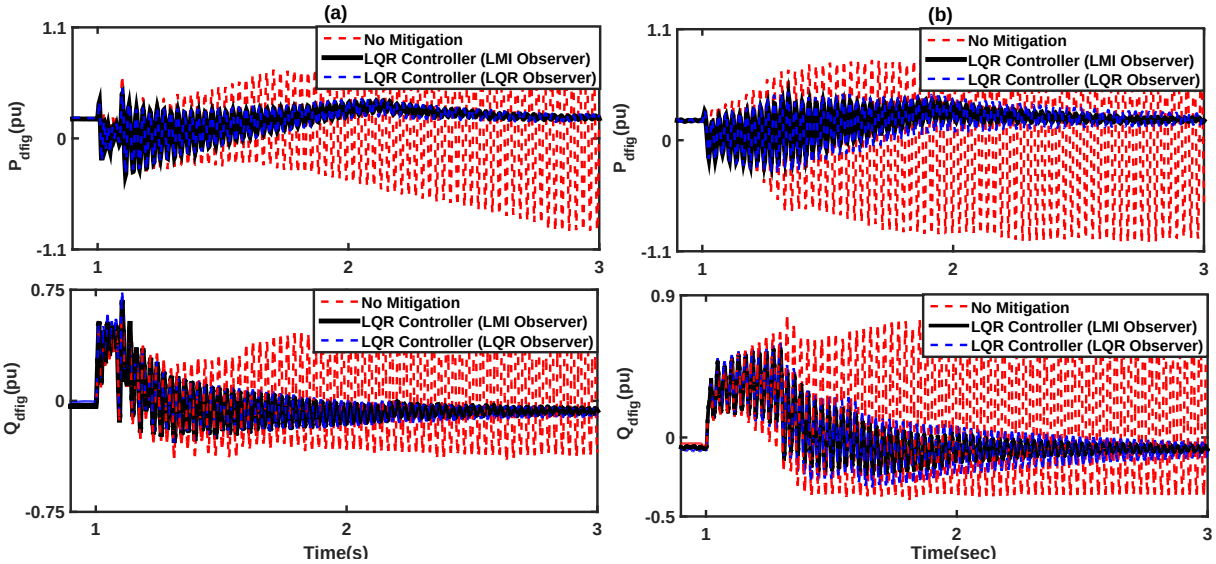

Figure 5.3 DFIG power components following the fault in (a) scenario S1, and (b) scenario S2.

Fig. 5.4 shows that when the limiters installed at the output of the damping controller adjust their limits dynamically, better performance is observed compared to the proposed method of [44] for scenarios S1 and S2. The active/reactive power components of DFIG are shown in this figure. In scenario S2, undesirable behavior is due to large oscillations in the DFIG terminal voltage resulting from the active FRT operation mode, Fig. 5.4. As a result, the SSCI mode will not be damped considering the restriction method proposed in [44].

Scenario S3 examines the severest case, in which only 150 wind turbines are in service,

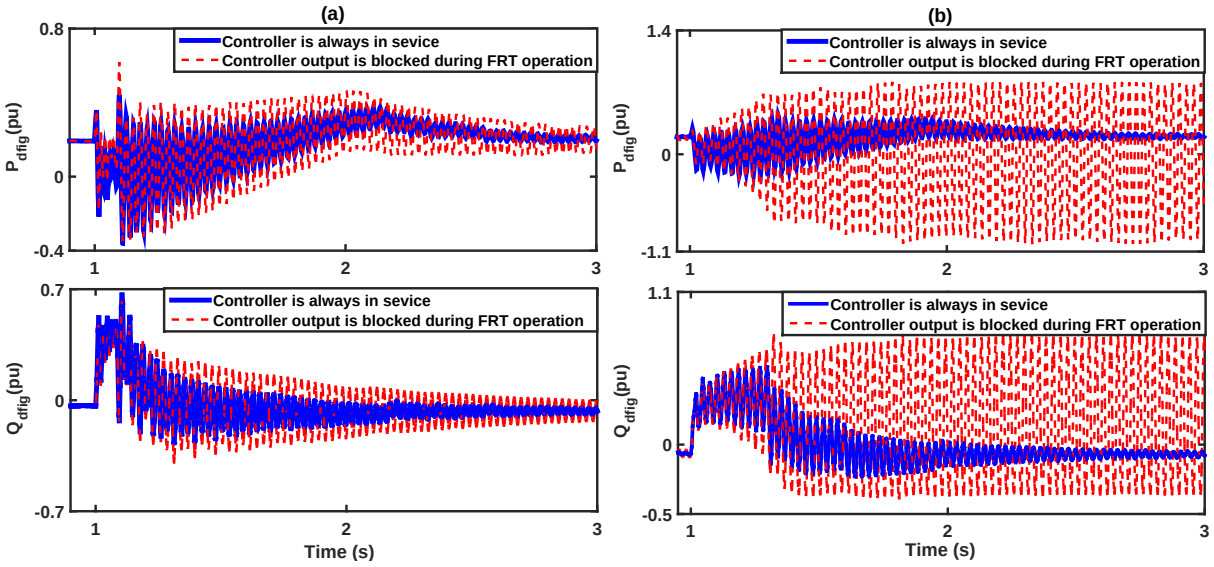

Figure 5.4 DFIG power components for different controller restriction schemes (a) scenario S1, and (b) scenario S2.

Fig. 4.17. In this scenario, the system response to both types of considered faults (close and distant faults) is demonstrated, Fig. 5.5. This figure shows that the proposed damping controller mitigates the SSCI oscillations whose frequency is similar to that obtained by the frequency scan method and eigenvalue analysis. The Lyapunov-based observer is only simulated due to its superiority compared to the LQR based one.

5.1.3 Local Implementation

The SSCI damping controllers are typically designed and tested using an aggregated wind turbine model that represents the entire wind farm. No research has been reported on the implementation in a realistic wind farm. This section first presents various implementation schemes for an LQR-based SSCI damping controller and discusses their practical implementation challenges. Then, an implementation scheme which obviates the need for high rate data transfer between the wind turbines and the wind farm secondary control layer is proposed. In the proposed implementation, the SSCI damping controller receives only the wind turbine outage information updates from WFC, and hence is not vulnerable to the variable communication network latency. The SSCI damping controller parameters are also modified when there is a change in wind turbine outage information for the ultimate performance. The effectiveness of the proposed implementation scheme is shown with EMT simulations of the detailed benchmark considering different wind speeds at each wind turbine and outages due

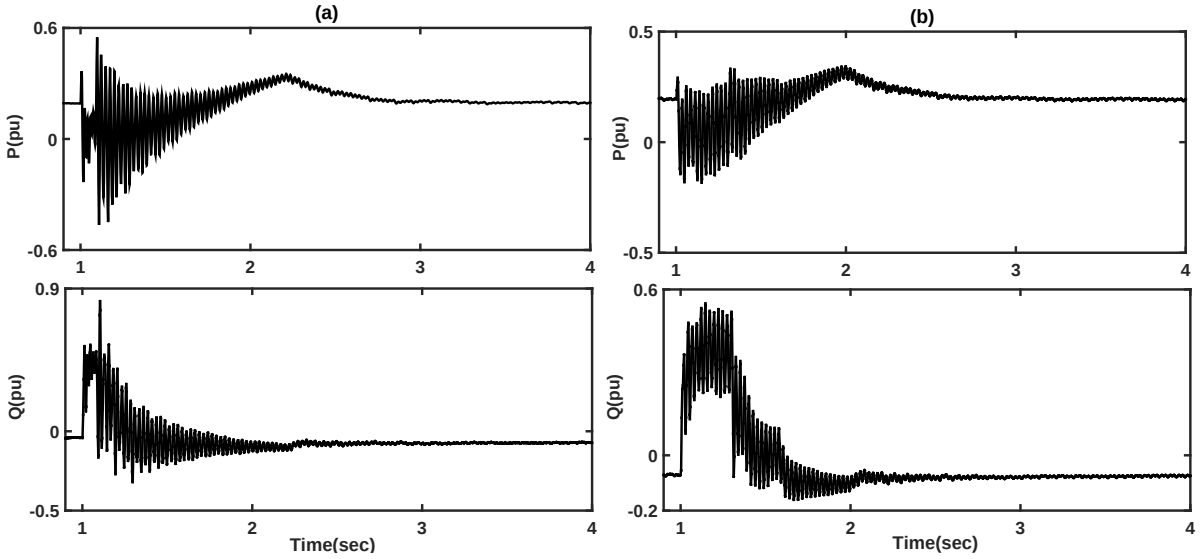

Figure 5.5 DFIG power components in scenario S3 (a) electrically close fault, and (b) electrically remote fault.

to sudden decreases in wind speeds.

The SSCI damping controller is normally expected to be located in the secondary control layer of the wind farm as it is designed based on the aggregated wind turbine model. In other words, the entire wind farm is represented by a single wind turbine although the WFC is taken into account during the SSCI damping controller design. In this implementation, each wind turbine controller sends the measurements of the current of the DFIG converter to the central SSCI damping controller (α in Fig. 5.6), and receives the output signal of the central SSCI damping controller (β in Fig. 5.6). This implementation requires communication links that enables high rate data transfer between the wind turbines and the central SSCI damping controller. The SSCI damping controller (i.e. LQR gain and observer) in the previous section is designed considering no wind turbine outages in the wind farm and the slowest permissible wind speed. On the other hand, its effectiveness is tested for various wind speeds as well as wind turbine outage scenarios.

Fig. 5.7 shows the proposed local SSCI damping controller integrated into the DFIG control. This implementation will not function properly when there are significant wind turbine outages in the wind farm. On the other hand, the wind conditions and reactive power generation at each wind turbine are expected to be similar. Hence, proper functioning of the SSCI damping controller can be achieved by scaling the measured DFIG converter currents considering the number of units in service (N in Fig. 5.7). It should be emphasized here that, the ag-

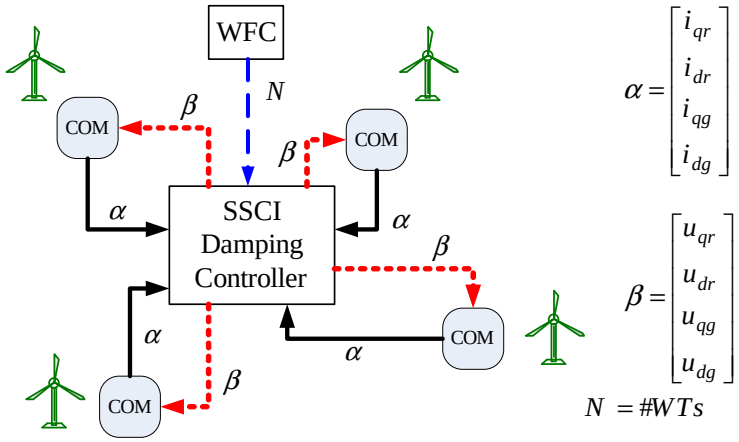

Figure 5.6 Central implementation of the SSCI damping controller.

gregated model used for the SSCI damping controller design also assumes the same wind conditions and reactive power generation at each wind turbine. The information N is available at WFC and can be transmitted to wind turbine controllers with the voltage reference generated by the WFC ($\Delta V_{dfig}^{'}$ in Fig. 3.11). The signal N only changes whenever there is a change in the number of wind turbines in service (i.e. no continuous change). Hence, the high rate data transfer between the wind turbine controllers and the WFC is not required. It should be noted that, sudden and large changes in N can be expected following a fault inside the WF or following a sudden drop in the wind speed that results in partial tripping in the wind farm due to the different wind conditions at each turbine. To improve the SSCI damping controller performance, we propose an adaptive approach that modifies the controller considering the number of units in service. In this approach, a separate SSCI damping controller (i.e. LQR gain and observer) is designed for each wind turbine outage scenario, and the selection is made with the signal N (i.e. the number of turbines in service) as illustrated in Fig. 5.8. It should be noted that the same adaptive approach can also be used in the central SSCI damping controller as the number of wind turbines in service is known at the secondary control level.

The detailed model of the single-mode detailed benchmark (introduced in Chapter 3) is considered as the test system. The DFIG converters are represented by average value models (AVMs). The simulation time step is 50 us. A three-phase metallic fault is applied at the wind park end of Line-2 at t=1.2 s and cleared with the operation of circuit breakers B1 and B2, Fig. 3.21. The operating times of B1 and B2 are 80 and 60 ms, respectively. The simulation scenarios are presented in Table 5.1. In this table, $\sigma(\eta, \beta)$ represent the Gaussian distribution with a mean value and standard deviation of η and β, respectively.

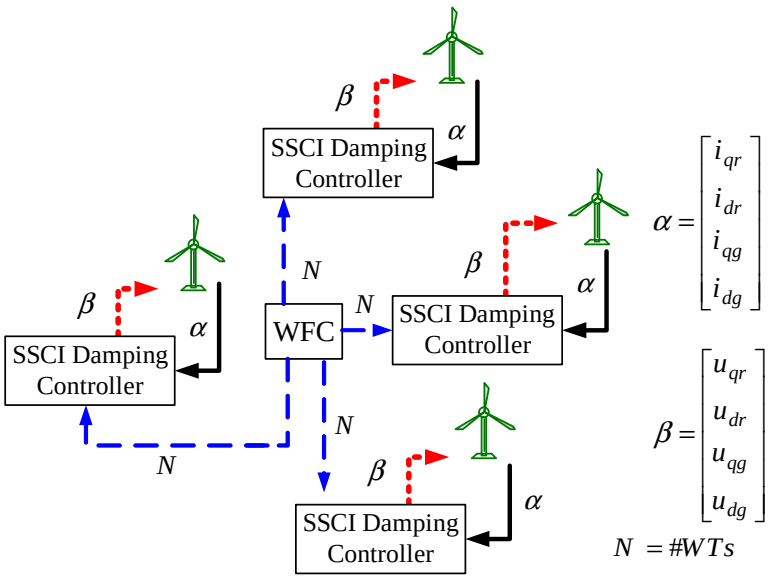

Figure 5.7 Local implementation of the SSCI damping controller.

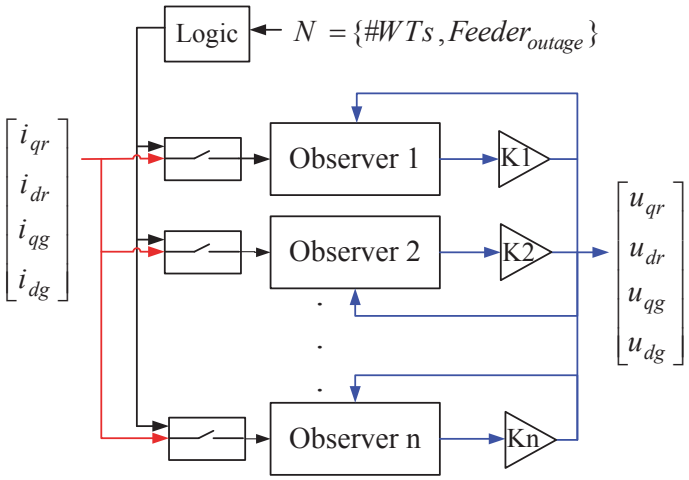

Figure 5.8 Control scheme of the local implementation of the SSCI damping controller.

The active/reactive power components of the DFIG for the scenarios S1-S4 are shown in Fig. 5.9. The system becomes unstable in S1 following the fault removal. On the other hand, the system becomes stable with the proposed local and central SSCI damping controllers. Although all units are in service in scenarios S1 - S4 (i.e. the adaptive approach implemented at the local SSCI controller has no impact), the local SSCI controller exhibits better performance in S4 compared to its central implementation counterpart in S2. The reason is the different wind speed conditions and different reactive power generations at each wind turbine.

Table 5.1 Simulation scenarios for the different implementations.

Scenario	SSCI Controller	Wind speed	Outage
S1	No SSCI controller	$\sigma(0.7pu, 0.1pu)$	No outage
S2	Central SSCI controller	$\sigma(0.7pu, 0.1pu)$	No outage
S3	Central SSI controller with 2 ms delay in the feedback loop	$\sigma(0.7pu, 0.1pu)$	No outage
S4	Local SSCI controller	$\sigma(0.7pu, 0.1pu)$	No outage
S5	Central SSCI controller	$\sigma(0.7pu, 0.1pu)$	34x4 WTs
S6	Local SSCI controller	$\sigma(0.7pu, 0.1pu)$	34x4 WTs
S7	Central SSCI controller	0.6 pu	No outage
S8	Local SSCI controller	0.6 pu	No outage
S9	Local SSCI controller	0.6 pu	34x4 WTs
S10	Local SSCI controller	0.6 pu	Cluster I and II
S11	Local SSCI controller	0.6 pu	Sudden outage of 34x4 WTs at 1.5s
S12	Local SSI controller with 20 ms delay in the feedback loop	0.6 pu	Sudden outage of 34x4 WTs at 1.5s

It should be noted that the central SSCI damping controller uses the total active and reactive currents produced by the turbine converters resulting in an averaging effect. Moreover, all wind turbine controllers receive the same signal from the central SSCI damping controller although their operating conditions are different. On the other hand, each local SSCI damping controller produces its output signal based on the wind turbine operating conditions.

The delay sensitivity of central implementation is illustrated in Fig. 5.9. The system does not remain stable when there is a 2 ms delay in the feedback loop in scenario S3. The impact of the implemented adaptive approach on the SSCI damping controller becomes apparent in Fig. 5.10.a, which presents the 136-WT outage simulation scenarios for $\sigma(0.7pu, 0.1pu)$ wind speed. The SSCI damping controller in S6 modifies the controller parameters considering the number of units in service, and achieves much better performance compared to its central implementation counterpart in S5. It should be noted that the difference in performance between the central and the local SSCI damping controllers become less noticeable when the parameters of the central control are also modified according to the number of wind turbines in service.

The effectiveness of the central and the local SSCI damping controllers can be observed in Fig. 5.10.b for the permissible slowest wind speed (0.6 pu). In this scenario, there is no wind turbine outage and the wind speeds are the same at all turbines. Hence, the performance difference between the local and central SSCI damping controllers is only due to different

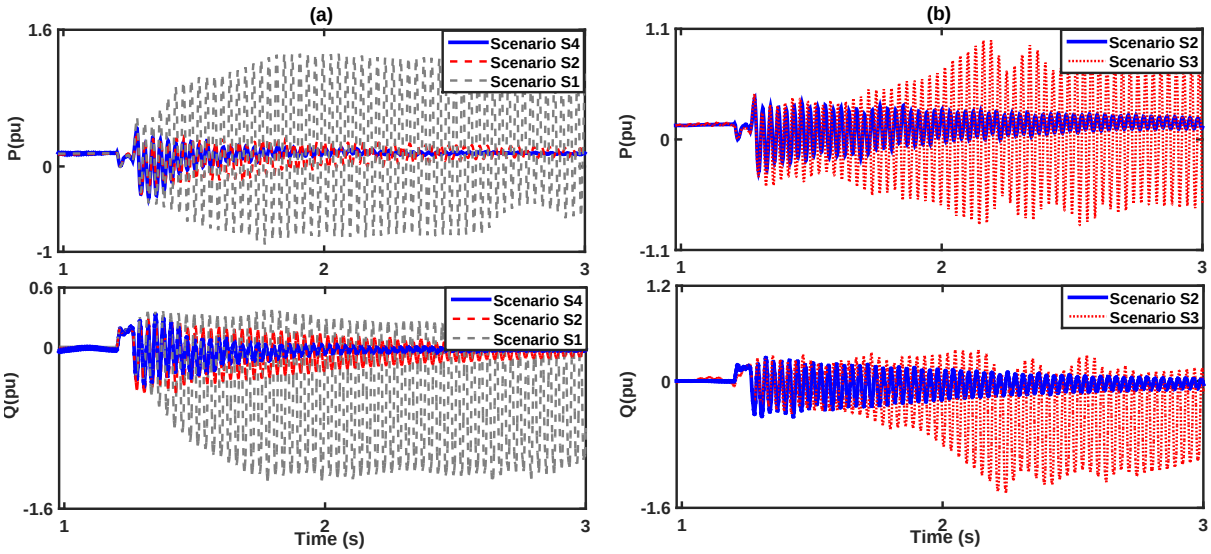

Figure 5.9 Active and reactive power components (a)scenarios S1, S2 and S4, and (b) scenarios S2 and S3.

reactive power generation at each wind turbine. As seen from Fig. 5.10.b, the performance difference is not significant compared to the simulation scenarios in Fig. 5.9.a, and Fig. 5.10.a.

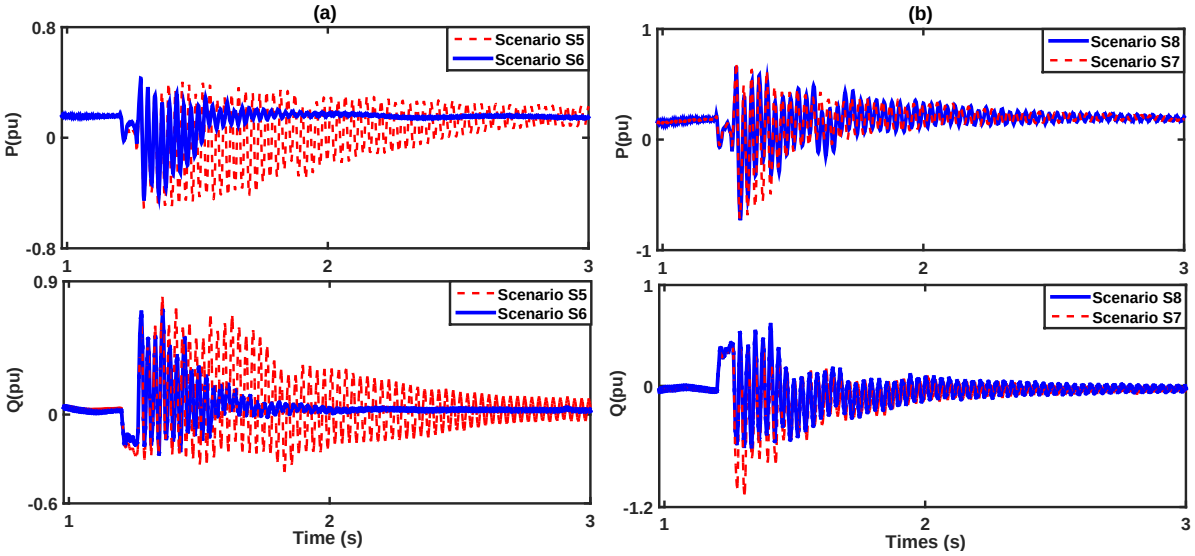

Figure 5.10 Active and reactive power components in (a) scenarios S5 and S6, and (b) scenarios S7 and S8.

The results presented in Fig. 5.11.a demonstrate the effectiveness of the proposed local SSCI controller at the slowest permissible wind speed for various extreme wind turbine outage

scenarios. Modifying the SSCI controller parameters for the wind turbine outages provides the ultimate performance. Moreover, as shown in Fig. 5.11.b, the proposed implementation not only eliminates the high rate data transfer requirement between the turbines and the secondary control layer of the wind farm, but also makes the system immune to excessive (even unrealistic) communication delays.

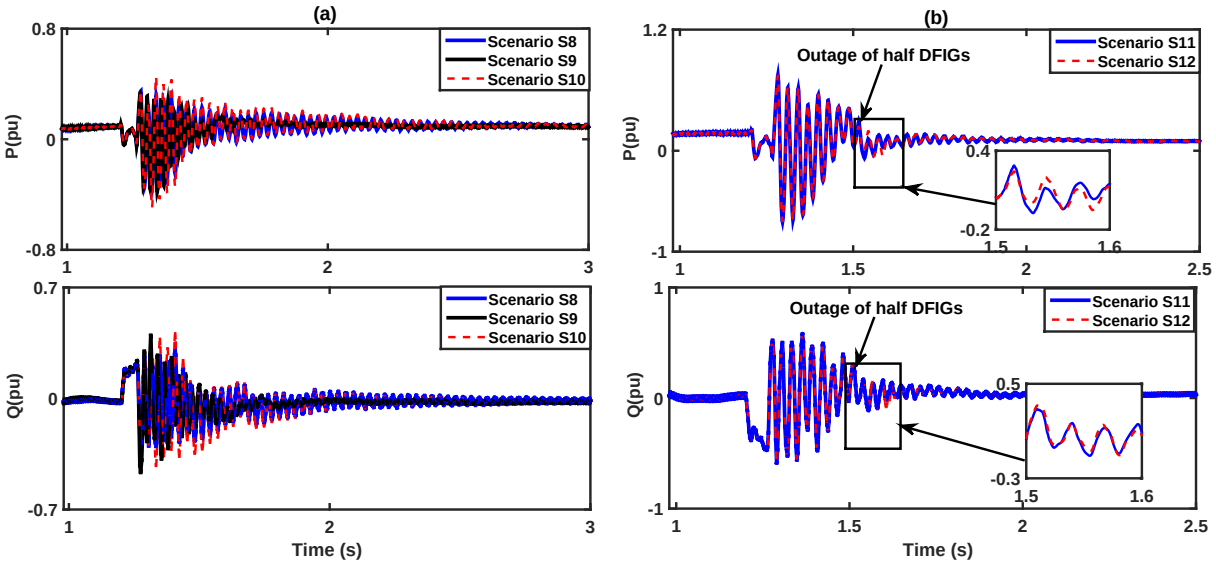

Figure 5.11 Active and reactive power components (a) scenarios S8 - S10, and (b) scenarios S11 and S12.

To confirm the accuracy of the aggregated model, scenarios S1 and S2 are simulated using the aggregated representation of each cluster as shown in Fig. 5.12. The aggregated wind turbine model per-unit (pu) parameters are the same as the single wind turbine pu parameters in aggregation when

$$S_{agg} = NS_{WT} \tag{5.11}$$

where S_{WT} is the single wind turbine base apparent power, N is the number of turbines in aggregation and S_{agg} is the base apparent power for the aggregated wind turbines [27]. The parameters for the equivalent MV collector grid are calculated on the basis of active and reactive power losses in the feeder for the rated current flow from each of the wind turbines.

The simulations with aggregated models are indicated with a * sign. It should be emphasized that the aggregated models for the simulation scenarios S2 and S4 are identical (i.e. S2* and S4* are identical). As the waveforms are practically indistinguishable from the ones presented in Fig. 5.9.a, the differences are presented in Fig. 5.13. As seen in Fig. 5.13.b, the results obtained with the aggregated model are very close to the central SSCI controller

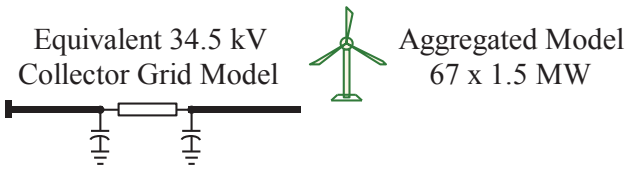

Figure 5.12 Aggregated cluster model.

implementation. This is due to the average wind speed and similar DFIG terminal voltage assumption at each wind turbine in the aggregated model. It should be noted that using the total active and reactive currents of the DFIGs in the central SSCI damping controller has an averaging effect.

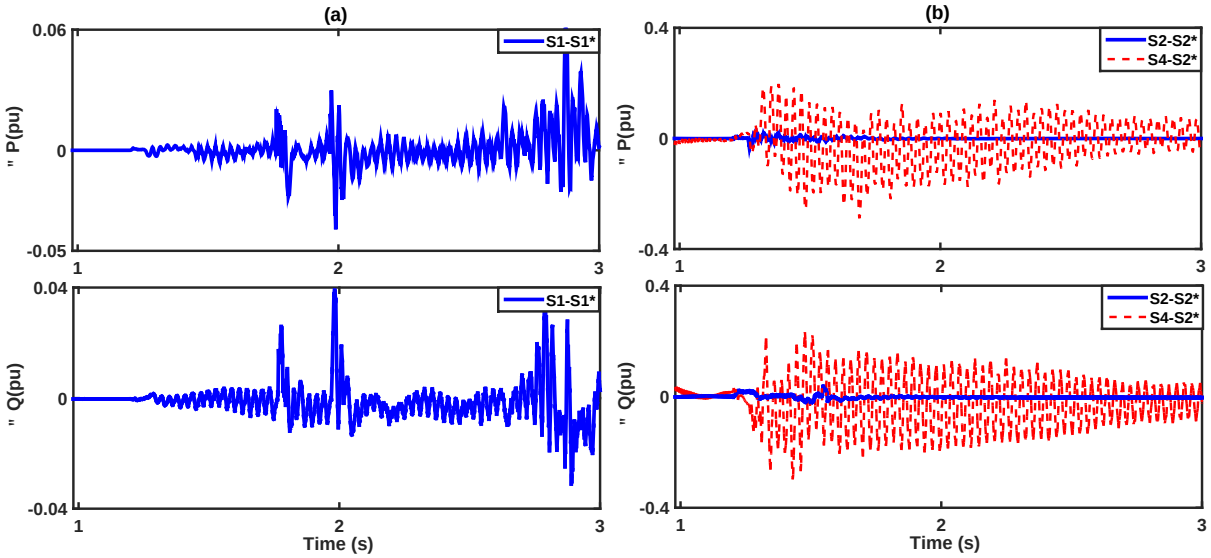

Figure 5.13 Difference in active and reactive powers (a) between scenario S1 and S1*, and (b) between scenarios S2 and S2*, and scenarios S4 and S2*.

5.2 H^∞ and Pole placement

Robust control techniques such as mixed-sensitivity H^∞ control have been employed in the power system for various applications [97, 98, 99, 100]. These approaches only guarantee the stability of a closed-loop system against system uncertainties. However, to achieve robust performance, more desired criteria, e.g., acceptable transient response in the time domain, should be imposed. The linear matrix inequality (LMI) framework allows the designer to

mix the objectives in time and frequency domains. Restricting the closed-loop system poles into a desired region of the s-plane, and mixed-sensitivity design of the H^∞ controller can be merged into a set of LMIs and solved together.

Subsynchronous oscillations are created by sudden variations of the system parameters/signals due to disturbances such as faults. Therefore, minimizing disturbance impact on the system stability is one of the primary objectives of the SSCI damping controller. The robust mixed-sensitivity controller design is an appropriate technique to shape the damping controller. However, the design procedure of the damping controller is often performed based on a simplified system model regardless of the disturbance and unmodeled dynamics. The existing classic control methods perform the control design for a single operating condition, i.e., the plant model is considered fix. Then, the effectiveness of their designed controllers is verified for different operating conditions. Clearly, such controllers are not able to provide the desirable damping for all operating conditions unless the control parameters are adjusted accordingly.

This section proposes a robust mixed-sensitivity H^∞ control with regional pole placement to damp the SSCI oscillations in a DFIG-based wind farm. The main advantage of the proposed controller is its robustness against unmodeled dynamics and the fact that it provides desirable performance characteristics, e.g., disturbance rejection and minimizing control effort. Moreover, by using the pole placement technique, the closed-loop poles are restrained within a desired region where excellent damping of the SSCI modes is achieved. The effectiveness of the designed controller is shown by EMT simulations for single-mode detailed benchmark.

The linearized state-space representation of the system is:

$$\begin{aligned} \dot{\mathbf{x}} &= \mathbf{A}\mathbf{x} + \mathbf{B}\mathbf{u} \\ \mathbf{y} &= \mathbf{C}\mathbf{x} + \mathbf{D}\mathbf{u} \end{aligned} \tag{5.12}$$

where $\mathbf{x}$, $\mathbf{u}$ and $\mathbf{y}$ denote the vectors of the system states, inputs and outputs, respectively. Fig. 5.14 depicts the standard mixed-sensitivity configuration in which the $\mathbf{G}(s)$ and $\mathbf{K}(s)$ are the open-loop system and the proposed controller. The sensitivity transfer function between the disturbance input ($\mathbf{d}$) and the measured output ($\mathbf{y}$) is $\mathbf{S} = (\mathbf{I} - \mathbf{GK})^{-1}$. Therefore, minimizing $\|\mathbf{S}\|_\infty$ results in good disturbance rejection. It is also required that the impact of the disturbance on the controller input be minimized, i.e., $\|\mathbf{KS}\|_\infty$ should be minimized as well. However, the simultaneous minimization of both $\mathbf{S}$ and $\mathbf{KS}$ over all the frequency ranges is not feasible. To reshape these functions over a pre-specified frequency range, the weighting filters $\mathbf{W}_1$ and $\mathbf{W}_2$ are employed. $\mathbf{W}_1$ is a low-pass filter which rejects the low frequency disturbances, whereas $\mathbf{W}_2$ is a high-pass filter which limits the control effort over

high frequency ranges.

The aforementioned configuration is referred to as ($\mathbf{S}/\mathbf{KS}$) mixed-sensitivity design, which is represented as:

$$\min_{\mathbf{K}\in\Omega}\left\|\begin{matrix}\mathbf{W}_1(s)\mathbf{S}(s)\\ \mathbf{W}_2\mathbf{K}(s)\mathbf{S}(s)\end{matrix}\right\|_\infty \quad or \quad \left\|\begin{matrix}\mathbf{W}_1(s)\mathbf{S}(s)\\ \mathbf{W}_2\mathbf{K}(s)\mathbf{S}(s)\end{matrix}\right\|_\infty < \gamma \tag{5.13}$$

where Ω is the set of all stabilizing controllers and γ is a small number whose value determines the robustness of the closed-loop system (the smaller γ, the more robust the closed-loop system).

The state-space representations of the system and weighting filters can respectively be expressed as:

$$\mathbf{G} = \begin{cases}\dot{\mathbf{x}}_G = \mathbf{A}_G\mathbf{x}_G + \mathbf{B}_G\mathbf{u}\\ \mathbf{y}_0 = \mathbf{C}_G\mathbf{x}_G\end{cases} \tag{5.14}$$

$$\mathbf{W}_1 = \begin{cases}\dot{\mathbf{x}}_{\mathbf{W_1}} = \mathbf{A}_{\mathbf{W_1}}\mathbf{x}_{\mathbf{W_1}} + \mathbf{B}_{\mathbf{W_1}}\mathbf{u}_{\mathbf{W_1}}\\ \mathbf{Z}_1 = \mathbf{C}_{\mathbf{W_1}}\mathbf{x}_{\mathbf{W_1}} + \mathbf{D}_{\mathbf{W_1}}\mathbf{u}_{\mathbf{W_1}}\end{cases} \tag{5.15}$$

$$\mathbf{W}_2 = \begin{cases}\dot{\mathbf{x}}_{\mathbf{W}_2} = \mathbf{A}_{\mathbf{W}_2}\mathbf{x}_{\mathbf{W}_2} + \mathbf{B}_{\mathbf{W}_2}\mathbf{u}\\ \mathbf{Z}_2 = \mathbf{C}_{\mathbf{W}_2}\mathbf{x}_{\mathbf{W}_2} + \mathbf{D}_{\mathbf{W}_2}\mathbf{u}\end{cases} \tag{5.16}$$

where $\mathbf{x_G}$, $\mathbf{x_{W_1}}$ and $\mathbf{x_{W_2}}$ are the state vectors of the system, low-pass and high-pass filters, respectively, Fig. 5.14. The state-space representation of the overall open-loop system can be obtained as:

$$\begin{pmatrix}\dot{\mathbf{x}}\\ \mathbf{z}\\ \mathbf{y}\end{pmatrix} = \begin{pmatrix}\mathbf{A} & \mathbf{B}_1 & \mathbf{B}_2\\ \mathbf{C}_1 & \mathbf{D}_{11} & \mathbf{D}_{12}\\ \mathbf{C}_2 & \mathbf{D}_{21} & \mathbf{0}\end{pmatrix}\begin{pmatrix}\mathbf{x}\\ \mathbf{d}\\ \mathbf{u}\end{pmatrix} \tag{5.17}$$

where $\mathbf{x} = [\mathbf{x}_G, \mathbf{x_{W_1}}, \mathbf{x_{W_2}}]^T$, and matrices $\mathbf{d}$ and $\mathbf{z}$ represent the disturbance and regulated output, respectively. Considering the state-space representation of controller $\mathbf{K}(s)$ to be:

$$\begin{aligned}\dot{\mathbf{x}}_K &= \mathbf{A}_K\mathbf{x}_K + \mathbf{B}_K\mathbf{y}\\ \mathbf{u} &= \mathbf{C}_K\mathbf{x}_K + \mathbf{D}_K\mathbf{y}\end{aligned} \tag{5.18}$$

The closed-loop system representation can then be detailed as:

$$\begin{aligned}\dot{\mathbf{x}} &= \mathbf{A_{cl}}(K)\mathbf{x} + \mathbf{B_{cl}}(K)\mathbf{d}\\ \mathbf{z} &= \mathbf{C_{cl}}(K)\mathbf{x} + \mathbf{D_{cl}}(K)\mathbf{d}\end{aligned} \tag{5.19}$$

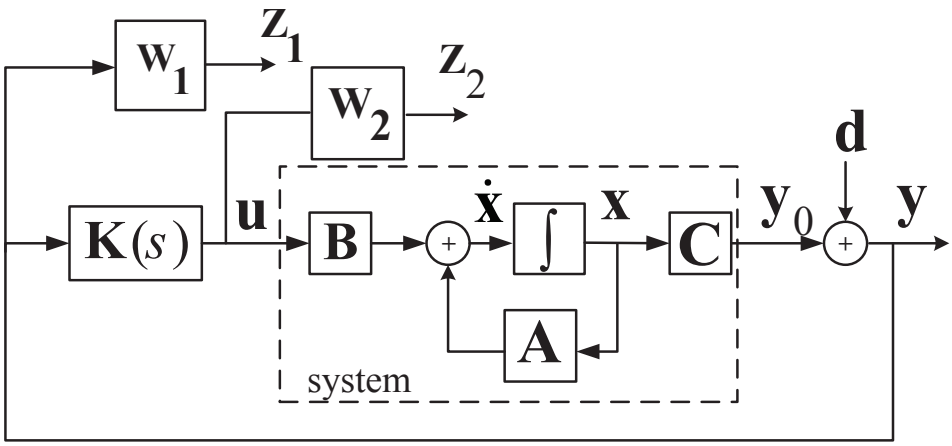

Figure 5.14 The controller design scheme.

$$\mathbf{A_{cl}}(K) = \begin{bmatrix} \mathbf{A} + \mathbf{B}_2\mathbf{D}_K\mathbf{C}_2 & \mathbf{B}_2\mathbf{C}_K \\ \mathbf{B}_K\mathbf{C}_2 & \mathbf{A}_K \end{bmatrix} \tag{5.20}$$

$$\mathbf{B_{cl}}(K) = \begin{bmatrix} \mathbf{B}_1 + \mathbf{B}_2\mathbf{D}_K\mathbf{D}_{21} \\ \mathbf{B}_K\mathbf{D}_{21} \end{bmatrix} \tag{5.21}$$

$$\mathbf{C_{cl}}(K) = \begin{bmatrix} \mathbf{C_1} + \mathbf{D}_{12}\mathbf{D}_K\mathbf{C}_2 & \mathbf{D}_{12}\mathbf{C}_K \end{bmatrix} \tag{5.22}$$

$$\mathbf{D_{cl}}(K) = \mathbf{D}_{11} + \mathbf{D}_{12}\mathbf{D}_K\mathbf{D}_{21} \tag{5.23}$$

Thus, the transfer function matrix between $\mathbf{d}$ and $\mathbf{Z}$ will be:

$$\mathbf{T_{zd}}(s) = \begin{bmatrix} \mathbf{W_1}(s)\mathbf{S}(s) \\ \mathbf{W_2}(s)\mathbf{K}(s)\mathbf{S}(s) \end{bmatrix} = \mathbf{C_{cl}}(K)(s\mathbf{I} - \mathbf{A_{cl}}(K))^{-1}\mathbf{B_{cl}}(K) + \mathbf{D_{cl}}(K) \tag{5.24}$$

To achieve robustness with respect to disturbances, the H^∞ norm of the closed-loop system should be less than γ, i.e., $\|\mathbf{T_{zd}}\|_\infty < \gamma$. It turns out that the closed-loop system is asymptotically stable if the following LMIs hold [96]:

$$\begin{bmatrix} (\mathbf{A_{cl}}(K))^T\mathbf{X} + \mathbf{X}\mathbf{A_{cl}}(K) & \mathbf{B_{cl}}(K) & \mathbf{X}(\mathbf{C_{cl}}(K))^T \\ (\mathbf{B_{cl}}(K))^T & -\gamma\mathbf{I} & (\mathbf{D_{cl}}(K))^T \\ \mathbf{C_{cl}}(K)\mathbf{X} & \mathbf{D_{cl}}(K) & -\gamma\mathbf{I} \end{bmatrix} < 0 \tag{5.25}$$

and

$$\mathbf{X} = \mathbf{X}^T > 0 \tag{5.26}$$

The power system should be able to damp the oscillations with the desired damping. This

is achievable if the closed-loop poles of the system lie in a desired s-plane region as shown in Fig. 5.15 considering the angle θ. It should be noted that the frequency of SSCI modes only depends on the power system parameters e.g., for a series RLC branch $f_n\sqrt{\frac{X_C}{X_L}}$. In other words, the SSCI modes move almost horizontally in the s-plane. Therefore, by moving the closed-loop eigenvalues to the left of the s-plane, the damping will increase. For the sake of simplicity, we move the SSCI poles to the shifted half plane, i.e., $Re(s) \leq -\alpha < 0$); hence, the following Lyapunov equation must hold [96]:

$$\begin{gathered} \mathbf{A}^T\mathbf{P}_{LYP} + \mathbf{P}_{LYP}\mathbf{A} - \mathbf{C}^T\mathbf{W} - \mathbf{W}^T\mathbf{C} + 2\alpha\mathbf{P}_{LYP} < 0 \\ \mathbf{P}_{LYP} > 0 \end{gathered} \tag{5.27}$$

where $\mathbf{P}_{LYP}$ and $\mathbf{W}$ are the solutions of (5.27), and α is the distance between the imaginary axis and the shifted half plane.

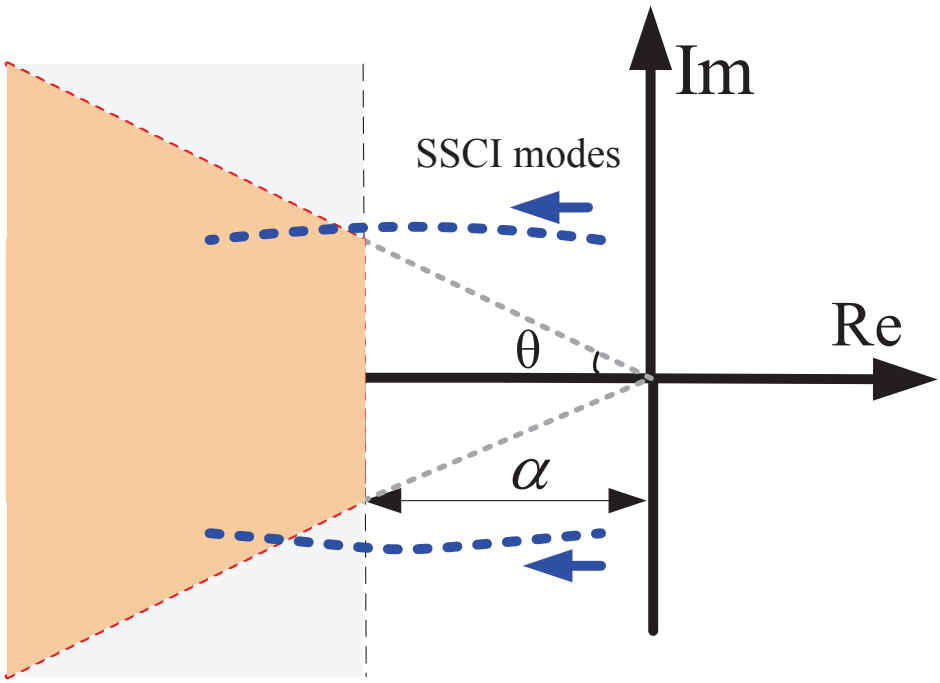

Figure 5.15 The region used for the pole placement technique.

The design specification is feasible if there exist two positive semi-definite matrices $\mathbf{P}_{LYP}$ and $\mathbf{X}$ ($\mathbf{P}_{LYP} = \mathbf{X}$) and the controller $\mathbf{K}$ (i.e., $\mathbf{A}_K, \mathbf{B}_K, \mathbf{C}_K, \mathbf{D}_K$), satisfying (5.25)-(5.27).

Since the inequalities (5.25)-(5.27) are not linear, we apply a change of variables in the controller structure to obtain a set of LMIs [101, 102].

The multi-objective design of the controller can be obtained through appropriate design of

the weighting filters. The main design guidelines for the filters are addressed in [103]. The *hinfmix* function of the *MATLAB LMI Toolbox* has been utilized to design the controller.

The order of the designed controller using the mixed-sensitivity H^∞ approach is equal to the sum of the orders of the system and filters. High order controllers are hard to implement; therefore, a model reduction technique using the Hankel singular value (HSV) is used to reduce the controller order. The HSV of a system represents the amount of energy in each state [103]. Thus, if the states with the highest amount of energy are preserved, the dominant modes of the system are also preserved. The *Robust Control Toolbox* is used to compute the Hankel singular values based on:

$$\sigma_h^i = \sqrt{\lambda_i(\mathbf{MN})} \tag{5.28}$$

where $\mathbf{N}$ and $\mathbf{M}$ are the controllability and observability gramians satisfying the following equations:

$$\mathbf{AM} + \mathbf{MA}^T + \mathbf{BB}^T = 0 \tag{5.29}$$

$$\mathbf{A}^T\mathbf{N} + \mathbf{NA} + \mathbf{C}^T\mathbf{C} = 0 \tag{5.30}$$

The largest Hankel singular value of the system is defined as the Hankel norm ($\sigma_{max}(\mathbf{MN})$) of the system. The Hankel technique proposes a reduced order system such that the infinity norm of the error between the reduced and nominal systems, i.e., $\|\mathbf{G}_{nom} - \mathbf{G}_{red}\|_\infty$, will be minimized. Fig. 5.16 shows the Hankel singular values of the open-loop system. The unstable states correspond to the subsynchronous modes. It can be observed that the SSCI mode contains more energy compared to the other modes. Thus, a reduced-order model of the system with only 2 states will have approximately the same subsynchronous modes. It should be noted that moving certain poles (particularly those corresponding to the mechanical modes) far to the left side of the s-plane requires too much control effort and will result in converter saturation and poor performance.

The weighting function $\mathbf{W}_1$ is chosen as a low-pass filter to desirably shape the closed-loop system at the lower frequency bands. The objective is to effectively reject the disturbance signals with frequencies lower than 5 Hz. The weighting function $\mathbf{W}_2$ is a high-pass filter with a cut-off frequency of 160 Hz in order to minimize the control effort and reject noise and switching harmonics. The magnitude of the low-pass filter over the low-frequency range corresponds to the desired inverse value of the steady-state tracking error. This parameter is obtained using the iterative EMT simulations and observing the impact on the system response of the disturbances, particularly the faults and the wind speed variations. The gain of the low-pass filter over the high-frequency range corresponds to the overshoot. The larger the magnitude of the high-frequency gain is, the more limitation is expected on the

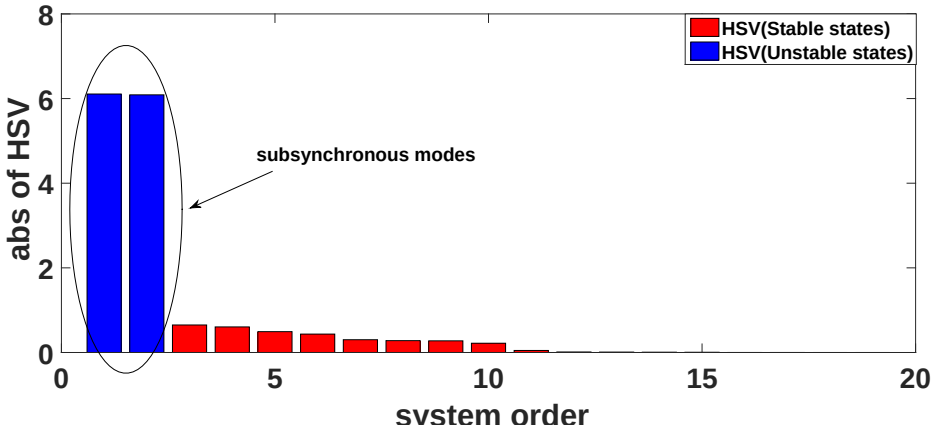

Figure 5.16 Hankel singular of the reduced order system.

overshoot of the system. However, limiting the overshoot will result in an increase of the response-time. Therefore, the magnitude of the high-frequency gain should be obtained from the maximum acceptable overshoot, whose value corresponds to the available capacity of the converters. It should be noted that converter current overshoots which exceed 1.1 pu will result in converter saturation and sluggish behavior of the system. In such a condition, the system may not be able to recover its stability after fault removal. The cut-off frequency of the weighting function $\mathbf{W}_1$ should be chosen so that disturbance rejection is achieved over the low-frequency range. In DFIG-based wind farms, the variation of the wind speed is one of the most frequent disturbances. To reject the impact of such mechanical disturbances, the cut-off frequency of the weighting function $\mathbf{W}_1$ is set to 5 Hz as the mechanical modes have often lower frequencies due to the shaft structure.

To ensure that the system behavior is dominated by frequency response of $\mathbf{W}_1$ in the low-frequency range, the magnitude of the high-pass filter over the low-frequency range is set to zero. In a DFIG-based wind farm, the switching frequencies of the converters can be considered as a major source of noise. Therefore, the cut-off frequency of the transfer function $\mathbf{W}_2$ is chosen so that these frequencies are eliminated in the system response. The high-frequency gain of filter $\mathbf{W}_2$ also corresponds to noise rejection in the closed-loop system. The cut-off frequency of $\mathbf{W}_2$ is chosen to be 160 Hz and the gain is set to 1.5. These values are obtained using the wind farm EMT simulations considering the detailed IGBT models of the converters. It should be noted that the switching frequencies of the RSC and GSC are 2250 Hz and 4500 Hz, respectively. Therefore, the weighting functions are chosen as:

$$\mathbf{W_{1,2}} = \begin{bmatrix} w_{1,2} & 0 & 0 & 0 \\ 0 & w_{1,2} & 0 & 0 \\ 0 & 0 & w_{1,2} & 0 \\ 0 & 0 & 0 & w_{1,2} \end{bmatrix} \tag{5.31}$$

where

$$w_1 = \frac{2.8}{s + 2\pi(5)} \tag{5.32}$$

$$w_2 = \frac{1.5s}{s + 2\pi(160)} \tag{5.33}$$

It should be noted that the gains of the transfer functions w_1 and w_2 correspond to the maximum of the sensitivity function and the limitation on energy of the control signals, respectively [104]. Therefore, these values are obtained from the EMT simulations of the single-mode detailed benchmark which is adopted as the case study in this section.

As discussed before, the frequency of SSCI modes remains almost unchanged for the closed-loop system as they are dependent on the resonance condition of the power system. Hence, the SSCI modes move almost horizontally in the s-plane considering different controller gains. The reduced order model of the system obtained using the Hankel singular value technique only includes the SSCI modes. Therefore, moving these modes toward higher damping can be simplified to moving them to the region specified in Fig. 5.15. This LMI region for the pole placement technique is selected to be the shifted half-plane ($Re(s) \leq \alpha = -4$) to achieve maximum damping and acceptable transient behavior. The value for α is obtained so that the maximum damping (i.e., highest $cos(\theta)$) is achieved while avoiding converter saturation. It should be noted that iterative EMT simulations are required to ensure converter saturation is avoided and maximum damping is achieved. The controller is designed under the severest SSCI conditions, i.e., lowest wind speed and 150 in-service wind turbines.

Table 5.2 shows the scenarios used to demonstrate the effectiveness of the controller at different operating points. In all scenarios, the system is subject to a metallic three-phase fault at bus1 (as shown in Fig. 3.20).

As the wind farm is often modeled with its aggregated model in EMT simulations, the wind speed is always assumed to be fixed at its average value for all of the wind turbines. However, to consider realistic modeling in EMT simulations, the distribution of wind speed among the wind turbines is assumed to have a normal Gaussian distribution. Therefore, the wind speed is different for each turbine, whereas its average value remains similar to the one used in the design of the controller. In Table 5.2, $\sigma(\eta, \beta)$ denotes the normal Gaussian distribution with

the mean value η and the standard deviation β. The active and reactive powers are measured at points A and B of Fig. 3.20 to show the difference between the aggregated and detailed models of the collector grid. In all scenarios, the average model of the DFIG converters is utilized.

Table 5.2 Simulation scenarios for the H^∞ controller.

Scenario	Controller	Wind speed	Wind farm outage
S1	Without SSCI controller	$\sigma(0.7pu, 0.1pu)$	No outage
S2	With SSCI controller	$\sigma(0.7pu, 0.1pu)$	No outage
S3	With SSCI controller	$\sigma(0.7pu, 0.1pu)$	Uniformly (4×34)
S4	Without SSCI controller	0.6 pu	No outage
S5	With SSCI controller	0.6 pu	No outage
S6	Without SSCI controller	0.6 pu	Uniformly (4×34)
S7	With SSCI controller	0.6 pu	Uniformly (4×34)

The injected active and reactive power components in scenario S1 (without the SSCI controller) are shown in Fig. 5.17. The results indicate the instability of the SSCI modes following the fault removal regardless of the aggregated or detailed model of the wind farm.

In scenarios S1-S3, the wind speed has a Gaussian distribution with a mean value and standard deviation of 0.7 pu and 0.1 pu, respectively. In scenarios S4-S7, the wind speed for all turbines is 0.6 pu (i.e., the lowest wind speed).

In S3, S6 and S7, there are 34 wind turbines out-of-service at each cluster without any MV feeder outage. The active and reactive powers at measurement points A and B for scenarios S2 and S3 are presented in Fig. 5.18. It can be observed that the proposed controller is able to damp the oscillations, and the aggregated or detailed modeling of the benchmarks has a negligible impact on the transient behavior of the system assuming the wind speed to be at its average value.

The results presented in Fig. 5.19 demonstrate the effectiveness of the proposed SSCI damping controller for scenarios S4-S7. It should be noted that the pole placement technique results in almost the same damping for all scenarios. As shown in Fig. 5.18 and Fig. 5.19 (see also Fig. 4.17), the SSCI problem becomes severer for slower wind speeds and certain wind turbine outage conditions.

5.3 μ-Controller

Most power systems present models which are highly uncertain due to the continuous changes in configuration, aging of elements, extensions, contingencies and unmodeled dynamics. The

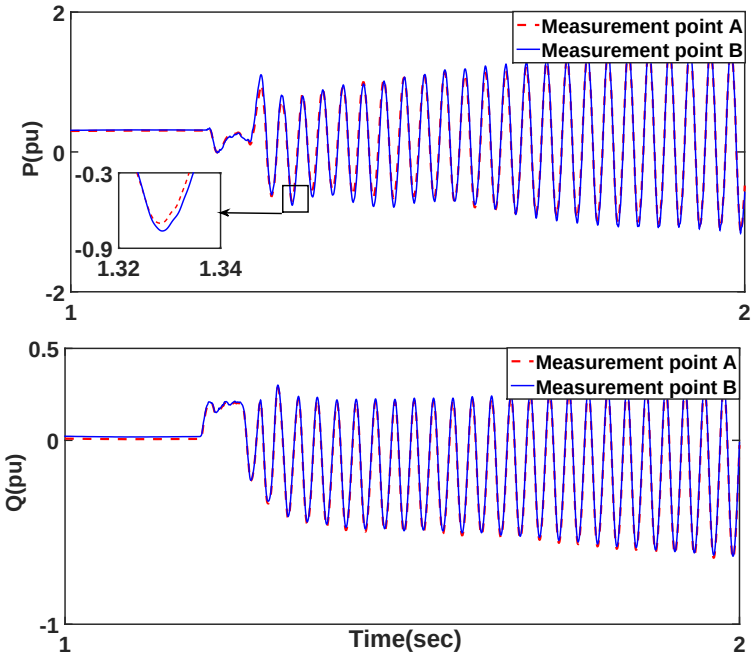

Figure 5.17 Active and reactive powers of the measurement points A and B (scenario S1).

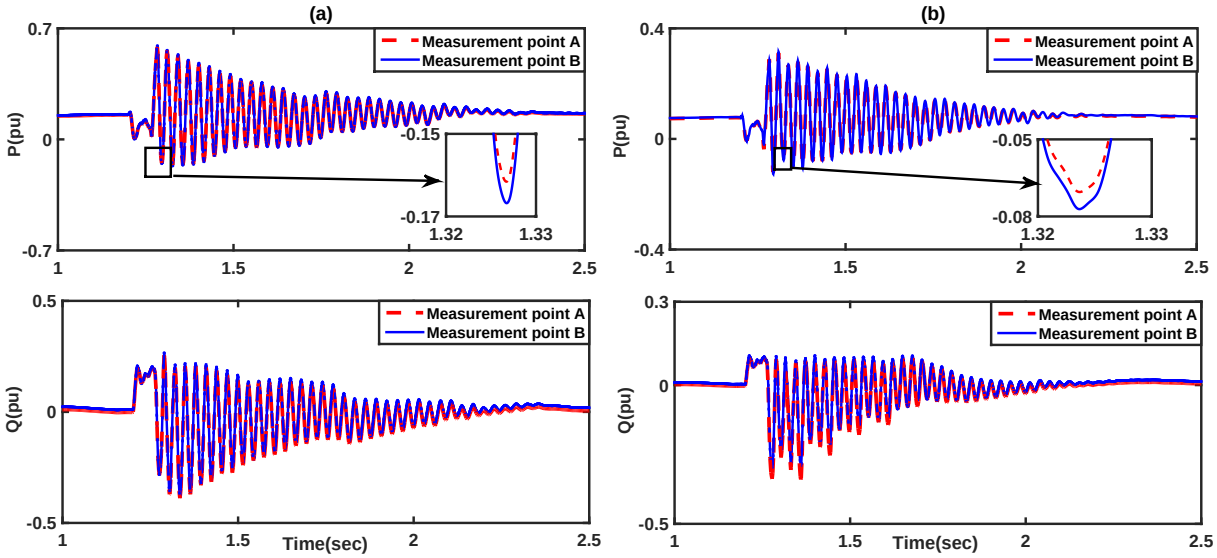

Figure 5.18 Active and reactive powers of measurement points A and B (a) scenario S2, and (b) scenario S3.

collective impact of these uncertainties on the subsynchronous stability (i.e., loci of the SSI modes) has not been fully addressed in the existing literature. Moreover, the existing SSI damping controllers are often designed for systems with fixed and known mathematical mo-

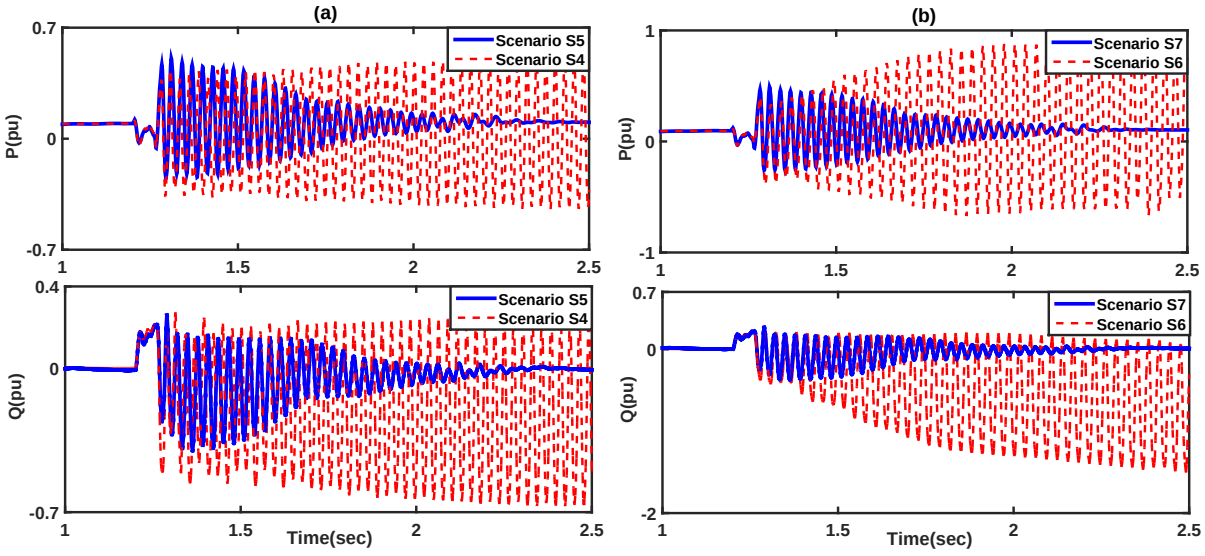

Figure 5.19 Active and reactive powers of measurement point B (a) scenarios S4 and S5, and (b) scenarios S6 and S7.

dels. The uncertainties may result in huge changes in the damping and frequency of the SSI modes, which in turn, can cause system instability. Therefore, the design of robust SSI damping controllers is required.

This section proposes a robust SSI damping controller based on the μ-synthesis technique to tackle the SSCI phenomenon in an uncertain power system. In the design procedure, the uncertain power system is modeled by a series RLC branch whose parameters vary in a certain range. The multi-mode benchmark is used for the design and the simulation.

5.3.1 Robust Analysis

To consider power system uncertainties and wind farm operating conditions, the model has been linearized about an operating point considering its parametric uncertainty. The linearized model of the system can be expressed as:

$$\begin{aligned} \dot{\mathbf{x}} &= \mathbf{A}\mathbf{x} + \mathbf{B}\mathbf{u} \\ \mathbf{y} &= \mathbf{C}\mathbf{x} + \mathbf{D}\mathbf{u} \end{aligned} \tag{5.34}$$

where $\mathbf{x}$, $\mathbf{u}$ and $\mathbf{y}$ are the state vector, control inputs and system outputs, respectively, and matrix $\mathbf{A}$ contains uncertain parameters from the power system side. Fig. 5.20 illustrates the linear fractional transformation (LFT) representation of the closed-loop system, where $\mathbf{P}$ is the nominal open-loop model used to design the controller and perform the robust analysis.

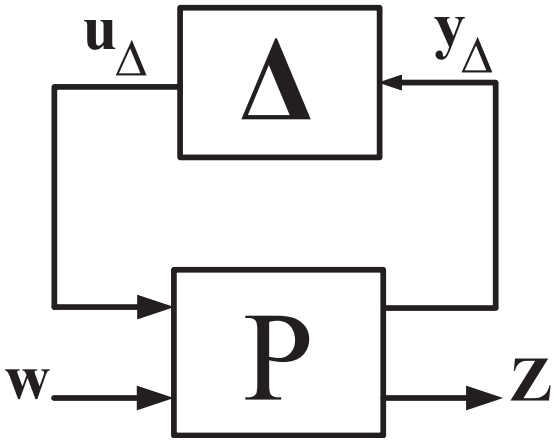

Figure 5.20 Linear fractional transformation of the system.

In the LFT approach, perturbation (also called uncertainty) is modeled as a block-diagonal matrix. Thus, consider the fixed positive integer n and the fixed non-negative integers s, f, $r_1, ..., r_s$ and $m_1, ..., m_f$ such that

$$\sum_{i=1}^{s} r_i + \sum_{j=1}^{f} m_j = n \tag{5.35}$$

With those integers fixed, let δ_i $(1 \leq i \leq s)$ be complex numbers, and Δ_j $(1 \leq j \leq f)$ be $m_j \times m_j$ complex matrices. Consider the matrix $\Delta \in \mathcal{C}^{n \times n}$ with a block-diagonal structure as defined below :

$$\Delta = \text{diag}[\delta_1 \mathbf{I}_{r1}, ..., \delta_s \mathbf{I}_{rs}, \Delta_1, ..., \Delta_f] \tag{5.36}$$

The collection of all such Δ is a class of block-diagonal matrices $\mathbf{\Delta} \subset \mathcal{C}^{n \times n}$:

$$\mathbf{\Delta} = \{\Delta \ : \ \delta_i \in \mathcal{C}, \Delta_j \in \mathcal{C}^{m_j \times m_j} \ , \ 1 \leq i \leq s \ , \ 1 \leq j \leq f\} \tag{5.37}$$

In (5.36) and (5.37), $\mathbf{I}$ is the identity matrix, δ_i represent the scalar or parametric uncertainties, and Δ_j represent the unstructured matrix uncertainties.

It is possible to generalize the above setting to the case where the perturbation itself is a dynamical system represented by a transfer matrix with block-diagonal structure (instead of a constant, complex matrix). To do so, let $\mathcal{M}(\mathbf{S})$ be the set of all stable, proper, rational transfer matrices of order n. Let $\mathbf{\Delta}$ be a block structure as in (5.37). Define the collection

$\mathcal{M}(\mathbf{\Delta})$ of transfer matrices as follows [103]:

$$\mathcal{M}(\mathbf{\Delta}) := \{\Delta \in \mathcal{M}(\mathbf{S}) \ : \ \Delta(s) \in \mathbf{\Delta} \ for \ all \ s\} \tag{5.38}$$

The $\mathcal{M}(\mathbf{\Delta})$ of (5.38) is the set of stable, proper, rational transfer matrices of order n associated with the block structure $\mathbf{\Delta}$. For $\Delta \in \mathcal{M}(\mathbf{\Delta})$, define: $\| \Delta \|_\infty = \sup_\omega(\bar{\sigma}\Delta(j\omega))$.

The resistance, reactance and capacitor impedance of the series line vary within the following uncertainty box.

$$\begin{gathered} 0.02 \ pu < R < 0.035 \ pu \\ 0.4 \ pu < X_L < 0.52 \ pu \\ 0.05 \ pu < X_C < 0.07 \ pu \end{gathered} \tag{5.39}$$

Subsequent to a fault or system reconfiguration, the resistance and inductance observed from the DFIG terminals will change, whereas the capacitor will remain fixed at its nominal value. Fig. 5.21 shows the real part of the SSI mode in terms of the resistance and inductance, and Fig. 5.22 shows the stability regions.

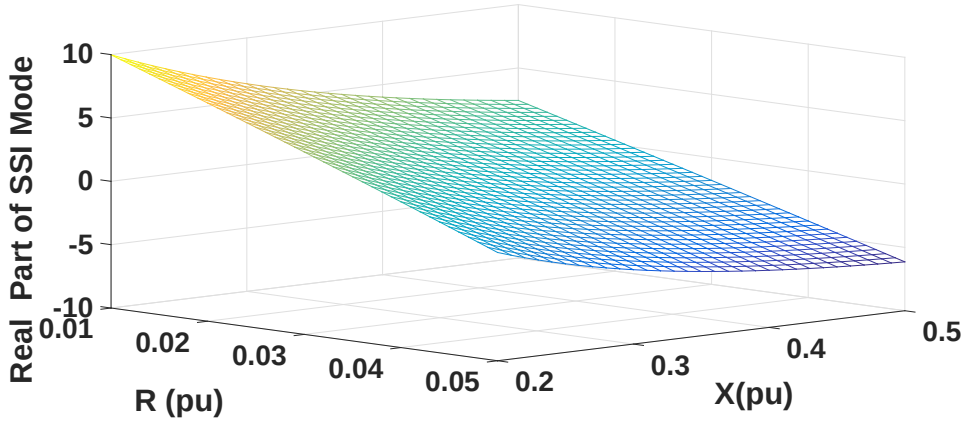

Figure 5.21 SSI mode variation versus simultaneous change in R and X.

Fig. 5.23 shows the singular values of the open-loop system (the system without the SSCI damping controller) for 10 uniformly chosen uncertainties in R, X and X_C. The worst-case scenario (severest oscillations) occurs when R, X and X_C are 0.0281 pu, 0.4034 pu and 0.07 pu, respectively. In this scenario, the frequency of the SSI oscillations is 41 Hz.

In general, given a fixed $\mathbf{M} \in \mathcal{C}^{n\times n}$ and a fixed block structure $\mathbf{\Delta}$, the structured singular value of $\mathbf{M}$ (with respect to $\mathbf{\Delta}$) is denoted by $\mu_{\mathbf{\Delta}}(\mathbf{M})$ and is defined [104]:

$$\mu_{\mathbf{\Delta}}(\mathbf{M}) := \frac{1}{\inf\{\bar{\sigma}(\Delta) \ : \ \Delta \in \mathbf{\Delta}, \det(\mathbf{I} - \mathbf{M}\Delta) = 0\}} \tag{5.40}$$

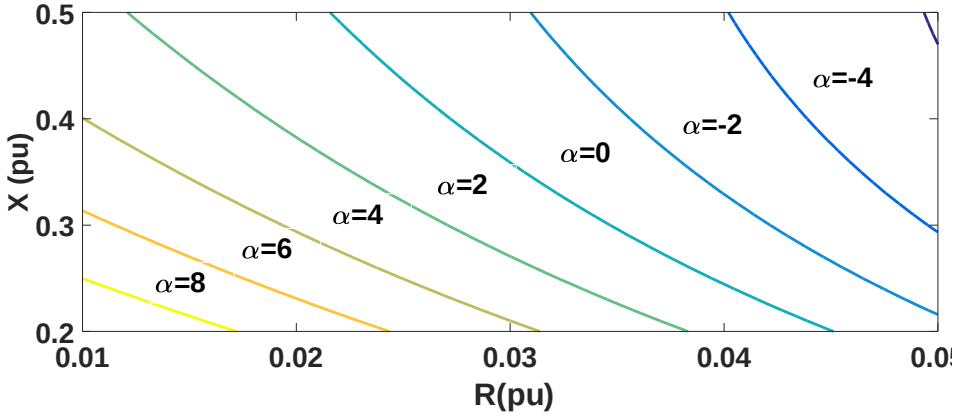

Figure 5.22 Damping of SSI versus simultaneous change in R and X.

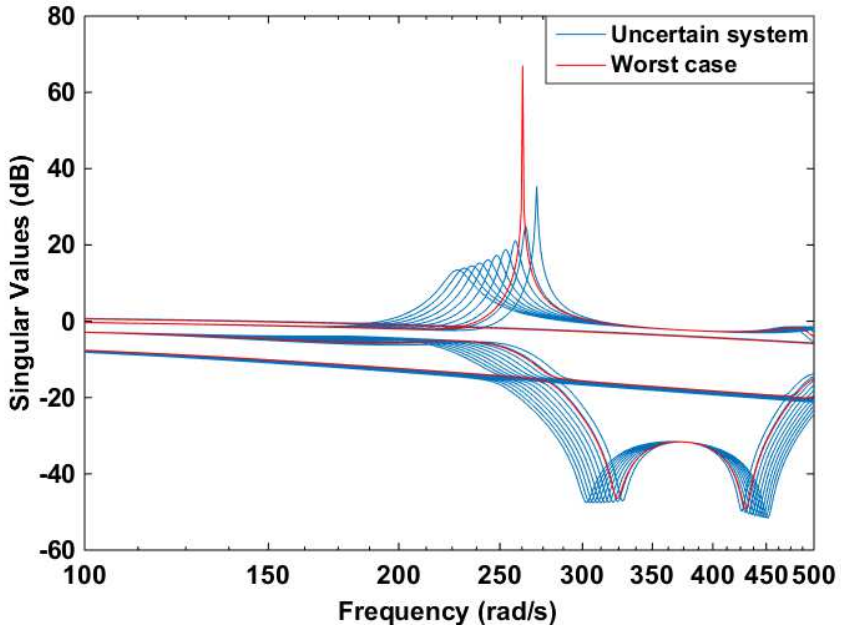

Figure 5.23 Singular values of the uncertain system.

If there is no $\Delta \in \mathbf{\Delta}$ for which $det(\mathbf{I}-\mathbf{M}\Delta) = 0$, then $\mu_{\mathbf{\Delta}}(\mathbf{M})$ is defined to be zero. Structured singular values are defined and used for transfer matrices as well. To do so, definition (5.40) is invoked at each $s \in \mathcal{C}$ where the transfer matrix is defined; the structured singular value in this case is a function of s. For the nominal open-loop transfer matrix $\mathbf{P}$ in Fig. 5.20, the structured singular value is denoted by $\mu_{\mathbf{\Delta}}(\mathbf{P}(s))$ at each s where $\mathbf{P}(s)$ is defined. The following is a statement on robust stability. Let the $\mathbf{P}$ in Fig. 5.20 be a stable, proper, rational transfer matrix of order n; $\beta > 0$ be a positive number; $\mathcal{M}(\mathbf{\Delta})$ be as in (5.38). For

all $\Delta \in \mathcal{M}(\mathbf{\Delta})$ with $\|\Delta\|_\infty \leq \beta$, the perturbed closed-loop system in Fig. 5.20 is well-defined and stable if and only if $sup_\omega \, \mu_\Delta(\mathbf{P}_{11}(j\omega)) < \frac{1}{\beta}$, [103].

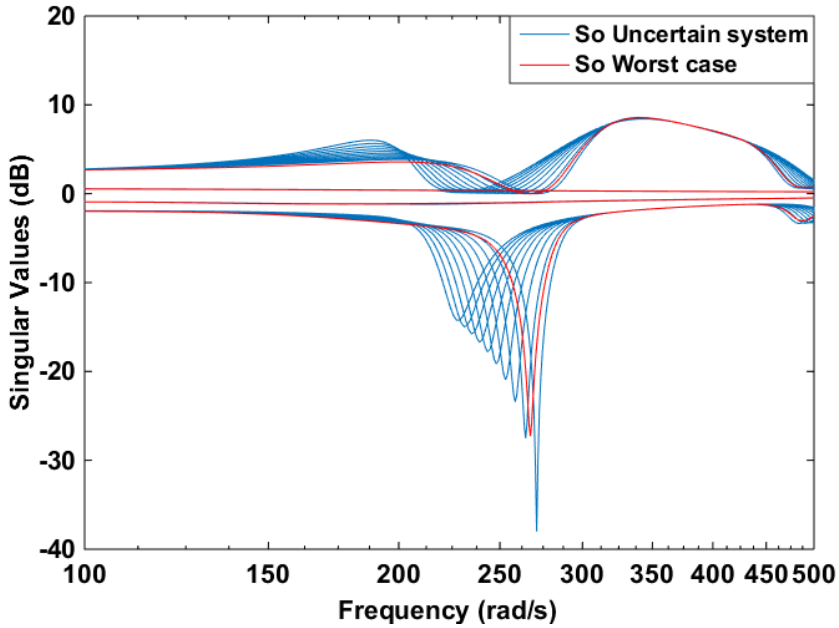

Figure 5.24 Singular values of the sensitivity transfer function.

Robust stability is not the only concern in the analysis of uncertain systems. The closed-loop system should also meet several performance criteria, e.g., good tracking and disturbance rejection. The singular values of the sensitivity transfer function ($\mathbf{S}_o = (\mathbf{I} - \mathbf{GK})^{-1}$) are shown in Fig. 5.24. The lower and upper bounds of the stability margin are 0.4141 and 0.7952, respectively. The family of the open-loop systems is not stable, in particular when the parameters exceed their nominal values by 41.4%. Increasing R, X and X_C by 25% results in a 4%, 3% and 9% decrease in the stability margin, respectively. The system is also unable to meet the robust performance criteria. The lower and upper bounds of the performance are 0.0549 and 0.0556, respectively. The 25% increase in R, X and X_C will result in a 1%, 2% and 2% decrease in the performance margins, respectively. The upper and lower bounds of μ are shown in Fig. 5.25. As the upper bound of μ exceeds 1 over a frequency range, the system is not robustly stable.

5.3.2 μ-Synthesis

Fig. 5.26 shows the control design schematic diagram. The controller model is denoted by $\mathbf{K}$, and $\mathbf{u}_\mathbf{\Delta}$ and $\mathbf{y}_\mathbf{\Delta}$ are the inputs and outputs of the uncertainty block.

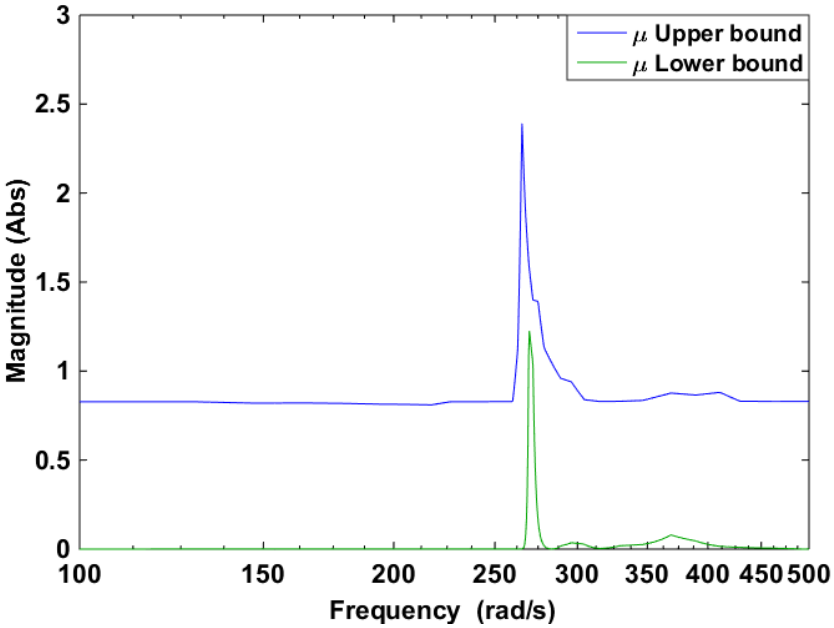

Figure 5.25 Upper and lower μ bounds.

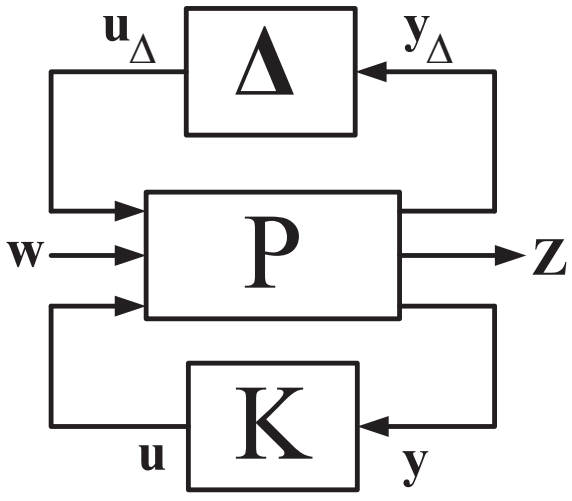

Figure 5.26 Standard $\mathbf{M} - \mathbf{\Delta}$ configuration for the controller design.

The LFT of the family of systems which need to be controlled can be expressed as:

$$\{F_u(\mathbf{P}, \Delta) : \Delta \in \mathcal{M}(\mathbf{\Delta}), \sup_{\omega}(\bar{\sigma}(\Delta(j\omega)) \leq 1)\} \tag{5.41}$$

where subscript u of the function $F_u(\mathbf{P}, \Delta)$ denotes the use of upper LFT configuration in the controller design, Fig. 5.26. The controller $\mathbf{K}$ should stabilize the closed-loop for all $\Delta \in \mathcal{M}(\mathbf{\Delta})$. The μ-synthesis technique minimizes the peak of the structured singular value of $F_L(\mathbf{P}, \mathbf{K})$ over the set of all stabilizing controllers (Ω), i.e.,

$$\min_{\mathbf{K}\in\Omega} \max_{\omega} \mu_{\Delta_P}(F_L(\mathbf{P}, \mathbf{K})(j\omega)) \tag{5.42}$$

where L subscript of $F_L(\mathbf{P}, \mathbf{K})$ denotes the use of lower LFT configuration, and Δ_P is the extended uncertainty block described as:

$$\Delta_P = \{\begin{bmatrix} \Delta & 0 \\ 0 & \Delta_F \end{bmatrix} : \Delta \in \mathbf{\Delta}, \Delta_F \in \mathcal{C}^{n_w \times n_Z}\} \tag{5.43}$$

In (5.43), Δ_F, n_w and n_Z are, respectively, a fictitious complex (unstructured) uncertainty block, the size of the reference vector and the size of the controlled output vector, Fig. 5.26. The control scheme of the system is illustrated in Fig. 5.27, where $\mathbf{d}$ is disturbance, $\mathbf{r}$ is reference, and $\mathbf{Z}$ is the error output.

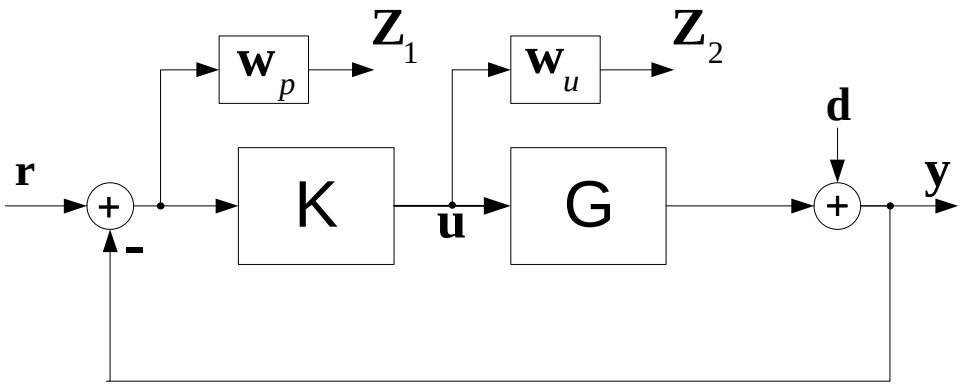

Figure 5.27 Block diagram of the closed-loop system for the controller design.

The design goal is to achieve robust stability and robust performance for the following family of uncertain systems.

$$\mathbf{Z} = \mathbf{T_{ZR}}\mathbf{R} \tag{5.44}$$

where

$$\mathbf{Z} = \begin{pmatrix} \mathbf{Z_1} \\ \mathbf{Z_2} \end{pmatrix} \qquad \mathbf{R} = \begin{pmatrix} \mathbf{r} \\ \mathbf{d} \end{pmatrix} \tag{5.45}$$

and

$$\mathbf{T_{ZR}} = \begin{pmatrix} \mathbf{W}_p\mathbf{S}_o & -\mathbf{W}_p\mathbf{S}_o \\ \mathbf{W}_u\mathbf{K}\mathbf{S}_o & -\mathbf{W}_u\mathbf{K}\mathbf{S}_o \end{pmatrix} \tag{5.46}$$

The weighting functions are used to shape the frequency response of the closed-loop system. $\mathbf{W_p}$ is a low-pass filter used to reject the disturbance in low frequency ranges. $\mathbf{W_u}$ is a high-pass filter which minimizes the control effort and rejects the switching harmonics. In our design, the objective is to reject the disturbances below 5 Hz, and to attenuate the switching frequencies of the RSC ($f_{RSC_{sw}}$=2250 Hz) and GSC ($f_{GSC_{sw}}$ =4500 Hz). Therefore, the weighting matrices are obtained as below:

$$\mathbf{W_p} = \begin{pmatrix} W_p & 0 & 0 & 0 \\ 0 & W_p & 0 & 0 \\ 0 & 0 & W_p & 0 \\ 0 & 0 & 0 & W_p \end{pmatrix} \qquad W_p = \frac{0.01(s+10)}{(s+2\pi(5))} \tag{5.47}$$

$$\mathbf{W_u} = \begin{pmatrix} W_u & 0 & 0 & 0 \\ 0 & W_u & 0 & 0 \\ 0 & 0 & W_u & 0 \\ 0 & 0 & 0 & W_u \end{pmatrix} \qquad W_u = \frac{0.1(0.001s+1)}{(0.0001s+1)} \tag{5.48}$$

It should be noted that similar to the weighting design procedure for a mixed-sensitivity H^∞ controller, the gains of W_p and W_u correspond to the maximum of the sensitivity function and the energy of the control effort signal, respectively. In this section, the transfer functions W_p and W_u are obtained using the same guidelines proposed for the weighting factors in the mixed-sensitivity H^∞ technique. Moreover, the value of the structured singular value should be considered to ensure its value is below 1. The linear closed-loop system simulations in MATLAB and detailed EMT simulations in EMTP-RV demonstrate acceptable transient behavior. The DK-iteration method is used to compute the controller parameters. The order of the controller is then reduced using the Hankel singular value approach [103]. Fig. 5.28 shows that reducing the controller order to 6 will not affect its performance.

Fig. 5.29 illustrates the lower and upper bounds of μ, which also shows a reduction in the peak value of μ. Fig. 5.30 shows the singular values of the closed-loop system and the worst gain scenario.

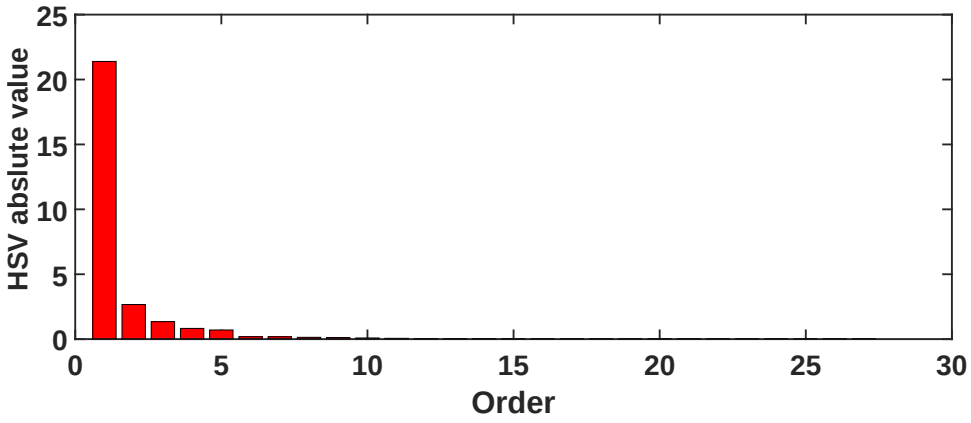

Figure 5.28 Hankel singular values of the controller.

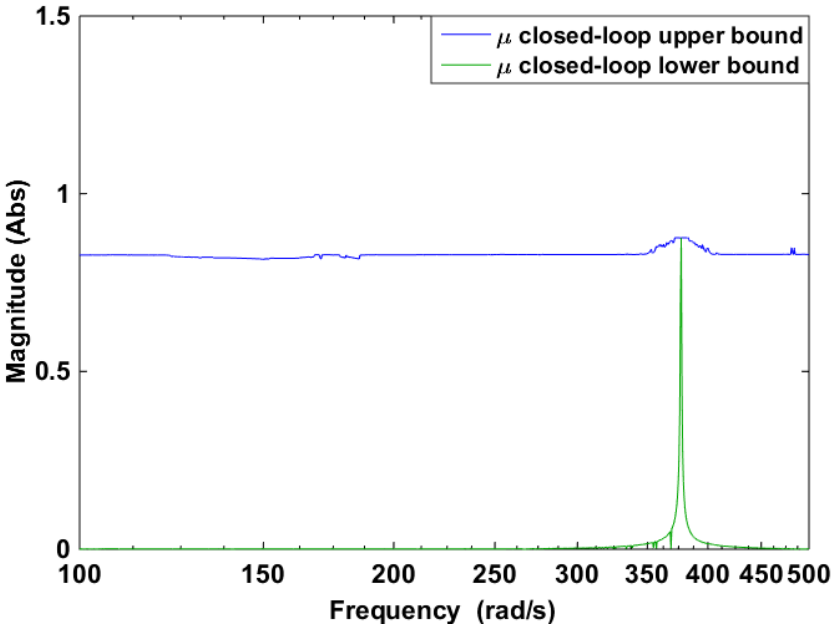

Figure 5.29 Closed-loop upper and lower bounds of the μ.

Table 5.3 presents the simulation scenarios used to demonstrate the effectiveness of the controller. The simulation step time is 50 us. The simulations are performed using EMTP-RV software and the generic wind farm model in [84]. The fault locations F1 - F4 are illustrated in Fig. 5.31. Three-phase metallic fault is applied at t=1 s in scenarios S1 - S6 (i.e. at F1 - F3). The faults F1, F2 and F3 occur, respectively, at those ends of the transmission lines A, B and C that are connected to the wind farm. Those faults are cleared with the operation of the line circuit breakers. The close and remote breakers operate at 60 ms and 80 ms, respectively. On

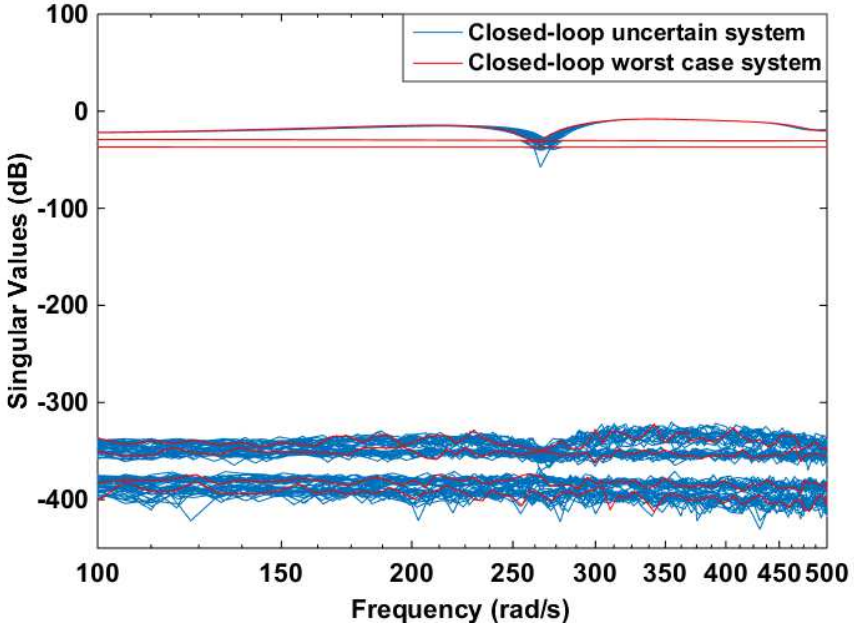

Figure 5.30 Singular values of the closed-loop uncertain system.

the other hand, the three-phase fault F4 in scenario S7 and S8 takes place at the terminal of the Thevenin source of the Equivalent System-B, Fig. 5.31. The fault impedance is 0.3162 Ω and $\frac{X}{R} = 3$. This fault is cleared with the operation of the Equivalent System-B end circuit breaker of the line after 300 ms. This fault scenario imitates a fault inside the Equivalent System-B and its clearance with the operation of the backup protection (such as due to breaker failure) which involves the breakers of the busbar to which transmission line B is connected. It should be noted that scenario S7 and S8 are repeated for different types of faults as well as system impedances that result in 0.5 pu to 0.8 pu voltage sag at DFIG terminals. However, these results are not presented in this section due to similar performance of the controller. In all the scenarios, the wind speed is 0.6 pu (i.e. the permissible slowest wind speed) and there are no WT outages inside the wind farm.

Figs. 5.32-5.33 show the active and reactive powers delivered by the aggregated wind turbine for scenarios S1 - S8. The system is unstable without the SSCI damping controller in all scenarios and the frequency of the SSCI mode is similar to the ones obtained through the frequency scan and eigenvalue analysis. The simulation results presented in those figures also confirm the effectiveness of the proposed SSCI damping controller. The μ-synthesis technique used stabilizes the system in all the scenarios in spite of the dramatic differences between the SSCI mode frequencies and initial dampings. Although the SSCI mode has negative damping

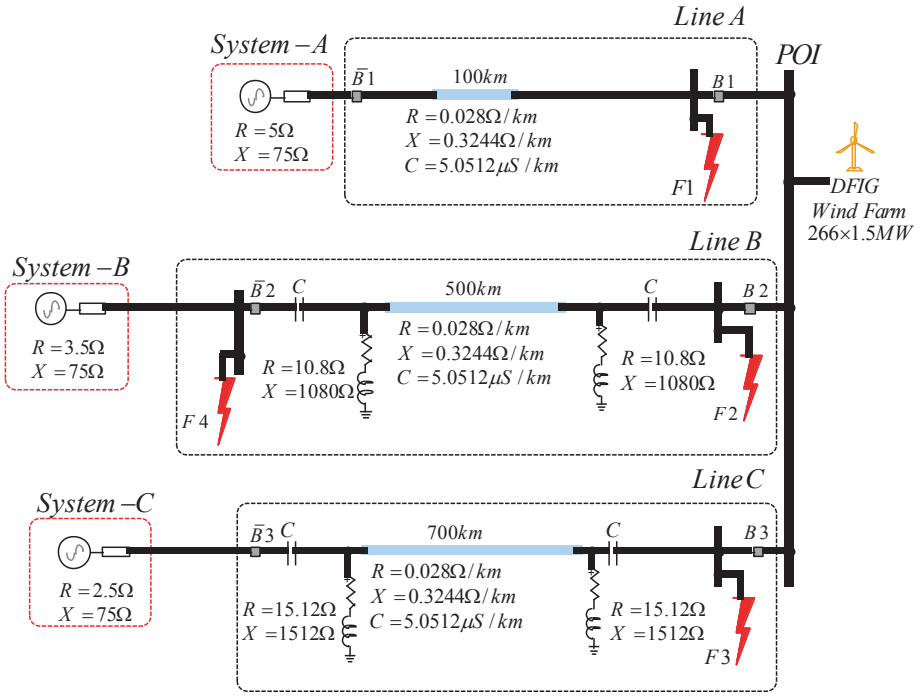

Figure 5.31 Test system under study.

Table 5.3 Simulation scenarios (+) with SSI controller, (-) without SSI controller.

Scenario	Fault location	Line outage (prior to fault)	Line outage (after fault)	SSCI controller
S1	F1	-	Line A	-
S2	F1	-	Line A	+
S3	F2	Line A	Lines A and B	-
S4	F2	Line A	Lines A and B	+
S5	F3	Line A	Lines A and C	-
S6	F3	Line A	Lines A and C	+
S7	F4	Line A	Lines A and B	-
S8	F4	Line A	Lines A and B	+

during fault in scenarios S7 and S8 (see Fig. 5.33), the system remains stable after fault removal with the proposed mitigation. As seen from Fig. 4.17, the system becomes most vulnerable to SSCI when there are 150 WTs in service. To demonstrate the effectiveness of the proposed damping controller in such extreme WT outage conditions, scenarios S2, S4, S6 and S8 are repeated for the case in which 150 WTs are in service in the wind farm. Those simulation scenarios are indicated with a "$*$" sign. The results presented in Fig. 5.34 show that the proposed damping controller stabilizes the system effectively in those wind turbine

outage scenarios as well.

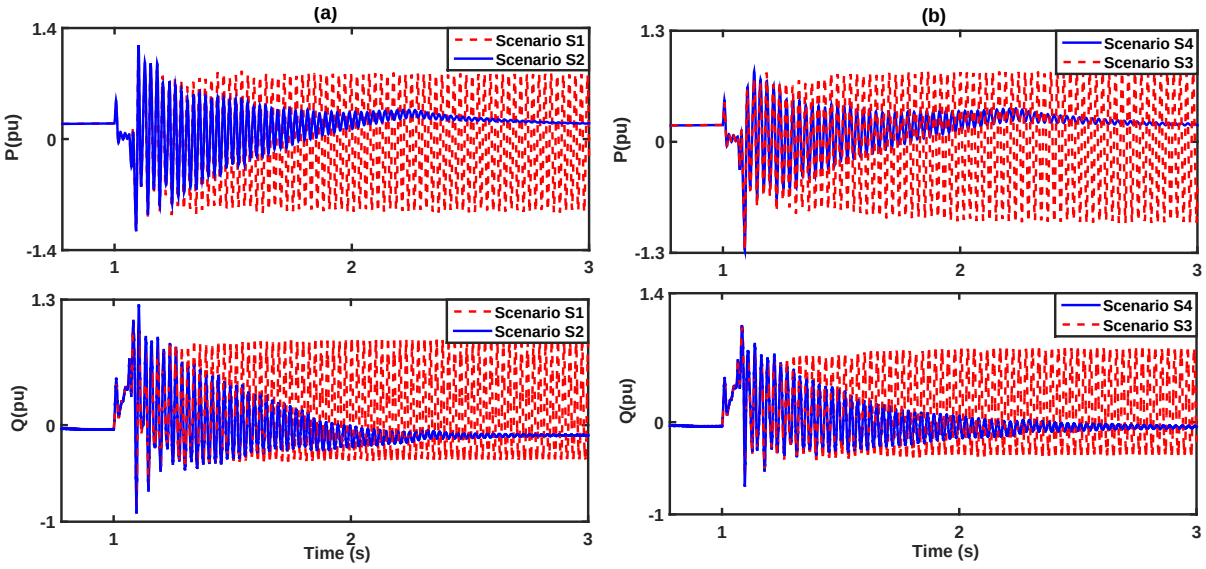

Figure 5.32 Active and reactive power components of the aggregated WT in (a) scenarios S1 and S2, and (b) scenarios S3 and S4.

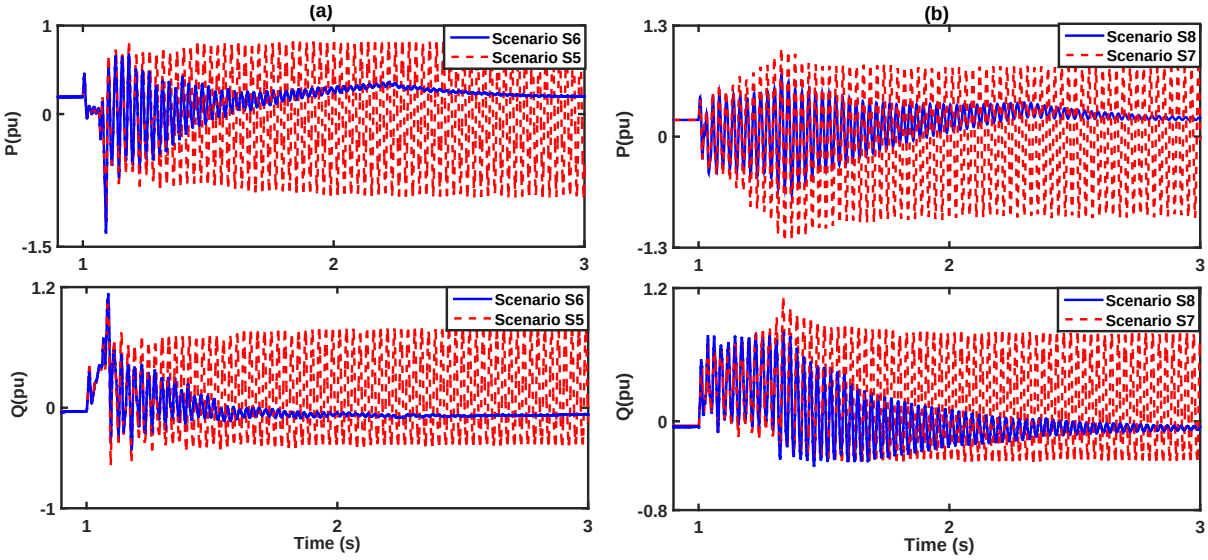

Figure 5.33 Active and reactive power components of the aggregated WT in (a) scenarios S5 and S6, and (b) scenarios S7 and S8.

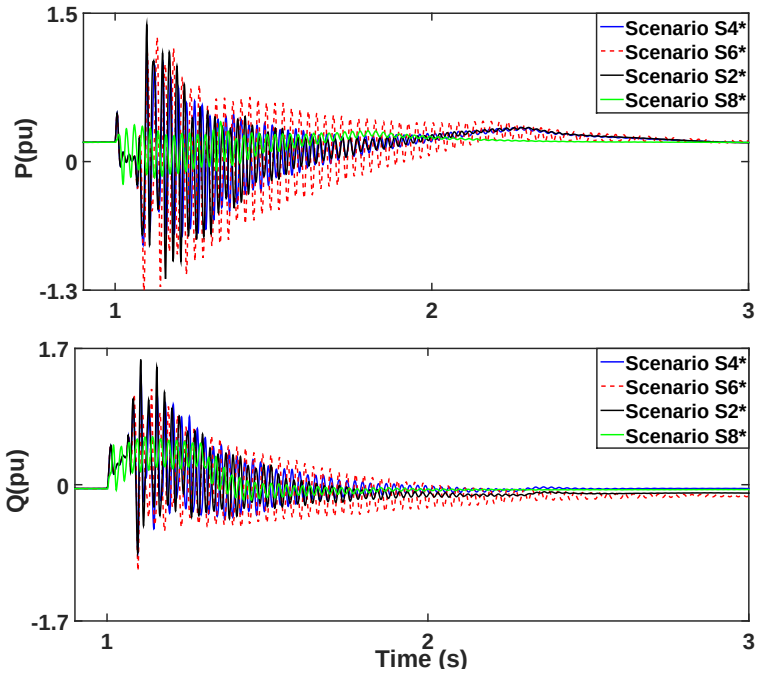

Figure 5.34 Active and reactive power components of the aggregated WT in scenarios S2*, S4* and S6*.

5.4 Controller and Time Delay

In power system applications, the presence of time-delay is often ignored for the sake of simplification, or since the delay is often very small when the measurements are local. The main sources of delay are communication systems and sensor devices. The time delay considerably increases when a secondary control layer is implemented in a distributed system over vast areas, e.g., wind farms. The impact of time delay on the stability of the power system stabilizer (PSS), TCSC, SVC and load frequency control has been studied in [10, 105, 106, 107].

The time delay is often considered to be constant. However, in a realistic system, it can be modeled as a random variable distributed uniformly over an interval. Therefore, it is essential to obtain the maximum amount of time delay that a system can tolerate before it becomes unstable. This time delay is referred to as the stability delay margin [108]. The characteristic equation of a time-delayed system, obtained by setting the dominator of the closed-loop transfer function equal to zero, is transcendental, and thus, the system's stability cannot be assessed using conventional tests. The commonly used methods for determining the delay margin of a system are addressed in [109, 108, 110]. Among these methods, the most well-known one is the Rekasius substitution [108, 110]. This method benefits from the substitution of the transcendental term with its equivalent transfer function on the imaginary axis of

the s-plane. However, this method suffers from large computational burden, particularly for complex and large-scale systems. Therefore, a new algorithm based on the Rekasius substitution and the Guardian Map Theory [9] is introduced to reduce the computational burden of delay margin calculation.

In a typical wind farm, turbines are distributed over vast areas. These turbines communicate with the secondary level controllers (e.g., SSCI damping controller) using communication links. These links are subject to delays whose values depend on the distance and the technology used to transfer the data. This type of delay is mostly ignored in practice; however, it may have a significant effect on the system's stability particularly in the case of the subsynchronous phenomenon.

The linear time invariant (LTI) system can be expressed as:

$$\begin{aligned} \dot{\mathbf{x}} &= \mathbf{A}\mathbf{x} + \mathbf{B}\mathbf{u} \\ \mathbf{y} &= \mathbf{C}\mathbf{x} + \mathbf{D}\mathbf{u} \end{aligned} \tag{5.49}$$

where $\mathbf{A} \in \mathcal{R}^{n\times n}$, $\mathbf{B} \in \mathcal{R}^{n\times m}$, $\mathbf{C} \in \mathcal{R}^{r\times n}$ and $\mathbf{D} \in \mathcal{R}^{r\times m}$ are the matrices used to specify the small signal behavior of the system. n, m and r are the number of state, input and output signals, respectively. The dynamics of the designed controller in the secondary level can also be expressed as:

$$\begin{aligned} \dot{\mathbf{x}}_K &= \mathbf{A}_K\mathbf{x}_K + \mathbf{B}_K\mathbf{y} \\ \mathbf{u} &= \mathbf{C}_K\mathbf{x}_K + \mathbf{D}_K\mathbf{y} \end{aligned} \tag{5.50}$$

where K subscript represents the matrices describing the damping controller. Fig. 5.35 shows the control scheme of the system, where $\mathbf{y}^\tau$ denotes the delayed measurement signals. The state-space representation of the closed-loop system can be obtained as:

$$\begin{bmatrix} \dot{\mathbf{x}} \\ \dot{\mathbf{x}}_K \end{bmatrix} = \begin{bmatrix} \mathbf{A} & \mathbf{B}\mathbf{C}_K \\ 0 & \mathbf{A}_K \end{bmatrix} \begin{bmatrix} \mathbf{x} \\ \mathbf{x}_K \end{bmatrix} + \begin{bmatrix} 0 & 0 \\ \mathbf{B}_K\mathbf{C} & 0 \end{bmatrix} \begin{bmatrix} \mathbf{x}^\tau \\ \mathbf{x}_K^\tau \end{bmatrix} \tag{5.51}$$

The stability of the considered system can be assessed using the location of the roots of the characteristic equation detailed as:

$$\Delta(s,\tau) = \det(s\mathbf{I} - \bar{\mathbf{A}} - \bar{\mathbf{A}}_\tau e^{-s\tau}) = \sum_{k=0}^{n} a_k(s)e^{-ks\tau} \tag{5.52}$$

$$\bar{\mathbf{A}} = \begin{bmatrix} \mathbf{A} & \mathbf{B}\mathbf{C}_K \\ 0 & \mathbf{A}_K \end{bmatrix} \tag{5.53}$$

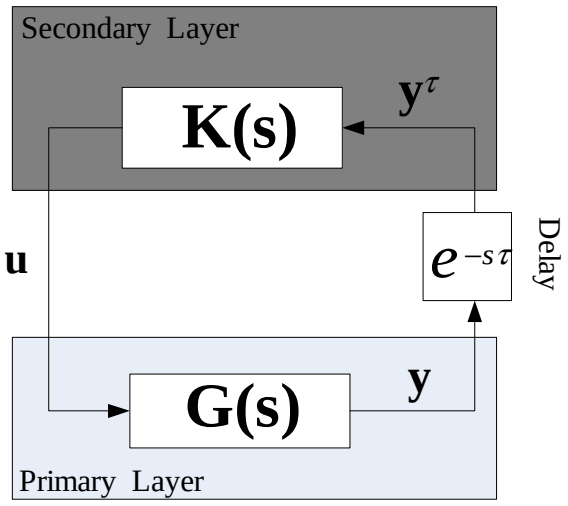

Figure 5.35 The control scheme for analyzing the stability delay margin.

$$\bar{\mathbf{A}}_\tau = \begin{bmatrix} 0 & 0 \\ \mathbf{B}_K\mathbf{C} & 0 \end{bmatrix} \tag{5.54}$$

where $a_K(s)$ are polynomials in the s-plane with real coefficients. Assuming $\gamma^\tau = \{\gamma_1^\tau, ...\}$ to be the set of the roots of the equation $\Delta(s,\tau) = 0$, the system is small-signal stable if and only if [10]:

$$\max\{Re(s) \ : \ s \in \gamma^\tau\} < 0 \tag{5.55}$$

Based on the criterion presented in (5.55), delay systems can be categorized into two major types namely, delay-dependent and delay-independent systems. A dynamic system is delay-independent if (5.55) holds for all values of τ and is delay-dependent if there exists a value (τ^*) in which the system is stable for $\tau < \tau^*$ and is not stable for $\tau \geq \tau^*$.

The exponential terms ($e^{-k\tau s}$) result in the transcendental characteristic equation (5.52). Therefore, the roots of this equation cannot be assessed using conventional tests. The Rekasius substitution solves this problem by replacing the transcendental term with its equivalent transfer function on the imaginary axis, Fig. 5.36. Assuming $\tau \in \mathcal{R}^+$, and the real number T ($T \in \mathcal{R}$) on the imaginary axis, following Rekasius substitution holds:

$$e^{-\tau s} = \frac{1 - Ts}{1 + Ts} \tag{5.56}$$

Thus, in the imaginary axis (i.e., $s = j\omega_c$), the transcendental term can be substituted with its exact equivalent term (5.56) without approximation. It should be noted that the system poles (i.e., roots of $\Delta(s,\tau)$) cross the imaginary axis when the system is going to become unstable, Fig. 5.36.

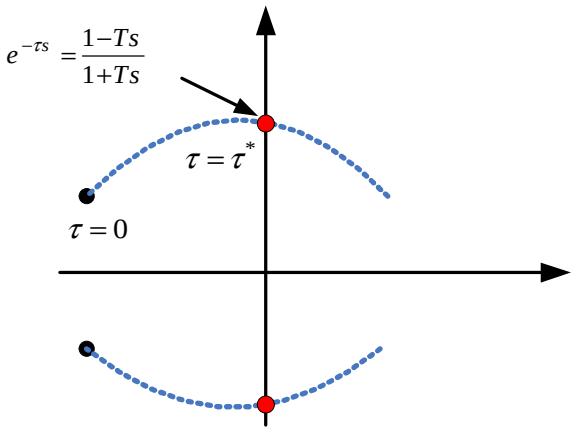

Figure 5.36 The Rekasius substitution.

The value of τ_i can be expressed in terms of ω_c and T as [109]:

$$\tau_i^* = \frac{2}{\omega_c}(tan^{-1}(\omega_c T) \pm i\pi), i = 0, 1, 2, 3, ... \tag{5.57}$$

Substituting (5.56) in (5.52), the characteristic equation in the imaginary axis can be obtained as:

$$\bar{\Delta}(s, \tau) = \sum_{k=0}^{n} a_k(s)(\frac{1 - Ts}{1 + Ts})^k \tag{5.58}$$

To find T which results in $\Delta(s, \tau) = 0$, both sides of the equation are multiplied by $(1+Ts)^n$ i.e.,

$$\bar{\Delta}(s, \tau) = \sum_{k=0}^{n} a_k(s)(1 - Ts)^k(1 + Ts)^{n-k} \tag{5.59}$$

The roots of $\bar{\Delta}(s, \tau)$, which only depend on T, should be investigated to conclude on the stability of the system. It should be noted that the transcendental characteristic equation with n^{th} degree (5.52) is now converted into $2n^{th}$ degree polynomial without transcendental term (5.59) with a similar purely imaginary roots.

To determine the stability of the system, several methods such as Routh's array and root sensitivity are addressed in [107, 109, 108]. However, these methods cannot be applied to high-order systems (e.g., a wind farm model) due to the complexity resulting from the uncertain parameter T. Therefore, the Guardian Map Theory [9] is adopted in this section to obtain the regions of stability.

The Guardian Map Theory is a practical and powerful analysis tool used to study uncertain systems [111]. To apply this technique, T is assumed to be an uncertain parameter.

Guardian Map Definition: Let $\mathcal{X}$ be the set of all polynomials with degree at most n and

real coefficients or the set of all $n \times n$ square real matrices, and let $\mathcal{S}$ be an open subset of $\mathcal{X}$ (a set is called open if all of its points have a neighborhood contained in the set). Moreover, assume that υ is a scalar valued function which maps $\mathcal{X}$ into the set of complex numbers $\mathcal{C}$. Let $\bar{\mathcal{S}}$ be the closure of $\mathcal{S}$ in $\mathcal{X}$ (the closure of a set is the union of its interior and its boundary). Then, we say υ guards $\mathcal{S}$ if, for all $x \in \bar{\mathcal{S}}$, the equivalence

$$\upsilon(x) = 0 \quad if\ and\ only\ if \quad x \in \partial\mathcal{S}, \tag{5.60}$$

holds. In this case, we can also say that υ is a guardian map for $\mathcal{S}$. $\partial\mathcal{S}$ denotes the boundary of the set $\mathcal{S}$ in $\mathcal{X}$. This definition and its subsequent proposition can be used to tackle the robust stability problem of a parameterized family of polynomials [9].

Proposition: Let $r = (r_1, r_2, ..., r_k) \in U$, where U is a pathwise connected subset of $\mathcal{R}^k$, and let $x(r)$ be a matrix or polynomial in $\mathcal{X}$ which depends continuously on the parameter vector r. Moreover, let $\mathcal{S} \subset \mathcal{X}$ be guarded by the map υ and assume that $x(r^0) \in \mathcal{S}$ for some $r^0 \in U$. Then,

$$x(r) \in \mathcal{S} \quad for\ all \quad r \in U \quad if\ and\ only\ if \quad \upsilon(x(r)) \neq 0 \quad for\ all \quad r \in U \tag{5.61}$$

For example, the determinant function $\upsilon : A \to \det(A)$ guards the set of nonsingular matrices $A_{n\times n}$. The set of Hurwitz-stable real polynomials of the form

$$P(s) = q_n s^n + q_{n-1}s^{n-1} + q_{n-2}s^{n-2} + ... + q_0 \tag{5.62}$$

is guarded by the map $\upsilon : P \to \det\mathbf{H}(P)$ where $\mathbf{H}(P)$ is the Hurwitz matrix associated with P and is given by

$$\mathbf{H}(P) = \begin{bmatrix} q_{n-1} & q_{n-3} & q_{n-5} & . & . & . & 0 \\ q_n & q_{n-2} & q_{n-4} & . & . & . & . \\ 0 & q_{n-1} & q_{n-3} & . & . & . & . \\ 0 & q_n & q_{n-2} & . & . & . & . \\ 0 & 0 & 0 & . & . & . & . \\ 0 & 0 & 0 & . & . & q_1 & 0 \\ 0 & 0 & 0 & . & . & q_2 & q_0 \end{bmatrix} \tag{5.63}$$

The guardian map analysis provides the value of T which causes instability. Then, both T and ω_c can be used to obtain τ_i^* using (5.57). Thus, τ^* can be expressed as:

$$\tau^* = \min(\tau_i^*) \tag{5.64}$$

It should be noted that the Guardian Map Theorem may provide several values of T such as $T_1, ..., T_j$. For each value of $T_l (1 \leq l \leq j)$, the characteristic equation (5.59) possesses one pair of imaginary roots with the real frequencies $\pm\omega_{cl}$, i.e., a one-to-one mapping exists between the T_l's and the positive frequencies ω_{cl}'s. The final value for τ^* should be selected as the smallest of the values of τ_i^* obtained from all of T_l and ω_{cl} using (5.57).

Table 5.4 The algorithm proposed for obtaining the stability delay margin.

Algorithm
- Calculate $\bar{\mathbf{A}}$ and $\bar{\mathbf{A}}_\tau$ using the state-space representation of system
- Obtain $\Delta(s, \tau)$ using (5.52)
- Obtain the characteristic polynomial $\bar{\Delta}(s, \tau)$ using the Rekasius substitution
- Use the guardian map theorem and obtain the determinant of the Hurwitz matrix (5.63)
- Calculate T_l's which result in the system instability
- Obtain ω_{cl} and τ_i^* for each value of T_l using the (5.59) and (5.57), respectively
- Find the minimum value of τ_i^*

Table 5.4 shows the algorithm of the proposed method, which obtains the delay margin of a system using the Rekasius substitution and Guardian Map Theorem. The delay margin sensitivity analysis is performed to illustrate the effects of power system parameters and wind farm operating conditions on the delay margin. Fig. 5.37 demonstrates the effects of the following factors on the stability delay margin: the wind speed, the RSC rise-time, the voltage regulation gain (K_v), the resistance, the reactance, and the capacitance.

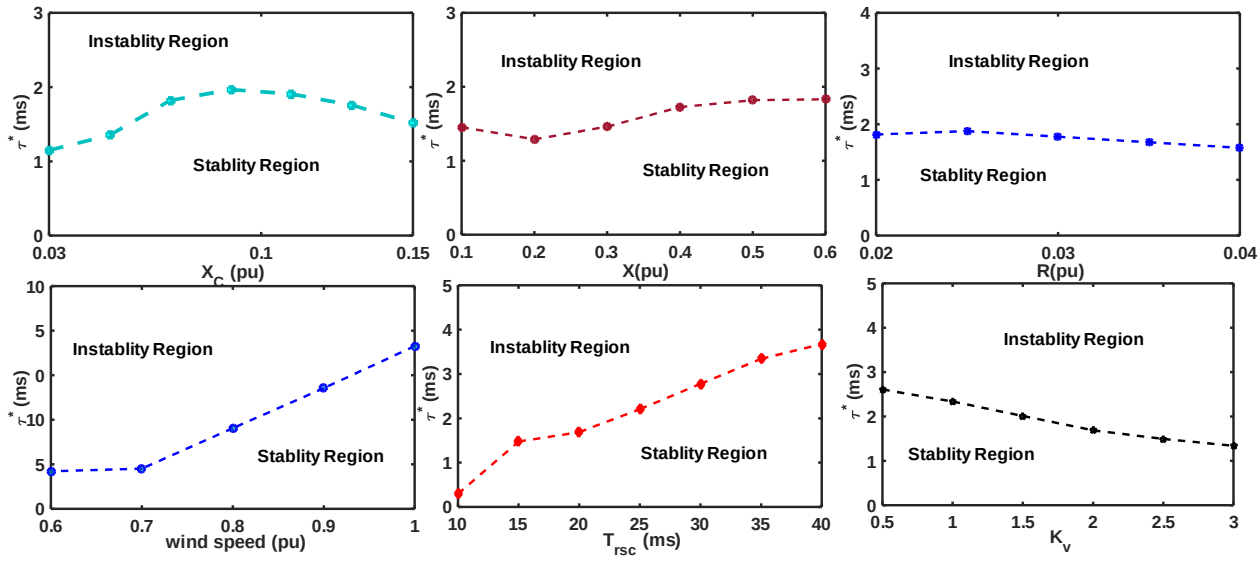

Figure 5.37 The impact of X_C, X, R, wind speed, T_{rsc} and K_v on the delay margin.

The results obtained from the EMT simulations illustrate that an increase in the wind speed or in the RSC rise-time result in an increase of the stability delay margin. However, the larger the voltage regulation gain, the smaller the stability delay margin. The resistance has a relatively negligible effect on the stability delay margin.

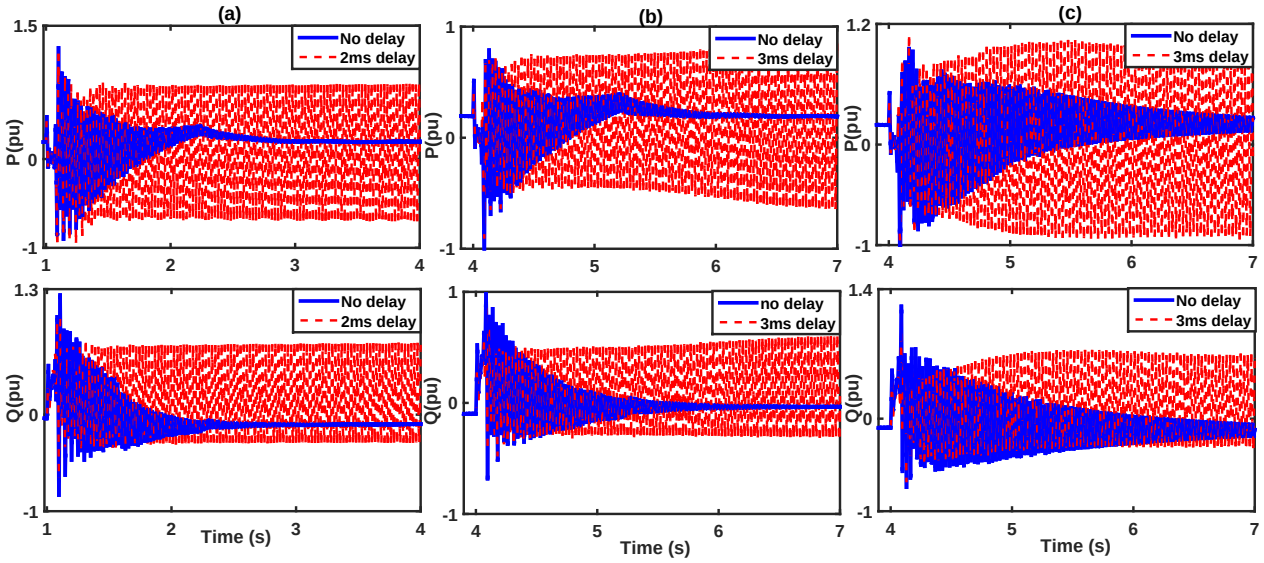

Figure 5.38 DFIG power components with and without delay for the multi-mode benchmark, (a) scenario a, (b) scenario b, and (c) scenario c.

The multi-mode benchmark with three different scenarios (described in Section. 3.11.3) is used as a case study. Fig. 5.38 shows the EMT simulation of scenario a, b and c, respectively. The DFIG active/reactive power components and its terminal voltage are illustrated in these figures. It can be observed that the delay, whose value is obtained from the analysis, can cause instability in the feedback loop.

Smith Predictor

To increase the delay margin, the Smith predictor scheme is adopted in this section [112, 113, 114]. The Smith predictor removes the transcendental term from the dominator of the closed-loop transfer function by using the difference between the model output and the plant output. Controller design can then proceed assuming no time-delay in the control loop.

The block diagram of a conventional time-delay system is represented in Fig. 5.39. In this figure, $\mathbf{y_p}$ is the measurement signal. It can be observed that the system can be split into a delay free system and a pure delay. If the variable $\mathbf{B}$ can be used in the feedback loop, since there is no delay in the feedback loop, the performance improves. However, it is not feasible

in a physical system to measure **B**. To alleviate this problem and improve the performance,

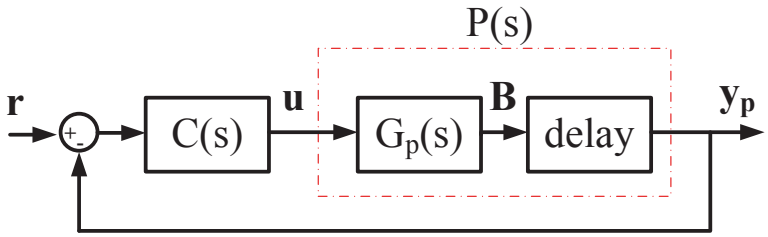

Figure 5.39 The feedback control of time delay system.

the Smith predictor scheme is used as demonstrated in Fig. 5.40. In this scheme, since the signal **B** is not available, the signal $\mathbf{B_m}$, which is the output of the mathematical model of the system, is used in the feedback loop. The **P** is the plant (which includes $\mathbf{G_p}(s)$ and the delay τ_p), $\mathbf{G_m}(s)$ is the mathematical model of the system, $\mathbf{C}(s)$ is the controller, $\mathbf{y_p}$ is the measurement signal, $\mathbf{y_1}$ is the output signal of the delayed mathematical model of the system, and $\mathbf{y_d}$ is the feedback signal.

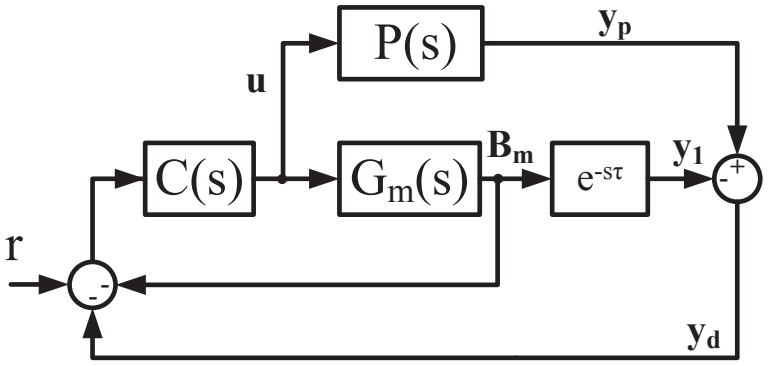

Figure 5.40 The rearrangement scheme of the Smith predictor.

Fig. 5.41 demonstrates the rearranged Smith predictor scheme. In this scheme, the closed-loop transfer function from **r** to $\mathbf{y_p}$ is:

$$\frac{\mathbf{y_p}}{\mathbf{r}} = \frac{C(s)G_p(s)e^{-s\tau_p}}{1 + CG_m(s) - CG_m(s)e^{-s\tau} + CG_p(s)e^{-s\tau_p}} \tag{5.65}$$

If $G_m(s) = G_p(s)$ and $\tau = \tau_p$, then this transfer function reduces to

$$\frac{\mathbf{y_p}}{\mathbf{r}} = \frac{C(s)G_p(s)e^{-s\tau_p}}{1 + CG_m(s)} \tag{5.66}$$

It can be observed that the transcendental term is removed from the dominator of the transfer

function.

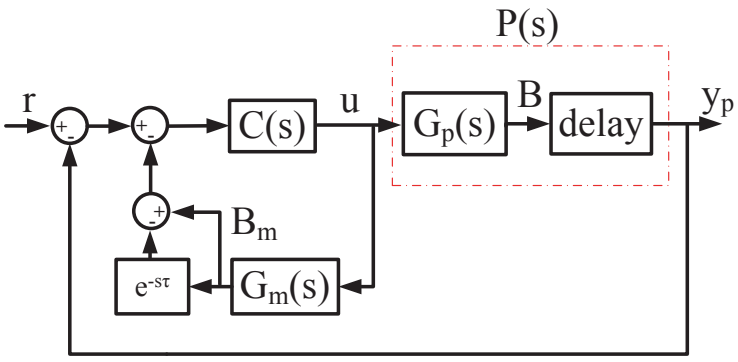

Figure 5.41 The scheme of adopted Smith predictor.

Fig. 5.42 shows the schematic diagram of the proposed predictor. In this scheme, **P** is the detailed realistic system (modeled in EMTP-RV software), $\mathbf{G}(s)$ is the linearized mathematical model of the system obtained in Chapter. 3, $\mathbf{C}(s)$ is the controller designed using the μ-synthesis technique, and $\mathbf{F}(s)$ is a low-pass filter used to ensure the stability of the Smith predictor. The behavior of the system against modeling uncertainty or unknown system delay can be modified using this filter [115, 116].

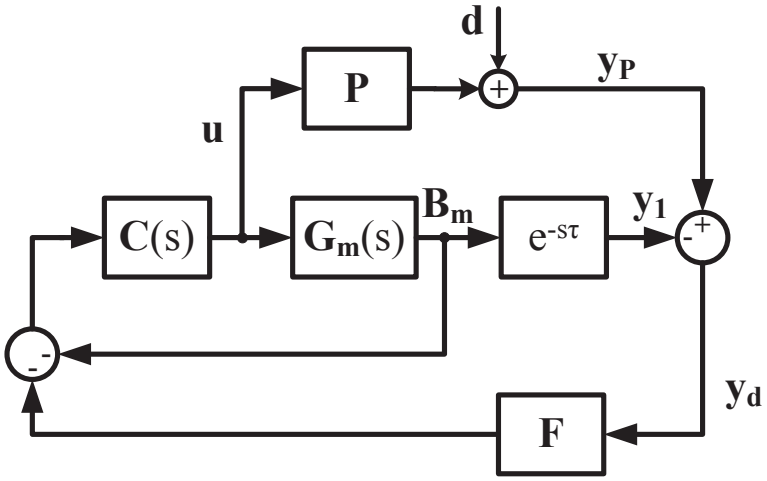

Figure 5.42 The scheme of the Smith predictor.

The main concern for the design of the low-pass filter is the system's ability to achieve the maximum possible delay margin considering plant uncertainty. To achieve this goal, the cut-off frequency and the gain of this low-pass filter are obtained using iterative EMT simulations. It should be noted that for obtaining a better performance, the designed filter should remove

the subsyncheronous frequencies from the feedback loop. The low-pass filter can be expressed as:

$$\mathbf{F}(s) = \begin{pmatrix} f & 0 & 0 & 0 \\ 0 & f & 0 & 0 \\ 0 & 0 & f & 0 \\ 0 & 0 & 0 & f \end{pmatrix} \qquad f = \frac{5}{(s + 2\pi(20))} \tag{5.67}$$

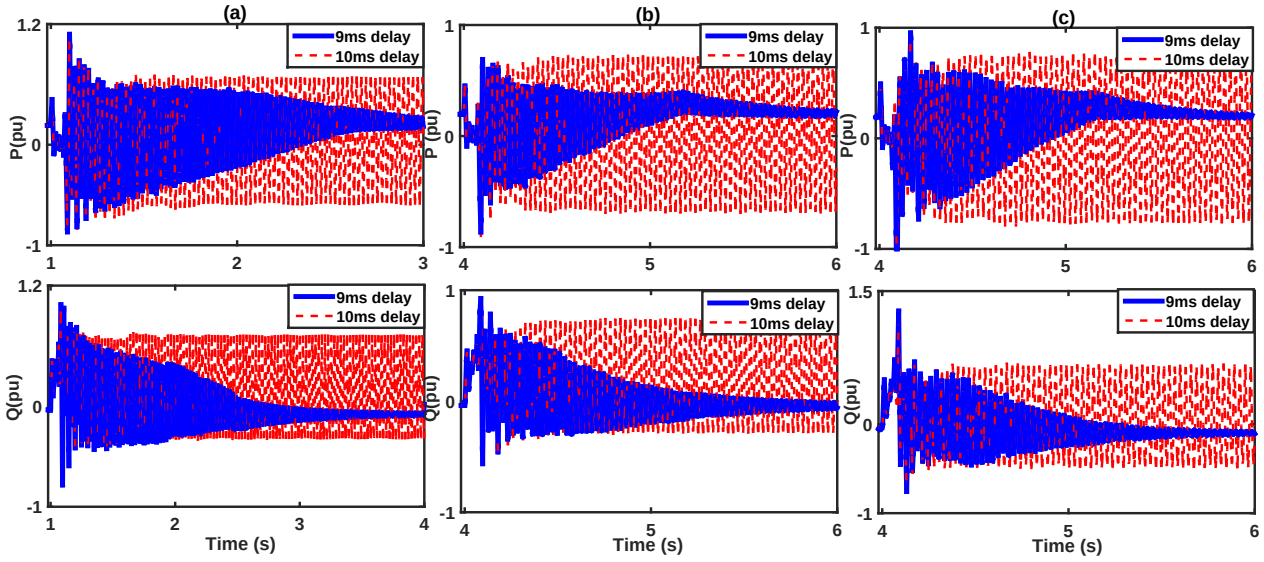

Figure 5.43 The active/reactive power components of the DFIG using the Smith predictor (a) scenario a, (b) scenario b, and (c) scenario c.

The EMT simulations are performed to show the effectiveness of the proposed prediction scheme. The injected power components of the DFIG are shown in Fig. 5.43. It can be observed that the Smith predictor can increase the delay stability margin of the system to 9 ms.

5.5 Sensor Failure

The performance and stability of a control system can be lost due to sensor failure. Therefore, model-based fault detection and isolation (FDI) techniques are attracting considerable attention [117]. The main goal of model-based FDI is to design a fault tolerant control system (FTCS) which is able to maintain system stability and performance after a sensor failure. The FDI scheme is demonstrated in Fig. 5.44. In this figure, asterisk superscript (*) denotes a faulty measurement.

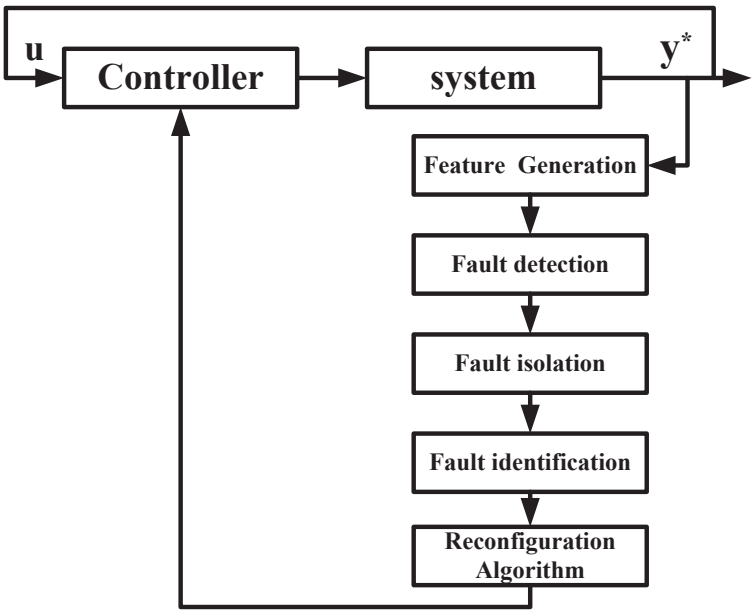

Figure 5.44 The FDI scheme.

This scheme consists of feature generation, fault detection, failure isolation, failure identification, and control system reconfiguration functions [118] detailed as follows.

1. Feature generation is the calculation of signals required to detect the failure.
2. Failure detection is the procedure of detecting whether the sensor failure occurred or not.
3. Failure isolation is the procedure of finding the location of the failure.
4. Failure identification function determines the type, magnitude and cause of the failure.
5. Control system reconfiguration function changes the structure of the controller so that the system remains stable following the failure.

There are several fault detection and identification techniques which have been addressed in [8]. Among these techniques, the observer-based residue generation method is the most well-known one [119, 120]. This method computes the measurement signals of a system using the mathematical model of the system and compares them with the actual measurement signals. A significant difference between these signals reveals a sensor failure. The main challenge regarding this technique is achieving robustness against system uncertainties or large disturbances (e.g., electrical faults), and sensor failure as both result in a sudden and abrupt change in the measurement signals. Fig. 5.45 shows the scheme of the residue generation technique. In this section, we employ this technique to detect sensor failure, and use the obtained result to change the structure of the damping controller to ensure system stability

during subsynchronous phenomenon.

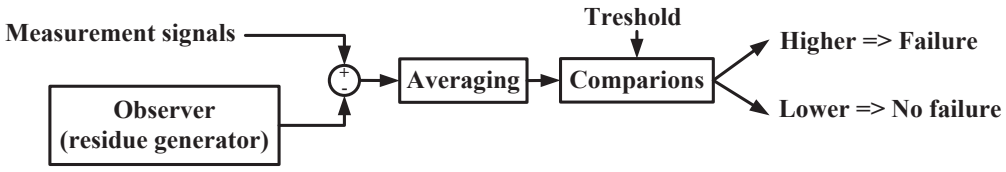

Figure 5.45 The general scheme of the residue generation technique.

The controllers of the wind farms are vulnerable to sensor failure. This phenomena accounts for 14.1% of the total number of failures in the wind farm and causes 5.4% of the total downtime [121]. The transient behavior of the system and its stability may be affected by sensor failure particularly when the possibility of the SSI phenomenon exists. Therefore, continuous monitoring of the system for sensor failure detection seems to be inevitable. Moreover, following a failure in the sensors, the SSI damping controller needs to be restructured to ensure safe operation of the system and to prevent unstable subsynchronous oscillations. In this section, we propose a framework for fault identification, detection, isolation, and controller reconfiguration for a DFIG-based wind farm subjected to SSI. The proposed framework uses the linear matrix inequality (LMI) technique to design a robust residue generator. This robust residue generator is used to obtain the estimated value of the measurement signals which are the system states in our design, i.e., the currents of the RSC and the GSC. The designed observer employs the quadratic stability method to ensure its stability following power system impedance variations which may occur due to electrical faults.

As discussed before, in the residue generation method, an abrupt change in the difference between the residue and the measurement signals reveals a sensor failure. The detection of an abrupt change in a signal can be carried out using several techniques. The simplest and most widely used technique is the usage of an averaging block and a threshold. The averaging block removes the impact of noise and small variations of operating point, and the threshold determines whether a signal shows meaningful variations.

Since the currents of the RSC and GSC (i.e., the measurement signals) are state-variables of the system, a full-order state observer can be used to calculate the currents of the converters. The main challenges of using this approach are the uncertainty of the power system and large disturbances, particularly electrical faults. These faults may result in the malfunctioning of the failure detection algorithm. Therefore, the designed observer should be robust against uncertainties in the power system and estimate the states rapidly.

The family of uncertain systems with interval parametric uncertainty in the impedance of

the power system (i.e., R, X, and X_C) can be represented as:

$$\begin{aligned} \dot{\mathbf{x}} &= \mathbf{A}(\zeta)\mathbf{x} + \mathbf{B}\mathbf{u} \\ \mathbf{y} &= \mathbf{C}\mathbf{x} \end{aligned} \tag{5.68}$$

where ζ is the uncertain parameter ($\zeta \in [\zeta^-, \zeta^+]$). Let $\mathbf{\Delta}_I$ be the set of the all possible edges of the uncertainty space as detailed below:

$$\mathbf{\Delta}_I = \{\zeta = (\zeta_1, \zeta_2, ..., \zeta_k) | \zeta_i = \zeta_i^- or \zeta_i^+, i = 1, 2, ..., k\} \tag{5.69}$$

Generally speaking, the dynamics of the observer can be expressed as [93]:

$$\dot{\mathbf{e}} = (\mathbf{A} - \mathbf{L}\mathbf{C})\mathbf{e} \tag{5.70}$$

where $\mathbf{e}$ is the error signal ($\mathbf{e} = \mathbf{x} - \hat{\mathbf{x}}$), $\mathbf{x}$ is the state vector and $\hat{\mathbf{x}}$ is the vector of the observed states. The observer can be designed by obtaining the gain matrix $\mathbf{L}$. The main goals of the observer design are: (1) observer should remain stable considering the uncertainty $\mathbf{\Delta}_I$ (i.e., $(\mathbf{A}(\zeta) - \mathbf{L}\mathbf{C})$ be Hurwitz), (2) observer should estimate the states as fast as possible (i.e., eigenvalues of error should be moved toward the left of the s-plane $Re(s) \leq \alpha$). It should be noted that system modes move almost horizontally in the s-plane. Therefore, the desired area satisfies the second goal of the observer design. The gain matrix of the quadratic stable observer can be obtained using a positive-definite matrix P and matrix W satisfying the following Lyapunov equations:

$$\begin{aligned} \mathbf{A}^T(\zeta)\mathbf{P} + \mathbf{P}\mathbf{A}(\zeta) + \mathbf{C}^T\mathbf{W} + \mathbf{W}^T\mathbf{C} + 2\alpha\mathbf{P} < 0 \\ \mathbf{P} > 0 \\ \forall \zeta \in \Delta_I \end{aligned} \tag{5.71}$$

where $\mathbf{P}$ and $\mathbf{W}$ are the solutions of (5.71). Then,

$$\mathbf{L} = \mathbf{W}\mathbf{P}^-1 \tag{5.72}$$

Parameter α, which indicates the fastness of the observer, is obtained to be -4 using repetitive EMT simulations. It should be noted that very fast observers may deteriorate the transient behavior of the system or result in an infeasible solution for (5.71).

The proposed framework for the sensor failure detection is shown in Fig. 5.46. In the residue analysis block, failures and faulty sensors are detected using the threshold value. Proper detection of a faulty sensor (or equivalently the detection of an abrupt change in residue)

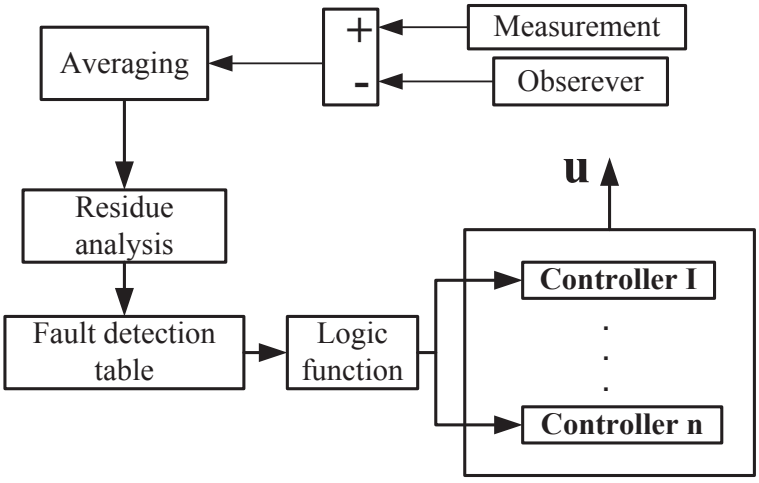

Figure 5.46 The proposed framework for sensor fault tolerant control.

requires the selection of an averaging frequency and a threshold value. Fig. 5.47 demonstrates the residue signal following a failure in the q-axis of the GSC current sensors at $t = 3\ s$. The multi-mode benchmark, whose SSCI oscillations are mitigated using the μ-synthesis technique, is adopted as a case study here. This figure illustrates the effect of the averaging frequency and the importance of threshold (η) selection in the proposed procedure. A low averaging frequency results in smoother residue waveform and consequently late sensor failure detection for 1 second. A high averaging frequency results in the fast detection of failures. However, the residue signal will fluctuate during the power system faults and the detection algorithm may mistake a power system fault for a sensor failure. This dilemma can be solved by the proper selection of the η considering the most severe electrical faults, i.e., three-phase metallic fault at the POI of the wind farm. It should also be noted that a large value of α in (5.71) results in a higher magnitude of residue following an electrical fault when the averaging frequency is high. Therefore, the selected value for α can also be adjusted in this step if the speed of detection is low.

The fault detection table in Fig. 5.46 is used to obtain the number of faulty sensors and to determine which controller should be switched into the control system by the logic function, Fig. 5.46. Following a sensor failure and its detection, the structure of the controller should change to guarantee the stability of the system. Such control scheme rearrangements are necessary to deal with losses of accurate measurement signals. To avoid an undesirable transient response and instability, a bank of controllers consisting of $2^z - 1$ separate controllers, where z is the number of measurement sensors, are designed considering all possible scenarios of measurement sensor loss. As an example, if the fault detection function shows a sensor failure

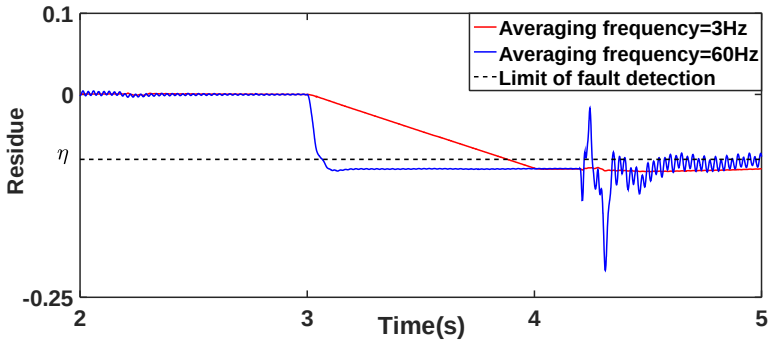

Figure 5.47 The obtained residue following a fault in the GSC q-axis current sensor.

in the q-axis current of the GSC, this sensor is removed from the feedback scheme and the number of input and output channels of the controller is reduced to 3. It is also assumed that if all of the sensors become faulty, the fault detection function disconnects the wind farm from the power system. It should be noted that the stabilizing controllers may not always be available if the disregarding of a measurement sensor results in an uncontrollable system.

Fig. 5.48 and Fig. 5.49 show the DFIG terminal voltage in scenario b (detailed in Section. 3.11.3) when the controller remains unchanged following a sensor failure. In these figures, the RSC and GSC measurements have 20% additive sensor failure. It can be observed that these failures result in sluggish and unstable transient response of the system. In Fig. 5.48, the crowbar activates repetitively due to voltage fluctuations and in Fig. 5.49 the subsynchronous oscillations remain undamped.

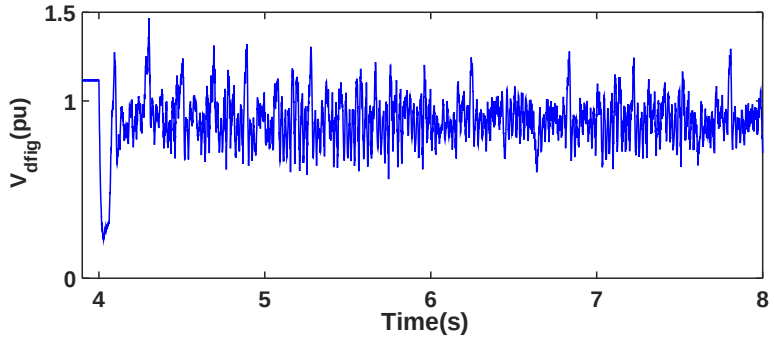

Figure 5.48 V_{dfig} considering 20% additive fault in GSC current sensors, scenario b.

The EMT simulations of the detailed system are used to validate the proposed framework. Fig. 5.50 shows the DFIG active/reactive power components and its terminal voltage for scenarios a and b of the multi-mode benchmark. It is assumed that during the normal operation of the system at $t = 3\ s$, the dq-axis GSC current sensors become faulty. The proposed

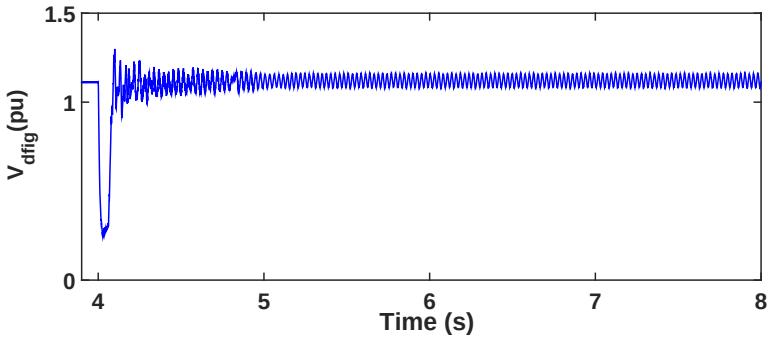

Figure 5.49 V_{dfig} considering 20% additive fault in RSC current sensors, scenario b.

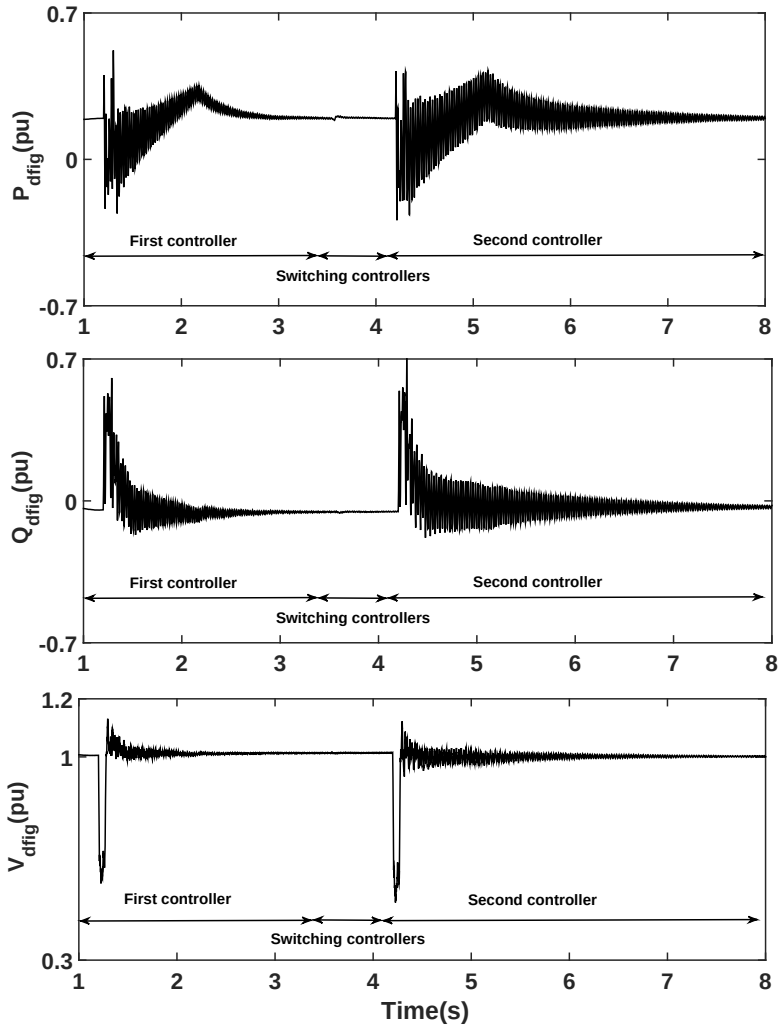

Figure 5.50 P(pu), Q(pu) and V(pu) of the DFIG with proposed framework (scenarios a and b).

framework is able to successfully damp the oscillation without deterioration of the transient behavior.

5.6 Summary

This chapter proposes several supplementary SSCI damping controllers designed using the LQR, the mixed-sensitivity H^∞ and the μ-synthesis techniques to mitigate subsynchronous oscillations. Certain implementation challenges for the proposed controllers are addressed.

The LQR technique is used for the single-mode aggregated benchmark. Then, different restriction schemes and local/central implementations of the designed controller are investigated. The LQR technique gives a simple control scheme. However, more complex controllers may be required depending on the system topology and control objectives.

A mixed-sensitivity H^∞ controller is also proposed in this chapter. This method enables the designer to impose several performance objectives such as disturbance rejection and noise attenuation at once. The effectiveness of the H^∞ controller and the accuracy of the aggregation methods are verified through EMT simulations on the detailed single-mode benchmark.

The μ-synthesis technique is used to design a controller for the mitigation of SSCI oscillations in the presence of parametric uncertainty in the impedances of the power system. The proposed controller is used to damp the oscillations in the multi-mode benchmark. The μ-synthesis technique may give high order controllers depending on the ranges of the uncertainties. The SSCI damping controller should be designed on the basis of the system topology, the desired control objectives and the required simplicity.

The impact of time-delay on the subsynchronous stability of the system is addressed. The Rekasius substitution and the Guardian Map theory are used to calculate the delay margin for a DFIG-based wind farm whose oscillations are mitigated by the μ-synthesis technique. The impacts of power system parameters and wind farm operating conditions on the delay margin are examined using a sensitivity analysis. The Smith predictor scheme is proposed to extend the delay margin.

A framework for the detection of sensor failure in a DFIG-based wind farm is also proposed in this chapter. This framework employs a residue generation technique to detect sensor failure and restructure the SSCI damping controller. The main advantages of this framework are its ability to distinguish between electrical faults and sensor failures, and ensure the subsynchronous stability of the system following a failure in the measurement sensors.

CHAPTER 6 CONCLUSION

6.1 Thesis Summary

This thesis applies several methods to analyze and mitigate the subsynchronous oscillations created in a doubly-fed induction generator (DFIG)-based wind farm connected to a series compensated transmission line.

Chapter 3 focuses on the modeling of a wind farm, its state-space representation, and developing the benchmarks. The first step in the analysis and mitigation of subsynchronous phenomena is obtaining a mathematical model which describes the system characteristics. This mathematical model and the state-space representation of the system are obtained, and a detailed model of the system is developed in EMTP-RV software for time domain simulations. Using the model developed in EMTP-RV software, several benchmarks are introduced based on realistic power systems including the DFIG-based wind farm. According to existing standards, the transient behavior of the overall power system should meet the grid code requirements [83]. Thus, modeling of the power system, wind farm, and wind turbines should be performed precisely while considering the details of the electrical and control systems. The fault-ride-through (FRT) and the nonlinearities in the control system (e.g., saturation units) and electrical circuits are considered in the detailed modeling. The wind farm secondary controller (WFC), the collector grid and non-homogeneous wind speed are also considered in our studies. This step paves the way for more accurate and detailed analysis of subsynchronous phenomena. In this thesis, the transient responses of the developed benchmarks, including the performance evaluation of the proposed controllers, are demonstrated using EMTP-RV simulations.

The analysis of subsynchronous phenomena using the established methods are carried out in Chapter 4. The different types of subsynchronous phenomena are briefly studied and discussed. The techniques of eigenvalue analysis, and the frequency scan method together with EMT simulation are used to analyze the SSI phenomenon. This chapter also presents a comprehensive robust stability analysis to evaluate the effect of system uncertainties, e.g., line impedance and wind farm control parameters, on the loci of the SSI mode. The results are used to obtain some guidelines for the safe operation of the DFIG-based wind farm. In these guidelines, the impacts of different power system parameters and wind farm operating conditions are discussed.

The mitigation of SSCI oscillations using a supplementary damping controller is addressed

in Chapter 5. The designed supplementary damping controller is added to the control system of the wind farm. Several techniques are used to design various controllers depending on the power system topology and structure. All the proposed controllers use the currents of the DFIGs as their inputs and inject the produced output signals into the inner control loops of the RSC and GSC. These output signals are limited dynamically according to the DFIG converter limits and the desired transient response against the faults. The SSCI damping controller is designed based on the linear model of the system. However, the effectiveness of the supplementary controllers is verified using the detailed wind farm models and benchmarks developed in Chapter 3. The EMTP-RV simulations demonstrate that the proposed controllers successfully damp the SSCI oscillations without deteriorating the DFIG transient response. The following techniques are used to design the proposed controllers:

6.1.1 LQR Controller

This SSCI damping controller consists of an observer, and a full-state feedback gain designed based on the LQR technique. The Lyapunov and LQR techniques are used to design the observer gain. The single-mode benchmark is used to verify the effectiveness of this controller.

Initially, the designed controller is placed in the secondary control layer of the wind farm; this arrangement is named "central implementation". The transient response of the system turns out to be unsatisfactory in the face of large changes in the system structure such as turbine or feeder outages. The poor response against changes in system structure is attributable to the fixed structure of the controller. Therefore, a gain-scheduling control scheme is proposed to obviate such undesirable transient responses. Moreover, to achieve a simple control structure, the proposed controllers are placed in the control circuits of each turbine; this arrangement is named "local implementation". Simulation results establish the superiority of local over central implementation with respect to the ability to damp the SSCI oscillations.

6.1.2 H^∞ Controller Design

Based on the mixed-sensitivity and pole placement techniques, the H^∞ control is used to design a supplementary damping controller. In the EMT simulations, certain parts of the wind farm are modeled to include the medium voltage (MV) collector grid. In those parts, the wind speeds are modeled as having Gaussian distributions. The simulation results confirm that the aggregated model provides an acceptable level of accuracy which is comparable to what can be achieved by using the detailed model of the wind farm.

6.1.3 μ-Controller

Based on the μ-synthesis technique, a supplementary SSI damping controller is designed to mitigate subsynchronous oscillations. This type of controller is well-suited for widely uncertain systems. The linearized model is also used to analyze the system robustness. The multi-mode benchmark is implemented in the EMTP-RV software to verify the impact of uncertainty on the performance of the proposed μ-controller.

The impact of time delay on the system stability when the SSCI damping controller is implemented in the secondary control level is also discussed in Chapter. 5. The delay margin of the system is calculated using the modified Rekasius substitution technique and the Guardian Map Theory to better deal with the systems which have high order models. Then, the impact of power system parameters and wind farm operating condition on the delay margin is obtained. To improve the system response in the presence of delay, a Smith Predictor scheme is proposed. Chapter 5 also proposes a new framework for detecting the failure of the sensors that provide the inputs to the SSCI damping controller. Such faulty sensors result in system instability or unacceptable transient behavior when the system is subjected to SSCI. The proposed framework uses the residue generation technique to detect the failure and switch the controller in a gain-scheduling scheme to preserve the stability of the system.

6.2 Publications

1- M. Ghafouri, U. Karaagac, H. Karimi, S. Jensen, J. Mahseredjian, and S. O. Faried, "An LQR Controller for Damping of Subsynchronous Interaction in DFIG-Based Wind Farms," IEEE Transactions on Power Systems, February 2017, doi :10.1109/TPWRS.2017.2669260.

2- M. Ghafouri, U. Karaagac, H. Karimi, and J. Mahseredjian, "A Robust Controller for Mitigating Subsynchronous Interaction in DFIG-based Wind Farms," under preparation.

3- M. Ghafouri, U. Karaagac, H. Karimi, and J. Mahseredjian, "Local Implementation of SSCI Damping Controller," under preparation.

4- M. Ghafouri, U. Karaagac, and H. Karimi, "A Practicable H^{∞}-based SSCI Damping Controller for Series Compensated Wind Farms with DFIG Wind Turbines," submitted to IET Journal of Renewable Energies.

5- M. Ghafouri, U. Karaagac, H. Karimi, and J. Mahseredjian, "Subsynchronous resonance damping in DFIG-based wind farms using optimal control," 2016 IEEE Power and Energy Society General Meeting (PESGM), Boston, MA, 2016, pp. 1-5.

6.3 Future Works

The following topics are suggested for future research in continuation of this work:

1. SSCI analysis and mitigation considering unbalanced conditions, e.g., unbalanced fault and voltages: In the literature, analysis and mitigation of subsynchronous phenomenon is performed when the wind farm is connected to three-phase balanced voltage. Moreover, subsynchronous phenomena occurs following a three-phase to ground symmetric fault. However, the problem remains unsolved considering unbalanced voltage or asymmetrical faults in the power system. In this case, the decoupled sequence control of the DFIG should be considered. It should also be noted that the phase imbalance is a countermeasure against SSCI. Moreover, components such as measurement filters should be added to the control circuit as those components may have significant impact on the subsynchronous stability of the system.
2. Subsynchronous study of the power system including the voltage source converter (VSC)-based components: Recently, the penetration level of the VSC-based components in power systems has increased due to their applications in the generation and transmission of electricity. However, VSC-based components may cause subsynchronous interaction in a grid, particularly the torsional interaction. These interactions often occur between the control circuit of a VSC-based component and other generation units. The HVDC system and the photovoltaic (PV) system are instances of VSC-based components that have received considerable attention due to recent incidents in China [122, 123]. The interaction between a turbo-generator and a VSC-HVDC system is discussed in [124]. The identification and mitigation of such interactions are challenging problems demanding further research.
3. Achieving SSCI mitigation by redesigning the inner control loops of the DFIG controller: As discussed in Chapter 4, the main reason for the occurrence of the subsynchronous phenomenon is the fast reaction of the DFIG control system. The safe operating region may be enlarged by redesigning the inner control loops of the RSC and the GSC using a new multiple-input multiple-output (MIMO) control scheme and considering the current reference signals of both converters as input vector of the new inner loop controller. This idea is adopted in the literature to damp the inter-area oscillations in power systems in the presence of FACTS devices. However, there are several challenges regarding the employment of this idea in DFIG-based wind farms. One challenge is the transient response of the controller against different types of faults. Moreover, the design procedure of the controller should be straightforward and simple enough for industrial applications.

BIBLIOGRAPHY

[1] Global wind report annual market update 2013,. [Online]. Available : http://www.iea.org

[2] Renewables 2017 global status report. [Online]. Available : http://www.ren21.net

[3] Global wind report annual market statistics,2016. [Online]. Available : http://www.GWEC.net

[4] [Online]. Available : http://www.canwea.ca

[5] "Terms, definitions and symbols for subsynchronous oscillations," *Power Apparatus and Systems, IEEE Transactions on*, vol. PAS-104, no. 6, pp. 1326–1334, June 1985.

[6] "Proposed terms and definitions for subsynchronous oscillations," *Power Apparatus and Systems, IEEE Transactions on*, vol. PAS-99, no. 2, pp. 506–511, March 1980.

[7] M. Sahni, D. Muthumuni, B. Badrzadeh, A. Gole, and A. Kulkarni, "Advanced screening techniques for sub-synchronous interaction in wind farms," in *PES T D 2012*, May 2012, pp. 1–9.

[8] Y. Zhang and J. Jiang, "Bibliographical review on reconfigurable fault-tolerant control systems," *Annual Reviews in Control*, vol. 32, no. 2, pp. 229 – 252, 2008. [Online]. Available : http://www.sciencedirect.com/science/article/pii/S1367578808000345

[9] L. Saydy, A. L. Tits, and E. H. Abed, "Guardian maps and the generalized stability of parametrized families of matrices and polynomials," *Mathematics of Control, Signals and Systems*, vol. 3, no. 4, pp. 345–371, 1990. [Online]. Available : http://dx.doi.org/10.1007/BF02551375

[10] H. Wu, K. S. Tsakalis, and G. T. Heydt, "Evaluation of time delay effects to wide-area power system stabilizer design," *IEEE Transactions on Power Systems*, vol. 19, no. 4, pp. 1935–1941, Nov 2004.

[11] S. Purushothaman and F. D. Leon, "Eliminating sub-synchronous oscillations with an induction machine damping unit (IMDU)," in *2011 IEEE Power and Energy Society General Meeting*, July 2011, pp. 1–1.

[12] D. N. Walker, C. E. J. Bowler, R. L. Jackson, and D. A. Hodges, "Results of subsynchronous resonance test at mohave," *IEEE Transactions on Power Apparatus and Systems*, vol. 94, no. 5, pp. 1878–1889, Sept 1975.

[13] D. H. Baker, G. E. Boukarim, R. D'Aquila, and R. J. Piwko, "Subsynchronous resonance studies and mitigation methods for series capacitor applications," in *2005 IEEE*

Power Engineering Society Inaugural Conference and Exposition in Africa, July 2005, pp. 386–392.

[14] G. D. Irwin, A. K. Jindal, and A. L. Isaacs, "Sub-synchronous control interactions between type 3 wind turbines and series compensated AC transmission systems," in *2011 IEEE Power and Energy Society General Meeting*, July 2011, pp. 1–6.

[15] L. Fan, C. Zhu, Z. Miao, and M. Hu, "Modal analysis of a DFIG-based wind farm interfaced with a series compensated network," *Energy Conversion, IEEE Transactions on*, vol. 26, no. 4, pp. 1010–1020, Dec 2011.

[16] Y. Cheng, S. H. Huang, J. Rose, V. A. Pappu, and J. Conto, "ERCOT subsynchronous resonance topology and frequency scan tool development," in *2016 IEEE Power and Energy Society General Meeting (PESGM)*, July 2016, pp. 1–5.

[17] H. A. Mohammadpour and E. Santi, "Analysis of subsynchronous control interactions in DFIG -based wind farms : ERCOT case study," in *2015 IEEE Energy Conversion Congress and Exposition (ECCE)*, Sept 2015, pp. 500–505.

[18] J. Adams, V. A. Pappu, and A. Dixit, "ERCOT experience screening for sub-synchronous control interaction in the vicinity of series capacitor banks," in *2012 IEEE Power and Energy Society General Meeting*, July 2012, pp. 1–5.

[19] M. Sahni, B. Badrzadeh, D. Muthumuni, Y. Cheng, H. Yin, S. H. Huang, and Y. Zhou, "Sub-synchronous interaction in wind power plants- part ii : An ERCOT case study," in *2012 IEEE Power and Energy Society General Meeting*, July 2012, pp. 1–9.

[20] B. Badrzadeh, M. Sahni, Y. Zhou, D. Muthumuni, and A. Gole, "General methodology for analysis of sub-synchronous interaction in wind power plants," *Power Systems, IEEE Transactions on*, vol. 28, no. 2, pp. 1858–1869, May 2013.

[21] Y. Cheng, S. H. Huang, J. Rose, V. A. Pappu, and J. Conto, "ERCOT subsynchronous resonance topology and frequency scan tool development," in *2016 IEEE Power and Energy Society General Meeting (PESGM)*, July 2016, pp. 1–5.

[22] M. El-Marsafawy, "Use of frequency-scan techniques for subsynchronous-resonance analysis of a practical series-capacitor compensated AC network," *IEE Proceedings C - Generation, Transmission and Distribution*, vol. 130, no. 1, pp. 28–40, January 1983.

[23] M. Elfayoumy and C. Moran, "A comprehensive approach for subsynchronous resonance screening analysis using frequency scanning technique," in *Power Tech Conference Proceedings, 2003 IEEE Bologna*, vol. 2, June 2003, p. 5 pp. Vol.2.

[24] Y. Cheng, M. Sahni, D. Muthumuni, and B. Badrzadeh, "Reactance scan crossover-based approach for investigating SSCI concerns for DFIG-based wind turbines," *IEEE Transactions on Power Delivery*, vol. 28, no. 2, pp. 742–751, April 2013.

[25] N. Johansson, L. Angquist, and H. P. Nee, "A comparison of different frequency scanning methods for study of subsynchronous resonance," *IEEE Transactions on Power Systems*, vol. 26, no. 1, pp. 356–363, Feb 2011.

[26] W. Ren and E. Larsen, "A refined frequency scan approach to sub-synchronous control interaction (SSCI) study of wind farms," *IEEE Transactions on Power Systems*, vol. 31, no. 5, pp. 3904–3912, Sept 2016.

[27] U. Karaagac, J. Mahseredjian, S. Jensen, R. Gagnon, M. Fecteau, and I. Kocar, "Safe operation of DFIG based wind parks in series compensated systems," *IEEE Transactions on Power Delivery*, vol. PP, no. 99, pp. 1–1, 2017.

[28] M. S. Annakkage, C. Karawita, and U. D. Annakkage, "Frequency scan-based screening method for device dependent sub-synchronous oscillations," *IEEE Transactions on Power Systems*, vol. 31, no. 3, pp. 1872–1878, May 2016.

[29] L. Fan and Z. Miao, "Mitigating SSR using DFIG-based wind generation," *Sustainable Energy, IEEE Transactions on*, vol. 3, no. 3, pp. 349–358, July 2012.

[30] L. Fan, R. Kavasseri, Z. L. Miao, and C. Zhu, "Modeling of DFIG -based wind farms for SSR analysis," *Power Delivery, IEEE Transactions on*, vol. 25, no. 4, pp. 2073–2082, Oct 2010.

[31] L. Fan, C. Zhu, Z. Miao, and M. Hu, "Modal analysis of a DFIG-based wind farm interfaced with a series compensated network," *Energy Conversion, IEEE Transactions on*, vol. 26, no. 4, pp. 1010–1020, Dec 2011.

[32] C. Z. Zaijun Wu and M. Hu, "Supplementary controller design for SSR damping in a series-compensated DFIG-based wind farm," in *Energies Journal*, vol. 5, November 2012, pp. 4481–4496.

[33] J. Sun, "Small-signal methods for AC distributed power systems ; a review," *Power Electronics, IEEE Transactions on*, vol. 24, no. 11, pp. 2545–2554, Nov 2009.

[34] J. Sun and Z. Miao, "Impedance-based stability criterion for grid-connected inverters," *Power Electronics, IEEE Transactions on*, vol. 26, no. 11, pp. 3075–3078, Nov 2011.

[35] L. Piyasinghe, Z. Miao, J. Khazaei, and L. Fan, "Impedance model-based SSR analysis for TCSC compensated type-3 wind energy delivery systems," *Sustainable Energy, IEEE Transactions on*, vol. 6, no. 1, pp. 179–187, Jan 2015.

[36] I. Vieto and J. Sun, "Real-time simulation of subsynchronous resonance in type-III wind turbines," in *Control and Modeling for Power Electronics (COMPEL), 2014 IEEE 15th Workshop on*, June 2014, pp. 1–8.

[37] Z. Miao, "Impedance-model-based SSR analysis for type 3 wind generator and series-compensated network," *Energy Conversion, IEEE Transactions on*, vol. 27, no. 4, pp. 984–991, Dec 2012.

[38] L. Piyasinghe, Z. Miao, J. Khazaei, and L. Fan, "Impedance model-based SSR analysis for TCSC compensated type-3 wind energy delivery systems," *Sustainable Energy, IEEE Transactions on*, vol. 6, no. 1, pp. 179–187, Jan 2015.

[39] G. Cakir, G. Radman, and K. Hatipoglu, "Determination of the best location and performance analysis of statcom for damping oscillation," in *Southeastcon, 2013 Proceedings of IEEE*, April 2013, pp. 1–5.

[40] A. Jalilvand and M. Keshavarzi, "Adaptive SVC damping controller design, using residue method in a multi-machine system," in *Electrical Engineering/Electronics, Computer, Telecommunications and Information Technology, 2009. ECTI-CON 2009. 6th International Conference on*, vol. 01, May 2009, pp. 160–163.

[41] H. Mohammadpour and E. Santi, "SSR damping controller design and optimal placement in rotor-side and grid-side converters of series-compensated DFIG-based wind farm," *Sustainable Energy, IEEE Transactions on*, vol. 6, no. 2, pp. 388–399, April 2015.

[42] A. Leon and J. Solsona, "Sub-synchronous interaction damping control for DFIG wind turbines," *Power Systems, IEEE Transactions on*, vol. 30, no. 1, pp. 419–428, Jan 2015.

[43] W. Zhu, R. Spee, R. Mohler, G. Alexander, W. Mittelstadt, and D. Maratukulam, "An EMTP study of SSR mitigation using the thyristor controlled series capacitor," *Power Delivery, IEEE Transactions on*, vol. 10, no. 3, pp. 1479–1485, Jul 1995.

[44] U. Karaagac, S. Faried, J. Mahseredjian, and A. A. Edris, "Coordinated control of wind energy conversion systems for mitigating subsynchronous interaction in dfig-based wind farms," *Smart Grid, IEEE Transactions on*, vol. 5, no. 5, pp. 2440–2449, Sept 2014.

[45] S. F. X. Gao, U. Karaagac and J. Mahseredjian, "On the use of wind energy conversion systems for mitigating subsynchronous resonance and subsynchronous interaction," in *Innovative Smart Grid Technologies Conference Europe (ISGT-Europe), 2014 IEEE PES*, Oct 2014, pp. 1–6.

[46] H. A. Mohammadpour and E. Santi, "Modeling and control of gate-controlled series capacitor interfaced with a DFIG-based wind farm," *IEEE Transactions on Industrial Electronics*, vol. 62, no. 2, pp. 1022–1033, Feb 2015.

[47] B. S. Umre, J. B. Helonde, J. P. Modak, and S. Renkey, "Application of gate-controlled series capacitors (GCSC) for reducing stresses due to sub-synchronous resonance in

turbine-generator shaft," in *2010 IEEE Energy Conversion Congress and Exposition*, Sept 2010, pp. 2300–2305.

[48] H. A. Mohammadpour, S. M. H. Mirhoseini, and A. Shoulaie, "Comparative study of proportional and TS fuzzy controlled GCSC for SSR mitigation," in *2009 International Conference on Power Engineering, Energy and Electrical Drives*, March 2009, pp. 564–569.

[49] H. A. Mohammadpour, M. M. Islam, E. Santi, and Y. J. Shin, "SSR damping in fixed-speed wind farms using series FACTS controllers," *IEEE Transactions on Power Delivery*, vol. 31, no. 1, pp. 76–86, Feb 2016.

[50] H. A. Mohammadpour and E. Santi, "Sub-synchronous resonance analysis in DFIG-based wind farms : Mitigation methods ; TCSC, GCSC, and DFIG controllers ; part ii," in *2014 IEEE Energy Conversion Congress and Exposition (ECCE)*, Sept 2014, pp. 1550–1557.

[51] R. K. Varma, S. Auddy, and Y. Semsedini, "Mitigation of subsynchronous resonance in a series-compensated wind farm using FACTS controllers," *IEEE Transactions on Power Delivery*, vol. 23, no. 3, pp. 1645–1654, July 2008.

[52] N. Rostamkolai, R. J. Piwko, E. V. Larsen, D. A. Fisher, M. A. Mobarak, and A. E. Poitras, "Subsynchronous interactions with static VAR compensators-concepts and practical implications," *IEEE Transactions on Power Systems*, vol. 5, no. 4, pp. 1324–1332, Nov 1990.

[53] Y. Y. Hsu and C. J. Wu, "Design of PID static VAR controllers for the damping of subsynchronous oscillations," *IEEE Transactions on Energy Conversion*, vol. 3, no. 2, pp. 210–216, Jun 1988.

[54] Z. Xin, Y. Ruoying, and G. Shan, "A novel objective function and analysis for optimal SVC parameters design to damping subsynchronous resonance," in *2016 China International Conference on Electricity Distribution (CICED)*, Aug 2016, pp. 1–6.

[55] K. R. Padiyar and N. Prabhu, "Design and performance evaluation of subsynchronous damping controller with STATCOM," *IEEE Transactions on Power Delivery*, vol. 21, no. 3, pp. 1398–1405, July 2006.

[56] M. S. El-Moursi, B. Bak-Jensen, and M. H. Abdel-Rahman, "Novel STATCOM controller for mitigating SSR and damping power system oscillations in a series compensated wind park," *IEEE Transactions on Power Electronics*, vol. 25, no. 2, pp. 429–441, Feb 2010.

[57] A. Moharana, R. K. Varma, and R. Seethapathy, "SSR alleviation by STATCOM in induction-generator-based wind farm connected to series compensated line," *IEEE Transactions on Sustainable Energy*, vol. 5, no. 3, pp. 947–957, July 2014.

[58] L. A. S. Pilotto, A. Bianco, W. F. Long, and A. A. Edris, "Impact of TCSC control methodologies on subsynchronous oscillations," *IEEE Transactions on Power Delivery*, vol. 18, no. 1, pp. 243–252, Jan 2003.

[59] S. R. Joshi, E. P. Cheriyan, and A. M. Kulkarni, "Output feedback SSR damping controller design based on modular discrete-time dynamic model of TCSC," *IET Generation, Transmission Distribution*, vol. 3, no. 6, pp. 561–573, June 2009.

[60] N. Kakimoto and A. Phongphanphanee, "Subsynchronous resonance damping control of thyristor-controlled series capacitor," *IEEE Transactions on Power Delivery*, vol. 18, no. 3, pp. 1051–1059, July 2003.

[61] M. Bongiorno, L. Angquist, and J. Svensson, "A novel control strategy for subsynchronous resonance mitigation using SSSC," *IEEE Transactions on Power Delivery*, vol. 23, no. 2, pp. 1033–1041, April 2008.

[62] K. Rachananjali, N. Pavani, S. Suman, and D. V. S. B. Chaitanya, "Damping of subsynchronous resonance using SSSC with hysteresis current control," in *2014 International Conference on Green Computing Communication and Electrical Engineering (ICGCCEE)*, March 2014, pp. 1–5.

[63] T. Rajaram, J. M. Reddy, and Y. Xu, "Kalman filter based detection and mitigation of subsynchronous resonance with SSSC," *IEEE Transactions on Power Systems*, vol. 32, no. 2, pp. 1400–1409, March 2017.

[64] F. A. R. A. Jowder and B.-T. Ooi, "Series compensation of radial power system by a combination of SSSC and dielectric capacitors," *IEEE Transactions on Power Delivery*, vol. 20, no. 1, pp. 458–465, Jan 2005.

[65] D. Rai, S. O. Faried, G. Ramakrishna, and A. A. Edris, "An SSSC-based hybrid series compensation scheme capable of damping subsynchronous resonance," *IEEE Transactions on Power Delivery*, vol. 27, no. 2, pp. 531–540, April 2012.

[66] N. G. Hingorani, B. Bhargava, G. F. Garrigue, and G. D. Rodriguez, "Prototype ngh subsynchronous resonance damping scheme. part i, field installation and operating experience," *IEEE Power Engineering Review*, vol. PER-7, no. 11, pp. 47–48, Nov 1987.

[67] Z. Xueqiang and C. Chen, "Damping subsynchronous resonance using an improved NGH SSR damping scheme," in *1999 IEEE Power Engineering Society Summer Meeting. Conference Proceedings (Cat. No.99CH36364)*, vol. 2, 1999, pp. 780–785 vol.2.

[68] R. A. Hedin, K. B. Stump, and N. G. Hingornai, "A new scheme for subsynchronous resonance damping of torsional oscillations and transient torque - part ii, performance," *IEEE Transactions on Power Apparatus and Systems*, vol. PAS-100, no. 4, pp. 1856–1863, April 1981.

[69] S. Ren, S. Wang, Y. Zhu, Q. Wang, and X. Huang, "A blocking filter design method of effective suppression of three forms of SSR," in *2016 IEEE PES Asia-Pacific Power and Energy Engineering Conference (APPEEC)*, Oct 2016, pp. 599–603.

[70] X. Xie, P. Liu, K. Bai, and Y. Han, "Applying improved blocking filters to the SSR problem of the tuoketuo power system," *IEEE Transactions on Power Systems*, vol. 28, no. 1, pp. 227–235, Feb 2013.

[71] H. Cen and X. Wang, "Analysis of self-excitation in turbine-generators induced by static blocking filter," in *2010 Asia-Pacific Power and Energy Engineering Conference*, March 2010, pp. 1–5.

[72] D. Xiaoliang, X. Xiaorong, Y. Yu, and H. Yingduo, "Impacting factors and stable area analysis of subsynchronous resonance in DFIG based wind farms connected to series-compensated power system," *Power System Technology*, vol. 39, no. 1, p. 189, 2015. [Online]. Available : http://www.dwjs.com.cn/EN/abstract/article_25813.shtml

[73] M. T. Ali, M. Ghandhari, and L. Harnefors, "Effect of control parameters on infliction of sub-synchronous control interaction in DFIGs," in *2016 IEEE International Conference on Power and Renewable Energy (ICPRE)*, Oct 2016, pp. 72–78.

[74] U. Karaagac, S. O. Faried, J. Mahseredjian, and A. A. . Edris, "Coordinated control of wind energy conversion systems for mitigating subsynchronous interaction in DFIG-based wind farms," *IEEE Transactions on Smart Grid*, vol. 5, no. 5, pp. 2440–2449, Sept 2014.

[75] H. A. Mohammadpour and E. Santi, "SSR damping controller design and optimal placement in rotor-side and grid-side converters of series-compensated DFIG-based wind farm," *IEEE Transactions on Sustainable Energy*, vol. 6, no. 2, pp. 388–399, April 2015.

[76] M. A. Chowdhury, M. A. Mahmud, W. Shen, and H. R. Pota, "Nonlinear controller design for series-compensated dfig-based wind farms to mitigate subsynchronous control interaction," *IEEE Transactions on Energy Conversion*, vol. PP, no. 99, pp. 1–1, 2017.

[77] M. Ghafouri, U. Karaagac, H. Karimi, S. Jensen, J. Mahseredjian, and S. O. Faried, "An LQR controller for damping of subsynchronous interaction in DFIG-based wind farms," *IEEE Transactions on Power Systems*, vol. 32, no. 6, pp. 4934–4942, Nov 2017.

[78] P. H. Huang, M. S. E. Moursi, W. Xiao, and J. L. Kirtley, "Subsynchronous resonance mitigation for series-compensated DFIG-based wind farm by using two-degree-of-freedom control strategy," *IEEE Transactions on Power Systems*, vol. 30, no. 3, pp. 1442–1454, May 2015.

[79] L. Fan and Z. Miao, "Mitigating SSR using DFIG-based wind generation," *Sustainable Energy, IEEE Transactions on*, vol. 3, no. 3, pp. 349–358, July 2012.

[80] C. Zhu, L. Fan, and M. Hu, "Control and analysis of DFIG-based wind turbines in a series compensated network for SSR damping," in *IEEE PES General Meeting*, July 2010, pp. 1–6.

[81] L. Fan and Z. Miao, "Nyquist-stability-criterion-based ssr explanation for type-3 wind generators," *IEEE Transactions on Energy Conversion*, vol. 27, no. 3, pp. 807–809, Sept 2012.

[82] J. Mahseredjian, S. Dennetière, L. Dubé, B. Khodabakhchian, and L. Gérin-Lajoie, "On a new approach for the simulation of transients in power systems," *Electric Power Systems Research*, vol. 77, no. 11, pp. 1514 – 1520, 2007, selected Topics in Power System Transients - Part {II6th} International Conference on Power System Transients. [Online]. Available : http://www.sciencedirect.com/science/article/pii/S0378779606002094

[83] *Grid code - high and extra high voltage.* E.ON Netz GmbH, Bayreuth, Germany, April 2006.

[84] U. Karaagac, H. Saad, J. Peralta, and J. Mahseredjian, "Doubly-fed-induction-generator based wind park models in EMTP-RV."

[85] E. Muljadi, C. P. Butterfield, A. Ellis, J. Mechenbier, J. Hochheimer, R. Young, N. Miller, R. Delmerico, R. Zavadil, and J. C. Smith, "Equivalencing the collector system of a large wind power plant," in *2006 IEEE Power Engineering Society General Meeting*, 2006, pp. 9 pp.–.

[86] R. Varma, Y. Semsedini, and S. Auddy, "Mitigation of subsynchronous oscillations in a series compensated wind farm with thyristor controlled series capacitor (TCSC)," in *Power Systems Conference : Advanced Metering, Protection, Control, Communication, and Distributed Resources, 2007. PSC 2007*, March 2007, pp. 331–337.

[87] S. Auddv, "Modeling and resonance issues of wind farm integration with related FACTS applications," in *University of Western Ontario London, Ontario, Canada, Phd thesis*, 2007.

[88] D. Suriyaarachchi, U. Annakkage, C. Karawita, and D. Jacobson, "A procedure to study sub-synchronous interactions in wind integrated power systems," *Power Systems, IEEE Transactions on*, vol. 28, no. 1, pp. 377–384, Feb 2013.

[89] Z. Miao, "Impedance-model-based SSR analysis for type 3 wind generator and series-compensated network," *Energy Conversion, IEEE Transactions on*, vol. 27, no. 4, pp. 984–991, Dec 2012.

[90] R. Nath and C. Grande-Moran, "Study of sub-synchronous control interaction due to the interconnection of wind farms to a series compensated transmission system," in *Transmission and Distribution Conference and Exposition (T D), 2012 IEEE PES*, May 2012, pp. 1–6.

[91] M. Sahni, B. Badrzadeh, D. Muthumuni, Y. Cheng, H. Yin, S. Huang, and Y. Zhou, "Sub-synchronous interaction in wind power plants- part ii : An ERCOT case study," in *Power and Energy Society General Meeting, 2012 IEEE*, July 2012, pp. 1–9.

[92] H. Wang and W. Du, *"Analysis and Damping Control of Power System Low-frequency Oscillations"*, Power Electronics and Power Systems, Springer US, 1994.

[93] S. Skogestad and I. Postlethwaite, *"Multivariable Feedback Control : Analysis and Design"*, Wiley, 2005.

[94] S. Nallusamy, D. Velayutham, and U. Govindarajan, "Design and implementation of a linear quadratic regulator controlled active power conditioner for effective source utilisation and voltage regulation in low-power wind energy conversion systems," *IET Power Electronics*, vol. 8, no. 11, pp. 2145–2155, 2015.

[95] H. S. Ko and J. Jatskevich, "Power quality control of wind-hybrid power generation system using fuzzy-LQR controller," *IEEE Transactions on Energy Conversion*, vol. 22, no. 2, pp. 516–527, June 2007.

[96] G. Duan and H. Yu, *"LMIs in Control Systems : Analysis, Design and Applications"*, CRC Press, 2013.

[97] B. Chaudhuri, B. C. Pal, A. C. Zolotas, I. M. Jaimoukha, and T. C. Green, "Mixed-sensitivity approach to H^∞ control of power system oscillations employing multiple FACTS devices," *IEEE Transactions on Power Systems*, vol. 18, no. 3, pp. 1149–1156, Aug 2003.

[98] R. Majumder, B. C. Pal, C. Dufour, and P. Korba, "Design and real-time implementation of robust FACTS controller for damping inter-area oscillation," *IEEE Transactions on Power Systems*, vol. 21, no. 2, pp. 809–816, May 2006.

[99] S. Kong and R. Majumder, "H^∞ robust control design for wind driven doubly-fed induction generator," in *2008 IEEE Power and Energy Society General Meeting - Conversion and Delivery of Electrical Energy in the 21st Century*, July 2008, pp. 1–6.

[100] B. Chaudhuri and B. C. Pal, "Robust damping of multiple swing modes employing global stabilizing signals with a TCSC," *IEEE Transactions on Power Systems*, vol. 19, no. 1, pp. 499–506, Feb 2004.

[101] M. Chilali, P. Gahinet, and P. Apkarian, "Robust pole placement in lmi regions," *IEEE Transactions on Automatic Control*, vol. 44, no. 12, pp. 2257–2270, Dec 1999.

[102] B. Pal and B. Chaudhuri, *"Robust Control in Power Systems"*, Power Electronics and Power Systems, Springer US, 2006.

[103] D. Gu, P. Petkov, and M. Konstantinov, *"Robust Control Design with MATLAB®"*, Advanced Textbooks in Control and Signal Processing, Springer London, 2006.

[104] K. Zhou and J. Doyle, *"Essentials of Robust Control"*, Prentice Hall Modular Series f, 1998.

[105] J. Quanyuan, Z. Zhenyu, and C. Yijia, "Wide-area TCSC controller design in consideration of feedback signals' time delays," in *IEEE Power Engineering Society General Meeting, 2005*, June 2005, pp. 1676–1680 Vol. 2.

[106] M. S. Saad, M. A. Hassouneh, E. H. Abed, and A. A. Edris, "Delaying instability and voltage collapse in power systems using SVCs with washout filter-aided feedback," in *Proceedings of the 2005, American Control Conference, 2005.*, June 2005, pp. 4357–4362 vol. 6.

[107] S. Sönmez, S. Ayasun, and C. Nwankpa, "An exact method for computing delay margin for stability of load frequency control systems with constant communication delays," *IEEE Transactions on Power Systems*, vol. 31, no. 1, pp. 370–377, Jan 2016.

[108] N. Olgac and R. Sipahi, "An exact method for the stability analysis of time-delayed linear time-invariant (LTI) systems," *IEEE Transactions on Automatic Control*, vol. 47, no. 5, pp. 793–797, May 2002.

[109] H. Jia, N. Guangyu, S. T. Lee, and P. Zhang, "Study on the impact of time delay to power system small signal stability," in *MELECON 2006 - 2006 IEEE Mediterranean Electrotechnical Conference*, May 2006, pp. 1011–1014.

[110] H. Jia, X. Cao, X. Yu, and P. Zhang, "A simple approach to determine power system delay margin," in *2007 IEEE Power Engineering Society General Meeting*, June 2007, pp. 1–7.

[111] M. Hamzeh, M. Ghafouri, H. Karimi, K. Sheshyekani, and J. M. Guerrero, "Power oscillations damping in DC microgrids," *IEEE Transactions on Energy Conversion*, vol. 31, no. 3, pp. 970–980, Sept 2016.

[112] Q. Zhong, *"Robust Control of Time-delay Systems"*, Springer London, 2006.

[113] L. Dugard and E. Verriest, *"Stability and Control of Time-delay Systems"*, Lecture Notes in Control and Information Sciences, Springer Berlin Heidelberg, 1997.

[114] K. Watanabe and M. Ito, "A process-model control for linear systems with delay," *IEEE Transactions on Automatic Control*, vol. 26, no. 6, pp. 1261–1269, Dec 1981.

[115] C. Ahumada, R. Cárdenas, D. Sáez, and J. M. Guerrero, "Secondary control strategies for frequency restoration in islanded microgrids with consideration of communication delays," *IEEE Transactions on Smart Grid*, vol. 7, no. 3, pp. 1430–1441, May 2016.

[116] B. Chaudhuri, R. Majumder, and B. C. Pal, "Wide-area measurement-based stabilizing control of power system considering signal transmission delay," *IEEE Transactions on Power Systems*, vol. 19, no. 4, pp. 1971–1979, Nov 2004.

[117] R. Isermann, *"Fault-Diagnosis Systems : An Introduction from Fault Detection to Fault Tolerance"*, Springer Berlin Heidelberg, 2005.

[118] S. Ding, *"Model-Based Fault Diagnosis Techniques : Design Schemes, Algorithms and Tools"*, Advances in Industrial Control, Springer London, 2012.

[119] M. Aldeen and F. Crusca, "Observer-based fault detection and identification scheme for power systems," *IEE Proceedings - Generation, Transmission and Distribution*, vol. 153, no. 1, pp. 71–79, Jan 2006.

[120] X. J. Li and G. H. Yang, "Dynamic observer-based robust control and fault detection for linear systems," *IET Control Theory Applications*, vol. 6, no. 17, pp. 2657–2666, Nov 2012.

[121] J. Ribrant and L. Bertling, "Survey of failures in wind power systems with focus on swedish wind power plants during 1997-2005," in *2007 IEEE Power Engineering Society General Meeting*, June 2007, pp. 1–8.

[122] H. Liu, X. Xie, J. He, T. Xu, Z. Yu, C. Wang, and C. Zhang, "Subsynchronous interaction between direct-drive PMSG based wind farms and weak AC networks," *IEEE Transactions on Power Systems*, vol. 32, no. 6, pp. 4708–4720, Nov 2017.

[123] T. Bi, J. Li, P. Zhang, E. Mitchell-Colgan, and S. Xiao, "Study on response characteristics of grid-side converter controller of PMSG to sub-synchronous frequency component," *IET Renewable Power Generation*, vol. 11, no. 7, pp. 966–972, 2017.

[124] D. Sun, X. Xie, Y. Liu, K. Wang, and M. Ye, "Investigation of ssti between practical mmc-based vsc-hvdc and adjacent turbogenerators through modal signal injection test," *IEEE Transactions on Power Delivery*, vol. 32, no. 6, pp. 2432–2441, Dec 2017.

Appendix A System Equations

The equations used to describe the dynamics of the system are described in this appendix. In this set of equations, function f described in 3.9 is detailed. It should be noted that due to nonlinear terms in the equations, they should be linearized.

$$\dot{V}_{DC} = (\frac{0.353}{\mathrm{V_{DC}}})(-10^{-6}\,{\mathrm{V_{DC}}}^2 + \mathrm{i_{qr}}\,(0.096\,\mathrm{u_{qr}} - 0.096\,\mathrm{i_{qr}} + \mathrm{x_{dr}} - 0.158\,\sqrt{{\mathrm{V_{dsVF}}}^2 + {\mathrm{V_{qsVF}}}^2} + 0.886\,\mathrm{i_{dr}}\,(0.371\,\omega_\mathrm{m} - 0.371) + 0.216) + \mathrm{i_{qg}}\,(0.333\,\mathrm{V_{qf1}} + 0.666\,\mathrm{V_{qf2}} - 1.5\,\mathrm{i_{dg}} - 98.78\,\mathrm{i_{qf1}} - 98.78\,\mathrm{i_{qf2}} + 97.82\,\mathrm{i_{qg}} - 98.78\,\mathrm{i_{Lq}} - 98.78\,\mathrm{i_{qs}} + 0.976\,\mathrm{u_{qg}} + \mathrm{x_{qg}}) - 1.0\,\mathrm{i_{dr}}\,(0.096\,\mathrm{i_{dr}} - 0.096\,\mathrm{u_{dr}} - 0.096\,\mathrm{x_P} - 1.0\,\mathrm{x_{qr}} + 0.096\,\mathrm{V_{dsVF}}\,\mathrm{i_{LdIF}} + 0.096\,\mathrm{V_{qsVF}}\,\mathrm{i_{LqIF}} + 0.941\,(\omega_\mathrm{m} - 1.0)\,(3.249\,\mathrm{i_{qr}} + 3.08\,\mathrm{i_{qs}}) - 0.047) + \mathrm{i_{dg}}\,(0.33\,\mathrm{V_{df1}} - 0.494\,\mathrm{V_{dcmf}} + 0.66\,\mathrm{V_{df2}} - 98.7\,\mathrm{i_{df1}} - 98.7\,\mathrm{i_{df2}} + 97.8\,\mathrm{i_{dg}} - 98.7\,\mathrm{i_{Ld}} - 98.7\,\mathrm{i_{ds}} + 1.5\,\mathrm{i_{qg}} + 0.976\,\mathrm{u_{dg}} + 0.976\,\mathrm{x_{dc}} + \mathrm{x_{dg}} + 0.413)) \quad \text{(A.1)}$$

$$\dot{i}_{ds} = 378.9\,\mathrm{V_{df1}} + 757.8\,\mathrm{V_{df2}} - 112295\,\mathrm{i_{df1}} - 112295\,\mathrm{i_{df2}} + 112295\,\mathrm{i_{dg}} - 112296\,\mathrm{i_{Ld}} + 131.45\,\mathrm{i_{dr}} - 112333\,\mathrm{i_{ds}} - 103.4\,\mathrm{u_{dr}} - 103.4\,\mathrm{x_P} - 1077.3\,\mathrm{x_{qr}} + 103.4\,\mathrm{V_{dsVF}}\,\mathrm{i_{LdIF}} + 103.4\,\mathrm{V_{qsVF}}\,\mathrm{i_{LqIF}} + 1014.3\,(\omega_\mathrm{m} - 1.0)\,(3.249\,\mathrm{i_{qr}} + 3.08\,\mathrm{i_{qs}}) - 1.0\,\mathrm{i_{qs}}\,(3124.2\,\omega_\mathrm{m} + 376.9) - 1.0\,\mathrm{i_{qr}}\,(3296.6\,\omega_\mathrm{m} + 2.728 \cdot 10^{-14}) - 50.7 \quad \text{(A.2)}$$

$$\dot{i}_{qs} = 378.9\,\mathrm{V_{qf1}} + 757.8\,\mathrm{V_{qf2}} - 112295\,\mathrm{i_{qf1}} - 112295\,\mathrm{i_{qf2}} + 112295\,\mathrm{i_{qg}} - 112295\,\mathrm{i_{Lq}} + 131.4\,\mathrm{i_{qr}} - 112333\,\mathrm{i_{qs}} - 103.4\,\mathrm{u_{qr}} - 1077\,\mathrm{x_{dr}} + 171.2\,\sqrt{{\mathrm{V_{dsVF}}}^2 + {\mathrm{V_{qsVF}}}^2} + \mathrm{i_{ds}}\,(3124.2\,\omega_\mathrm{m} + 376.9) + \mathrm{i_{dr}}\,(3296.6\,\omega_\mathrm{m} + 2.728 \cdot 10^{-14}) - 955\,\mathrm{i_{dr}}\,(0.371\,\omega_\mathrm{m} - 0.371) - 232.9 \quad \text{(A.3)}$$

$$\dot{i}_{dr} = 106424\,\mathrm{i_{df1}} - 718.2\,\mathrm{V_{df2}} - 359.1\,\mathrm{V_{df1}} + 106424\,\mathrm{i_{df2}} - 106424\,\mathrm{i_{dg}} + 106424\,\mathrm{i_{Ld}} - 139.6\,\mathrm{i_{dr}} + 106459\,\mathrm{i_{ds}} + 109.8\,\mathrm{u_{dr}} + 109.8\,\mathrm{x_P} + 1144.1\,\mathrm{x_{qr}} + \mathrm{i_{qr}}\,(3501\,\omega_\mathrm{m} - 376.9) - 109.8\,\mathrm{V_{dsVF}}\,\mathrm{i_{LdIF}} - 109.8\,\mathrm{V_{qsVF}}\,\mathrm{i_{LqIF}} - 1077.3\,(\omega_\mathrm{m} - 1.0)\,(3.24\,\mathrm{i_{qr}} + 3.08\,\mathrm{i_{qs}}) + \mathrm{i_{qs}}\,(3318\,\omega_\mathrm{m} - 1.95 \cdot 10^{-13}) + 53.8 \quad \text{(A.4)}$$

$$\dot{i}_{qr} = 106424\,\mathrm{i_{qf1}} - 718.2\,\mathrm{V_{qf2}} - 359.1\,\mathrm{V_{qf1}} + 106424\,\mathrm{i_{qf2}} - 106424\,\mathrm{i_{qg}} + 106424\,\mathrm{i_{Lq}} - 139.6\,\mathrm{i_{qr}} + 106459\,\mathrm{i_{qs}} + 109.8\,\mathrm{u_{qr}} + 1144.1\,\mathrm{x_{dr}} - 1.0\,\mathrm{i_{dr}}\,(3501.2\,\omega_\mathrm{m} - 376.9) - 181.8\,\sqrt{{\mathrm{V_{dsVF}}}^2 + {\mathrm{V_{qsVF}}}^2} - 1.0\,\mathrm{i_{ds}}\,(3318\,\omega_\mathrm{m} - 1.955 \cdot 10^{-13}) + 1014.3\,\mathrm{i_{dr}}\,(0.371\,\omega_\mathrm{m} - 0.371) + 247.45 \quad \text{(A.5)}$$

$$\dot{\omega}_m = 1.687\,\omega_\mathrm{r} - 1.687\,\omega_\mathrm{m} - 0.125\,\mathrm{T_{sh}} - 0.035 \quad , \quad \dot{\omega}_r = 0.555\,\mathrm{T_{sh}} + 7.5\,\omega_\mathrm{m} - 7.5\,\omega_\mathrm{r} + 1.611\,\mathrm{i_{dr}}\,\mathrm{i_{qs}} - 1.611\,\mathrm{i_{ds}}\,\mathrm{i_{qr}} \quad , \quad \dot{T}_{sh} = 1357.1\,\omega_\mathrm{m} - 1357.1\,\omega_\mathrm{r} \quad \text{(A.6)}$$

$$\dot{i}_{qg} = 245.4\,\mathrm{u_{qg}} - 245.4\,\mathrm{i_{qg}} + 251.3\,\mathrm{x_{qg}} + 5.465 \cdot 10^{-9} \quad , \quad \dot{i}_{dg} = 245.4\,\mathrm{u_{dg}} - 245.4\,\mathrm{i_{dg}} - 124.2\,\mathrm{V_{dcmf}} + 245.4\,\mathrm{x_{dc}} + 251.3\,\mathrm{x_{dg}} + 103.9 \quad \text{(A.7)}$$

$$\dot{i}_{Ld} = 216.5\,\mathrm{V_{df1}} - 649.7\,\mathrm{V_{Cd}} - 649.7\,\mathrm{E_d} + 433.1\,\mathrm{V_{df2}} - 64186\,\mathrm{i_{df1}} - 64186\,\mathrm{i_{df2}} + 64186\,\mathrm{i_{dg}} - 64212\,\mathrm{i_{Ld}} - 64186\,\mathrm{i_{ds}} - 376.99\,\mathrm{i_{Lq}} \quad \text{(A.8)}$$

$$\dot{i}_{Lq} = 216.5\,\mathrm{V_{qf1}} - 649.7\,\mathrm{V_{Cq}} - 649.7\,\mathrm{E_q} + 433.1\,\mathrm{V_{qf2}} + 376.9\,\mathrm{i_{Ld}} - 64186\,\mathrm{i_{qf1}} - 64186\,\mathrm{i_{qf2}} + 64186\,\mathrm{i_{qg}} - 64212\,\mathrm{i_{Lq}} - 64186\,\mathrm{i_{qs}} \quad \text{(A.9)}$$

$$\dot{V}_{Cd} = 61.2\,\mathrm{i_{Ld}} - 376.9\,\mathrm{V_{Cq}} \quad , \quad \dot{V}_{Cq} = 376.9\,\mathrm{V_{Cd}} + 61.2\,\mathrm{i_{Lq}}$$

(A.10)

$$\dot{V}_{df1} = 18.8\,\mathrm{V_{df2}} - 18.8\,\mathrm{V_{df1}} - 376.9\,\mathrm{V_{qf1}} + 5586.1\,\mathrm{i_{df1}} - 2793\,\mathrm{i_{df2}} + 2793\,\mathrm{i_{dg}} - 2793\,\mathrm{i_{Ld}} - 2793\,\mathrm{i_{ds}}$$

(A.11)

$$\dot{V}_{qf1} = 376.9\,\mathrm{V_{df1}} - 18.8\,\mathrm{V_{qf1}} + 18.8\,\mathrm{V_{qf2}} + 5586\,\mathrm{i_{qf1}} - 2793\,\mathrm{i_{qf2}} + 2793\,\mathrm{i_{qg}} - 2793\,\mathrm{i_{Lq}} - 2793\,\mathrm{i_{qs}}$$

(A.12)

$$\dot{i}_{df1} = 63604\,\mathrm{V_{df2}} - 63604\,\mathrm{V_{df1}} - 9424778\,\mathrm{i_{df1}} - 9424778\,\mathrm{i_{df2}} + 9424778\,\mathrm{i_{dg}} - 9424778\,\mathrm{i_{Ld}} - 9424778\,\mathrm{i_{ds}} - 376.9\,\mathrm{i_{qf1}}$$

(A.13)

$$\dot{i}_{qf1} = 63604\,\mathrm{V_{qf2}} - 63604\,\mathrm{V_{qf1}} + 376.9\,\mathrm{i_{df1}} - 9424778\,\mathrm{i_{qf1}} - 9424778\,\mathrm{i_{qf2}} + 9424778\,\mathrm{i_{qg}} - 9424778\,\mathrm{i_{Lq}} - 9424778\,\mathrm{i_{qs}}$$

(A.14)

$$\dot{V}_{df2} = 18.8\,\mathrm{V_{df1}} - 18.8\,\mathrm{V_{df2}} - 376.9\,\mathrm{V_{qf2}} - 5586\,\mathrm{i_{df1}} + 2793\,\mathrm{i_{df2}} + 5586\,\mathrm{i_{dg}} - 5586\,\mathrm{i_{Ld}} - 5586\,\mathrm{i_{ds}}$$

(A.15)

$$\dot{V}_{qf2} = 376.9\,\mathrm{V_{df2}} + 18.8\,\mathrm{V_{qf1}} - 18.8\,\mathrm{V_{qf2}} - 5586.1\,\mathrm{i_{qf1}} + 2793\,\mathrm{i_{qf2}} + 5586\,\mathrm{i_{qg}} - 5586\,\mathrm{i_{Lq}} - 5586\,\mathrm{i_{qs}}$$

(A.16)

$$\dot{i}_{df2} = 127209\,\mathrm{V_{df1}} - 127209\,\mathrm{V_{df2}} - 37699112\,\mathrm{i_{df1}} - 37699112\,\mathrm{i_{df2}} + 37699112\,\mathrm{i_{dg}} - 37699112\,\mathrm{i_{Ld}} - 37699112\,\mathrm{i_{ds}} - 376.9\,\mathrm{i_{qf2}}$$

(A.17)

$$\dot{i}_{qf2} = 127209\,\mathrm{V_{qf1}} - 127209\,\mathrm{V_{qf2}} + 376.9\,\mathrm{i_{df2}} - 37699112\,\mathrm{i_{qf1}} - 37699112\,\mathrm{i_{qf2}} + 37699112\,\mathrm{i_{qg}} - 37699112\,\mathrm{i_{Lq}} - 37699112\,\mathrm{i_{qs}}$$

(A.18)

$$\dot{x}_{qg} = 4.366\,\mathrm{u_{qg}} - 4.366\,\mathrm{i_{qg}} + 9.721 \cdot 10^{-11} \quad , \quad \dot{x}_{dg} = 4.366\,\mathrm{u_{dg}} - 4.366\,\mathrm{i_{dg}} - 2.209\,\mathrm{V_{dcmf}} + 4.366\,\mathrm{x_{dc}} + 1.848 \quad , \quad \dot{x}_{dc} = 0.041 - 0.0410\,\mathrm{V_{dcmf}} \quad , \quad \dot{x}_{P} = 1.947 - 10.0\,\mathrm{V_{qsVF}}\,\mathrm{i_{LqIF}} - 10.0\,\mathrm{V_{dsVF}}\,\mathrm{i_{LdIF}}$$

(A.19)

$$\dot{x}_{qr} = 3.214\,\mathrm{u_{dr}} - 3.214\,\mathrm{i_{dr}} + 3.214\,\mathrm{x_P} - 3.214\,\mathrm{V_{dsVF}}\,\mathrm{i_{LdIF}} - 3.214\,\mathrm{V_{qsVF}}\,\mathrm{i_{LqIF}} + 1.576 \quad , \quad \dot{x}_{qr} = 3.214\,\mathrm{u_{qr}} - 3.214\,\mathrm{i_{qr}} - 5.319\,\sqrt{\mathrm{V_{dsVF}}^2 + \mathrm{V_{qsVF}}^2} + 7.239$$

(A.20)

$$\dot{V}_{dsVF} = 44.4\,\mathrm{V_{df1}} + 88.8\,\mathrm{V_{df2}} - 133.3\,\mathrm{V_{dsVF}} - 13171\,\mathrm{i_{df1}} - 13171\,\mathrm{i_{df2}} + 13171\,\mathrm{i_{dg}} - 13171\,\mathrm{i_{Ld}} - 13171\,\mathrm{i_{ds}}$$

(A.21)

$$\dot{V}_{qsVF} = 44.4\,\mathrm{V_{qf1}} + 88.8\,\mathrm{V_{qf2}} - 133.3\,\mathrm{V_{qsVF}} - 13171\,\mathrm{i_{qf1}} - 13171\,\mathrm{i_{qf2}} + 13171\,\mathrm{i_{qg}} - 13171\,\mathrm{i_{Lq}} - 13171\,\mathrm{i_{qs}} \tag{A.22}$$

$$\dot{i}_{LdIF} = 133.3\,\mathrm{i_{Ld}} - 133.3\,\mathrm{i_{LdIF}} \quad , \quad \dot{i}_{LqIF} = 133.3\,\mathrm{i_{Lq}} - 133.3\,\mathrm{i_{LqIF}} \quad , \quad \dot{V}_{dcmf} = 376.9\,\mathrm{x_{dcf}} \quad , \quad \dot{x}_{dcf} = 8327\,\mathrm{V_{DC}} - 8327\,\mathrm{V_{dcmf}} - 2505\,\mathrm{x_{dcf}} \tag{A.23}$$